Departamento de Física Atómica, Molecular y Nuclear

Dipartimento di Fisica e Astronomia "Galileo Galilei"

Instituto de Física Corpuscular

Doctorado por la Universidad de Valencia y de Padova

Nuclear Structure Studies on quadrupole and octupole correlations in the vicinity of heavy N=Z nuclei with AGATA and NEDA

TESIS DOCTORAL

María de la Luz Jurado Gómez

DIRIGIDA POR

Dr. Andrés Gadea

Dr. José Javier Valiente Dobón

Dr. Emmanuel Clément

TUTORES

Prof. Juan Zúñiga Román

Prof. Daniele Mengoni

January 2022

"Tomen la educación y la cultura, y el resto se dará por añadidura."

"Prendi l'istruzione e la cultura e il resto seguirà."

Antonio Gramsci

UNIVERSIDAD DE VALENCIA

Abstract

Departamento de Física Atómica, Molecular y Nuclear
Dipartimento di Fisica e Astronomia "Galileo Galilei"
Instituto de Física Corpuscular

Doctor of Philosophy

by María de la Luz Jurado Gómez

The evolution of collectivity is essential to understand the structure of nuclei far from stability. The region that lies just above the Z=50 closed shell, in the vicinity of N=Z, exhibits interesting collective properties of quadrupole and octupole character. The aim of this thesis is to study the evolution of the quadrupole and octupole collectivity in light Xe isotopes, when approaching the N=Z line, through the lifetime measurement of the low lying excited states of ^{112}Xe where the reduced transitions probabilities were determined. The collectivity in Xe isotopes when neutrons are removed increases until the mid-shell for neutrons around N=66 and decreases until N=58 where there is a change in the trend and the collectivity in the light Xe seems to persist. To investigate the evolution of collectivity, the quadrupole degree of freedom is studied through the lifetime of the 2^+ and 4^+ states in the ^{112}Xe nucleus measured for the first time.

The experiment was performed in the first campaign with the AGATA-NEDA+NW-DIAMANT setup installed at the GANIL laboratory, with the CSNSM "OUPS" plunger device. A fusion evaporation reaction was used to populate the ^{112}Xe [1] with a ^{58}Ni beam, with an energy of 250 MeV, impinging on a ^{58}Ni 1 mg/cm^2 target. A ^{197}Au degrader with a thickness of 5 mg/cm^2 was installed in the plunger device to degrade the energy of the reaction products without stopping them, in order to maximize the energy resolution. The experiment was performed with a trigger condition of one neutron identified in NEDA-NW in coincidence with two detectors in AGATA while the information of DIAMANT has been used off-line for identification of the channels.

The reduced transitions probabilities for the $4^+ \rightarrow 2^+$ and $2^+ \rightarrow 0^+$ transitions in ^{112}Xe have been determined and compared with different theoretical models: LSSM, BMF and TRS. In addition, the reduced transition probability for the $5^- \rightarrow 4^+$ transition is determined and an upper limit for the reduced transition probability for the $5^- \rightarrow 2^+$ transition could be determined.

Futhermore, the final part of the thesis is dedicated to my contribution of the construction of the NEDA detectors at INFN-LNL to be used in a campaign for measurements, including the experiment described in the thesis.

Acknowledgements

A València i la seua gent, als meus amics i en especial a les que s'han convertit en els meus millors amics i han fet de la terreta una llar per a mi. A Fátima, Arantxa, Xandre i Jesús, per tot el l'afecte i suport que m'heu donat. Os estimo molt!

A mis amistades de Córdoba, en especial a las niñas; Paola, Marta, Ángela y Rocío, por orden de aparición en mi vida. Gracias por estar ahí siempre y por todo el apoyo y cariño que me dais. Sois las mejores, amores.

Mención especial de agradecimiento al viejo! Por estar en todo momento y en concreto durante el doctorado, acompañándome en todo el proceso, en los buenos y los malos momentos, disfrutando de los primeros y apoyándome en los segundos. Eres mi colchoncito en la vida, siempre sé que caeré mullidita si tú estás a mi lado, mil gracias.

A mi gran y maravillosa familia. Sois la alegría hecha amor, dispersos pero siempre juntos en lo hondo; la de Barcelona, Formentera, Mallorca y Córdoba.

Por último y más importante, a mis padres. Corto se haría un agradecimiento aquí. Simplemente, nada de lo que soy y de lo que consiga sería posible sin vosotros. Valores férreos, alegría por la vida, resiliencia para continuar y un largo etcétera. Más allá de que me hayáis dado la vida y me guiéis con amor por ella, sois mis mejores amigos, os quiero mucho y no me imagino haber terminado esta tesis sin vuestra ayuda, ánimo, apoyo y amor constantes.

Contents

List of Figures

List of Tables

Abbreviations

ADC	Analog to Digital Converter
ADF	AGATA Data Format
ADL	AGATA Detector Library
AGATA	Advanced Gamma Tracking Array
ATC	AGATA Triple Cluster
BMF	Beyond-Mean-Field
CC	Charge Comparison
CSNSM	Centre de Sciences Nucléaires et de Sciences de la Matiére
CSS	Cyclotron à Secteurs Séparés
DAQ	Data AcQuisition
DCFD	Digital Constant Fraction Discriminator
DCM	Decay Curve Method
DDCM	Differential Decay Curve Method
DMA	Direct Memory Access
EDF	Energy Density Functinal
FADC	Flash Analog to Digital Converter
FEE	Front-End Electronics
FET	Field Effect Transistor
FOM	Figure-of-Merit
FPGA	Field Programmable Gate Array
FWHM	Full Width at Half Maximum
GANIL	Grand Accéléreteur National d'Ions Lourds
GCM	Generator-Coordinate Method
GLP	Global Level PProcessing

GTS	**G**lobal **T**rigger **S**Synchronisation
HFB	**H**artree-**F**ock-**B**ogoliubov
HWG	**H**ill-**W**heeler-**G**riffin
HPGe	**H**igh **P**urity **Ge**rmanium
IFIC	**I**nstituto **FI**sica **C**orpuscular
INFN	**I**stituto **N**azionale di **F**isica **N**ucleare
IPM	**I**ndependent **P**article **M**odel
IPM	**I**nstitut de **P**hysique **N**ucléaire
IRT	**I**ntegrated **R**ise **T**ime
ISOL	**I**sotope **S**eparation **O**n-**L**ine
LED	**L**eading **ED**ge
LISE	**L**igne d'**I**ons **S**uper **E**pluchés
LLP	**L**ocal **L**evel **P**Processing
LNL	**L**aboratori **N**azionali di **L**egnaro
LSSM	**L**arge-**S**cale **S**hell **M**odel
MWD	**M**oving **W**indow **D**econvolution
NARVAL	**N**ouvelle **A**cquisition temps-**R**éel **V**ersion 1.2 **A**vec **L**inux
ND	**N**eutron **D**amage
NEDA	**N**eutron **D**etector **A**rray
NGD	**N**eutron **G**amma **D**iscrimination
NIM	**N**uclear **I**nstrumentation **M**odule
NW	The **N**eutron-**W**all
OFT	**O**rsay **F**orward **T**racking
OUPS	**O**rsay **U**niversal **P**lunger **S**ystem
PID	**P**article **ID**entification
PM	**P**hoto**M**ultiplier
PSA	**P**ulse-**S**hape **A**nalysis
PUR	**P**ILE-**U**p **R**ejection
QRPA	**Q**uasiparticle **R**andom **P**hase **A**pproximation
RDDS	**R**ecoil **D**istance **D**oppler-**S**hift
SCCM	**S**ymmetry-**C**onserving **C**onfiguration **M**ixing

SCMF	**S**elf-**C**onsistent **M**ean-**F**ield
SE-DIFF	**S**ingle-**E**nded to **DIFF**erential
SM	**S**hell **M**model
SPIRAL	**S**ystéme de **P**roduction d**I**ons **R**adioactifs en **L**igneé
TDC	**T**ime to **D**igital **C**onverter
ToF	**T**ime **o**f **F**light
TES	**T**otal **E**nergy **S**surface
TRS	**T**otal **R**outhian **S**surface

A mis padres.

Chapter 1

Introduction

The study of the nuclear structure aims at understanding the fundamental building blocks of matter and how they combine, interact and evolve to form the universe. The nucleus is composed of strongly interacting neutrons and protons confined in a very small volume. The nucleons interact via the strong force (exchanging mesons) to form the nuclei, moreover, the Coulomb interaction between protons plays also a fundamental role in the structure of the nucleus. When increasing the mass, nuclei are bound until the unbalance between the two kinds of nucleons weakens the mean-field (seen by the individual nucleons) or due to the increasing repulsive Coulomb interaction of the protons. It is the complex interplay of motion between the nucleons in nuclei that leads to a wide variety of mesoscopic structures, from the independent-like particle behavior, in the mean-field created by the other nucleons, to the collective motion involving all of the nucleons such as in the rotations and vibrations. All nuclei involve an interplay between these extremes and the study of this interplay is the goal of nuclear structure studies.

The existence of nuclei with stable deformed shapes was experimentally realized early in the history of nuclear physics. The observation of large quadrupole moments led to the suggestion that some nuclei might have spheroidal shapes, which was confirmed by the observation of rotational band structures and since such a shape is symmetric under space inversion, all members of the rotational band will have the same parity.

The region that lies just above the Z=50 closed shell in the vicinity of ^{100}Sn exhibits original collective behaviors. Besides the development of deformation when adding

protons in the $g_{7/2}$ shell, shape coexisting structures, strong octupole correlations and original neutron-proton couplings arise.

This work aims at studying the structure of ^{112}Xe, one of the light isotopes of Xenon, that with Z=54, has four protons above the Z=50 shell closure.

1.1 Quadrupole collectivity in the light Xe isotopes

The main goal of the present work is the investigation of the quadrupole collectivity in ^{112}Xe. Indeed, as the neutron and proton drip-lines are approached, new phenomena are likely to appear and in particular unique microscopic configuration may be especially pronounced in the vicinity of the N=Z line due to the strong correlation between protons and neutrons occupying identical orbitals.

The region in the neighborhood of ^{100}Sn seems to be of particular significance on the investigation of the role of proton-neutron correlation in the structure of low-lying excitations. As an example, proton-neutron T=0 pairing has been proposed to explain the low-lying structure of the N=Z=46 ^{92}Pd [2].

Above ^{100}Sn, the N=Z nuclei are unbound, nevertheless, in the vicinity of N=50, the low-lying structure of the neutron deficient Xe isotopes might also be influenced by the proton-neutron pairing and by a possible core breaking of ^{100}Sn.

The systematic presented below illustrates the evolution of the 2^+ and 4^+ excitation energies in even-even Xe isotopes (see Fig. 1.1 and Fig.1.2). This energies are related to the collective properties of the nucleus. The corresponding state energies in Te and Sn are shown for comparison.

The evolution of the first 2^+ and 4^+ energy is represented as a function of the neutron number from the N=82 to N=50 shell closures. The semimagic nucleus ^{136}Xe presents the highest excitation energy for the yrast 2^+ state and the lowest reduced transition probability $B(E2; 2^+ \rightarrow 0^+)$ underlying the N=82 shell closure. As neutrons are removed, moving to the neutron-deficient side of the Segrè chart, the collectivity of the Xe isotopes increases until the mid-shell for neutrons ($g_{7/2}$, $d_{5/2}$, $d_{3/2}$, $s_{1/2}$, $h_{11/2}$) around N=66. Furthermore, the collectivity seems to decrease (excitation energies of the 2^+ increase) as expected until N=58 where there
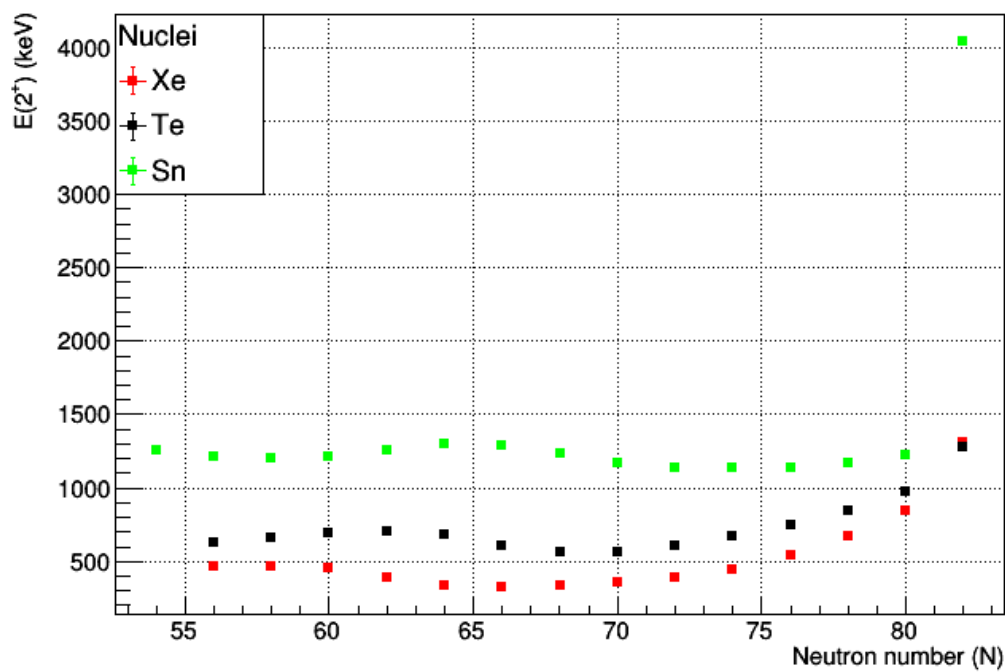
FIGURE 1.1: 2^+ state energies as a function of the neutron number of the Xe, Te and Sn isotopic chains nuclei.
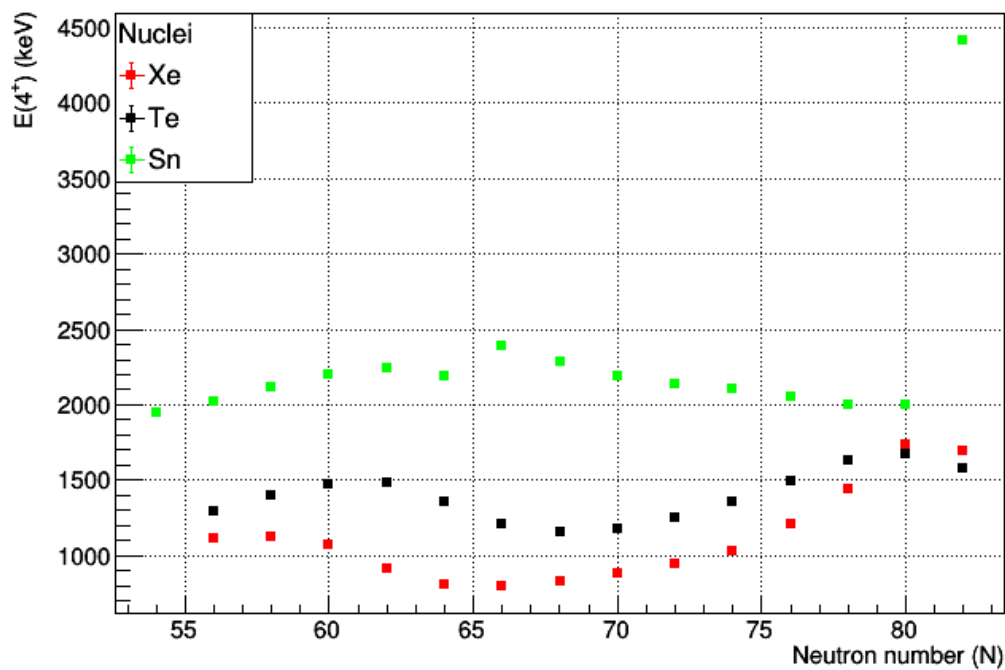
FIGURE 1.2: 4^+ state energies as a function of the neutron number of the Xe, Te and Sn isotopic chains nuclei.

is a sudden change in the trend and the collectivity in the light Xe persist [3]. In the lighter studied isotopes, this is supported by a tentative level scheme obtained in the in-beam spectroscopy of ^{110}Xe [4].

Nuclear models have tentatively explained the persistence of deformation and have examined to what extent enhanced proton-neutron pairing might be responsible for the behavior of the 2^+ and 4^+ excitation energy systematic. Based on the ^{110}Xe level scheme, it was proposed that pairing including deuteron-like J = 1 isoscalar pairs in QRPA calculations performed by D.S. Delion et al. are the essential ingredient to describe the collective behavior of light Xe [5].

B(E2) values were also predicted and the calculations show that the tendency of the $B(E2; 2^+ \rightarrow 0^+)$ close to N=50 is very sensitive to changes in pairing coupling parameters. However, the conclusions of these QRPA calculations have been ruled-out by large scale shell model calculations using a ^{100}Sn core [6].

The SM calculations show that the rotational-like behavior of the neutron-deficient Xe can be explained without strong np isoscalar pairing contribution and without reduction of the doubly magic ^{100}Sn shell gap. The shell model calculations carried for these collective nuclei are very demanding but, still, the agreement between the calculated excitation energies and the measured level scheme is remarkable. A detailed discussion of the model in relation with our experimental finding will be done in Chapter 6.

In this framework, we have performed the first measurement of the B(E2)s of the low-lying yrast states in ^{112}Xe via their lifetime using the plunger technique.

1.2   Octupole collectivity in the light Xe isotopes.

The spheroidal shapes in nuclei were discovered since large quadrupole moments were observed with rotational band structures. The spheroidal shapes are symmetric under space inversion thus all members in the rotational band have the same parity. Instead, nuclei that present a reflection-asymmetric shape, as for example pear shape, will develop as well low-lying negative-parity states. Extensive investigations of this kind of deformations have concluded that they rarely correspond to static deformations and, regarding excitations, that they are not as stable as the familiar quadrupole deformations. The reflection-asymmetric shapes are

generated by the octupole correlations due to the interaction between orbitals of opposite parity near the Fermi surface which differ by three units of angular momentum. In the vicinity of ^{100}Sn, the strongest octupole correlations are expected at the N=Z=56 ^{112}Ba [7]. In the light Xe nuclei, the Fermi surface lies between the $d_{5/2}$ and the $h_{11/2}$ orbitals for protons and neutrons. In the region around ^{114}Xe the octupole collectivity occurs for protons and neutrons at once. Experimentally, one of the strongest octupole correlations has been measured in ^{114}Xe [8] which the models can not recreate. The Generator-Coordinate Method (GCM) of the Hartree-Fock-Bogoliubov (HFB) self-consistent mean field theory with the Gogny force [9] was used for the calculations in ^{114}Xe with sucess in the 3^- state excitation energy. However, the calculation for the reduced transition probability gave a factor almost 4 times smaller that the experimental one, implying a possible failure in the model. Other calculations were made trying to get a better result, for instance using the quadrupole and octupole coupling with the same result as before [10] or changing the rotational formula [11].

At the present time there is no measurements of the octupole collectivity with the reduced transition probabilities beyond ^{114}Xe. This study aims to conduct the investigation about the increase of the octupole correlation in the very neutron deficient Xe isotope through the 5^- state lifetime. Measurements of reduced transition probabilities for E3 transitions are in general complex because, while the lifetime of the initial state can be determined with any high intensity transition de-exciting the level, the B(E3) determination required the branching ratio of the E3 transition that, frequently is very weak in the experimental spectra.

1.3 Thesis outline.

This thesis studies the evolution of the quadrupole and octupole collectivity in light Xe isotopes when approaching the N=Z line through the lifetime measurement of the first excited states of ^{112}Xe.

In the present chapter we introduce the theoretical framework which is fundamental for the discussion of the thesis results. In Chapter 2 the experimental set-up using the AGATA tracking array for γ-rays, the NEDA-Neutron Wall array for neutrons and DIAMANT for light charged particles detection coupling with the OUPS plunger device is described. The reaction mechanism employed in the

experiment as well as the experimental conditions are explained in Chapter 3. The data analysis and the validation of the lifetimetime measurement using the Decay Curve Method and its differential form with the Recoil Distance Doppler Shift technique is detailed in Chapter 4. In Chapter 5 the results for the measured lifetimes of ^{112}Xe are exposed. Theoretical interpretation using shell model and mean-field techniques are used for the study of the light Xe isotopes and the comparison with the thesis results is presented in Chapter 6. Chapter 7 specifies the contribution of the construction of the NEDA detectors going though the complete construction process. A summary of this thesis work in Spanish and Italian is given in Chapters 8 and 9, respectively.

Chapter 2

Experimental Set-up

2.1 The GANIL laboratory

The GANIL (Grand Accélérateur d'Ions Lourds) facility, located in Caen, France, provides stable ion beams for nuclear physics, atomic physics, radiobiology and material irradiation research since 1982.

Moreover, GANIL provides at the SPIRAL 1 facility intense exotic beams produced by the Isotope Separation On-Line (ISOL) method or using LISE spectrometer [12] by fragmentation of high-energy heavy-ion beams.

The GANIL facility scheme is shown in Fig. 2.1. The GANIL and SPIRAL 1 facility has 5 cyclotrons [13] as it can be seen in the figure. Different experiments can be run at the same time in the various experimental areas. Looking at the figure, the ion sources are shown with their compact cyclotron units C01 and C02 for the beam production and pre-acceleration irradiating a beam line IRRSUD (less than 1 MeV).

In the production of the radioactive beam in SPIRAL, the two first cyclotrons are used and CSS2 beam is sent toward the SPIRAL1 target. The beam is sent to the experimental areas (D1 - D5 and G1 - G4) through the fishbone.
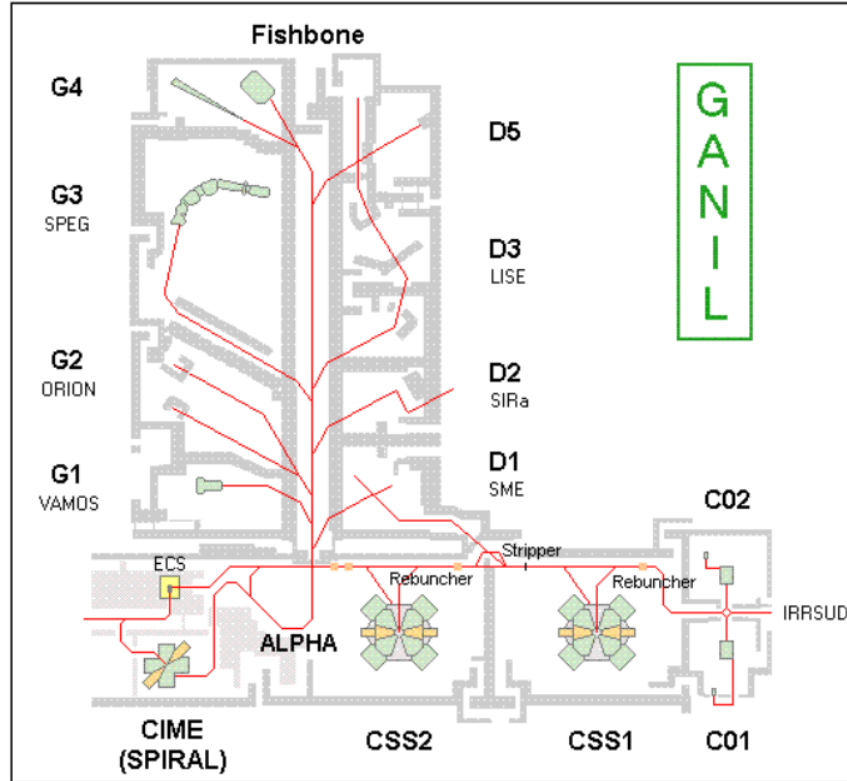
FIGURE 2.1: Scheme of the GANIL facility.

2.2   AGATA

2.2.1   The AGATA tracking array

The Advanced GAmma Tracking Array (AGATA) [14] project aims at building the
European forefront instrument based on semiconductor germanium detectors, for
high-resolution γ-ray spectroscopy. It is used in the nuclear research facilities op-
erating presently in Europe and will be especially important for the experimental
conditions expected at the future facilities for intense radioactive ion beams as
well as for high-intensity stable ion beams [15, 16]. The AGATA tracking array
is composed of segmented high-purity germanium detectors with front-end digital
electronics which relies on Pulse Shape Analysis (PSA) to extract the position of
the interaction points of the γ rays, which together with the digital determina-
tion of the Energy (with the Moving Window Deconvolution (MWD)) and Time
(with the Digital Constant Fraction Discriminator (DCFD)) are crucial for the
reconstruction of its path through the detector using the γ-ray tracking technique.

Since AGATA is presently under construction, only a limited number of detectors is available. The sub-array of AGATA used in the present experiment is shown in Fig. 2.2. The AGATA detectors are 36-fold electronically segmented coaxial germanium diodes operated in position sensitive mode. In this thesis work, the AGATA configuration was formed by 35 crystals. However, only 34 were operational. Futhermore, the AGATA array was positioned at nominal position.
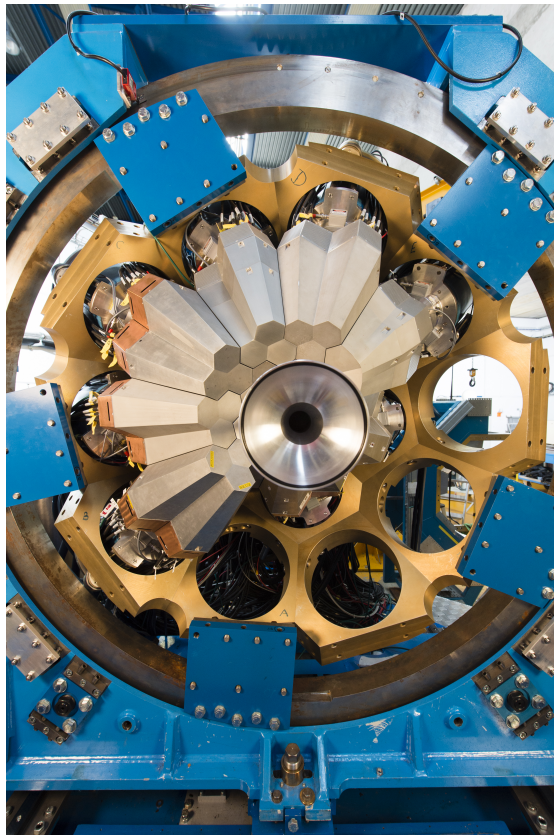
FIGURE 2.2: The Advanced GAmma Tracking Array (AGATA) at GANIL.

Thanks to the developments based on measurements and simulations plenty technical advances are being applied to make possible the construction and instrumentation of the AGATA encapsulated highly segmented germanium detectors into triple and double clusters detectors cryostats. AGATA combines digital electronics with fast sampling and data acquisition system processing at a high rate. AGATA has been designed to measure in a broad energy range, from ∼15 keV to few tens of MeV, with the two energy ranges provided for both core signal and segments. Additionally the position resolution of AGATA allows to perform an excellent Doppler correction reducing the Doppler broadening resolution losses. These performances are achieved by means of the γ-ray tracking technique [17].

AGATA is a travelling instrument between different host laboratories in Europe. The different campaigns aim at taking advantage of various beams and available facilities to maximize its scientific production [14].

2.2.2   AGATA detectors

The AGATA Triple Cluster (ATC) detector [14] consists of three asymmetric, encapsulated, α 36-fold electrically segmented, hexagonal shaped, coaxial n-type high purity germanium (HPGe) detectors. The weight of an AGATA crystal is about 2 kg and the n-type HPGe material has an impurity concentration specified to be between 0.4 and 1.8 x 10^{10} cm^3. The length of the coaxial Ge detectors is 9 cm and even if they are tapered, the relative efficiency of the detectors with the three different shapes is close to 80%. The asymmetric conformation in the geometry of such detector is necessary in order to optimize the tiling of the sphere with 180 detectors, achieving an 80% of the 4π angular coverage with germanium detector as shown in Fig. 2.3.
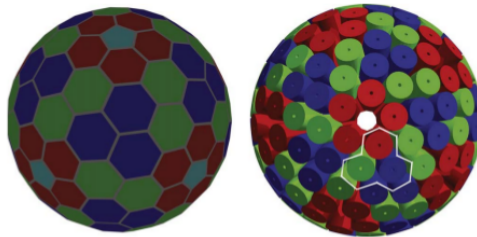
FIGURE 2.3: AGATA complete geometry design tiling of the sphere with 180 hexagones and 12 pentagones and the corresponding AGATA complete configuration. Figure taken from reference [14].

Presently the AGATA asymmetric encapsulated detectors are provided by MIRION Technologies (Canberra) while the company CTT produces the AGATA Triple Cluster (ATC) cryostats and installs the three detectors in the end-cap volume. The complete AGATA array will consist of 60 identical cryostats containing triplets of the three asymmetric detectors composing the tiling of the sphere. AGATA is designed to be also coupled to ancillary detectors, thanks to the inner radius of 23.5 cm.

The three types of detectors used in one AGATA cryostat slightly differ in their irregular hexagonal shape. Futhermore, each crystal with the A001, A002, etc. classification, has a length of 90 ± 1 mm and a diameter of $80^{+0.7}_{-0.1}$ mm at the back.

At the front, they are tapered to a hexagonal shape. The crystal has a 10 mm central hole which is broadening to a 13 mm in the front end. The 6-fold sector-wise segmentation goes through the middle of each flat hexagonal side. The 6-fold longitudinal segmentation forms rings of 8, 13, 15, 18, 18 and 18 mm in thickness starting at the hexagonal front face of the detector, in order to have an uniform distribution of γ-ray interactions and best pulse-shape sensitivity [14].

The AGATA identification assigns the letters A-F to the six sectors along the detector and the 1-6 numbers are used for the six rings, applying 1 to the front end and 6 at the back shown in Fig. 2.4. Due to the fragile surface of the crystals, an hermetical aluminium canister with a 0.8 mm wall thickness is used. The encapsulation technology was developed first for the EUROBALL cluster detectors by University of Köln. A space from 0.4 to 0.7 mm is used between capsule walls and crystal side faces. The capsules are mounted in the ATC detector with a 0.5 mm spacing between the flat surfaces. The 6 x 7 connector feed-throughs provide access to each of the 36 segmented outer contacts. Ceramic material is given to isolate the core contact, which applies the high voltage and it is used to get the core energy signals using an AC coupling in the charge preamplifier, acquiring 37 signals per crystal (38 electronic signals since core has high and low gains).

The signal channels are composed of a cold preamplifier stage working close to the liquid nitrogen temperature of the cryostat. The core preamplifier, designed to work at more than 50 kHz counting rate, has a low noise and large dynamic range for energy determination, pulse-shape analysis and timing properties.

A circuit board is mounted near the segment feed throughs and it is an interface for the cold part of the preamplifier electronics. It is relevant for the best performance of the crystals that cross-talk between segments signals, due to the capacitive coupling on cabling, feedthroughs and electronics, is minimal. Measurements provided cross-talk values of less than 1 in 10^{-3}, as it was described in an electronic model of crystals combination and preamplifier assembly [14].

2.2.3   Electronics, GTS and data flow

The only remaining analogic part in the full electronics chain is the preamplifiers of the segments and the cores, which are divided into two spatially separated parts, a cold and a warm part. The cold input stages are near the crystals to optimize
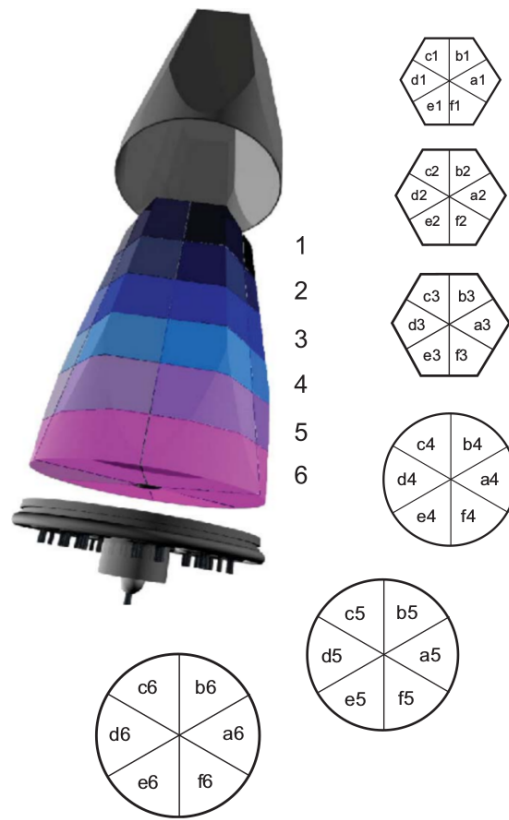
FIGURE 2.4: Segment labelling scheme of an AGATA crystal. Figure taken from reference [14].

noise performance and in order to minimise the cross-talk contributions a good electronic shielding is built between the input stages. The warm part, at room temperature, is separated by 15 cm cabling in the vacumm from the cold part of the cryostat and contains a low-noise transimpedance amplifier, a pole-zero stage, a differential output buffer and fast-reset circuit.

There are two cooling stages in the cryostats, one for the encapsulated Ge detector to 90 K and another for the cold part of the preamplifier electronics to near 130 $\pm$ 20 K. The rest of the preamplifier electronics is placed outside the vacuum. Both parts are electrically connected by hundreds of individual thin wires with low thermal conductivity. The vacuum used for the thermal isolation has pressure values below 10^{-6} mbar. Inside the cryostat, this pressure is kept during long periods using a Zeolith based getter. The individual FET consumes an electric power of $\sim$ 20 mW, reaching up to 2.3 W in the total consumption of the 111 FETs in a single triple cluster.

The Front-End Electronics of AGATA contain the preamplifiers mentioned above

which read the signals of the crystals. Subsequently, the signals from each AGATA crystal are digitized using sampling ADC boards. The pre-processing electronics receive the digital data which are timestamped and filtered via the Global Trigger and Synchronization system (GTS) [18]. Finally the information is sent to the Local Level Processing data flow.

In the AGATA electronics, when the core discriminator receives a signal, a local trigger sends a request towards the GTS. The GTS global trigger is in charge of the validation of the request by the trigger processor following a logic equation based in the coincidence and multiplicity conditions. In this work, a coincidence condition of 2 detectors of AGATA with signal and one neutron identified in the external trigger from NEDA is used with 30 ns time window between AGATA and NEDA. Following validation of an event, the data of each single capsule is sent to the corresponding processing computer.

The GTS contains sub-nanosecond clock synchronization and trigger data flow fabricated of a central trigger processor and nodes connected in a tree structure using optical fibers operated at 2 Gb/s. The measured detector signals from each γ-ray interaction are processed from the 36 segment signals and the core signal by the electronics of AGATA using analogue preamplifiers followed by sampling 100 MHz digitization corresponding to 10 ns time steps. An automatic phase-shift discrepancies correction and the measure of two different types of round-trip times is needed to obtain a sub-nanosecond synchronization [19].

Note that in general, large volume Ge detectors and associated electronics signals had an approximated bandwidth of 30 MHz, thus, our sampling frequency is well within the rules defined by the Nyquist sampling theorem.

The data flow is realized by the DCOD data acquisition of AGATA using the Actors defined in the object-oriented language Ada 95. DCOD uses three kind of Actors; producers, filters and consumers.

The AGATA data flow consists in two parts: The Local Level Processing (LLP) which treats each crystal individually and the Global Level Processing (GLP) which gathers all individual AGATA crystal and its ancillary together. The LLP consists of a producer, three filters (prepocessing, PSA and post-PSA) and a consumer. On-line only the LLP (producer, preprocessing, PSA and consumer) is performed. Off-line, the LLP (post-PSA) is first done followed by the event builder of the AGATA crystal, merged in a time stamp window of 20 ns and multiplicity

2. This forms the "AGATA event". In parallel, similarly, event builder is done for DIAMANT and NEDA. The three "events class" (AGATA, DIAMANT, NEDA) are then merged within a time window of 30ns. Finally, the tracking is performed in the Global level and data are sorted in a RootTree.

After the on-line processing, the data is stored in the AGATA disk server (based on the CEPH storage platform) and latter transfer to the GRID TIER1 locations at Lyon and Bologna. Most of the subsequent data analysis has been done in the GRID environment at IFIC.

2.2.4   Pulse shape analysis and tracking

The Pulse Shape Analysis (PSA) [14] is in charge of analyzing the shape of the charge and induced signals of the detector electrodes. The result of the PSA is the input for the tracking algorithms, which reconstruct the path of the γ rays inside the detector, and requires the energy (determined during the pre-processing with the MWD) and the three interactions determined in the PSA.

The signals in the segments of the detector are produced when electrons and holes are collected on the electrodes creating induced charges of opposite sign. In the coaxial detectors the drift time (charge collection time) is used to derive the radial position, wich depends on the distance to the electrode. The energy is measured with the charge calculated via the integral of the deposited charge from the sampled signals using the Moving Window Deconvolution technique [20].

In the detector, transient signals appear in the neighbourg segments of the segment that collected the net charge. The transient signals have null integral of the charge, contrary to the net charge signals. The rise-time of the net charge signals depends on the distance of the interaction points to the contact [21] as the shape of the induced signals depends on the distance of the interaction to the segments neighboring the one receiving the net charge [22, 23]. Thanks to the net charge signals and the transient signals, the positions of the γ-ray interactions are able to be reconstucted [17] with a final FWHM of approximately 4 mm [24].

The AGATA Detector Library (ADL) [25] is a traces library used by the PSA analysis to compare the shape of the measured signals, both the charged and induced. For this purpose, the ADL has simulated pulses of each segment and core in the detector for every interaction position of the γ ray. The measured and

the simulated signals (ADL) are compared. The best fit χ^2 based provides the interaction position of the γ ray for each interaction [24].

For this thesis work, the PSA has been done on-line during the experiment using the Adaptive Grid Search [26] that is the standard algorithm used presently by the AGATA collaboration.

In the Adaptive Grid Search algorithm, the detector is divided into a grid where to every point in the grid corresponds a simulated signal to compare with the measured ones. The position is the result of a three dimensional search in a coarse grid with a length of 6 mm per grid point and thereafter a more refined grid of 2 mm. Minimizing the Figure of Merit (FoM) shown in equation 2.1 it is possible to identify the most likely position of the interaction [27].

$$FoM = \sum_{j,t_i} |A_{j,m}(t_i) - A_{j,s}(t_i)|^p, \qquad (2.1)$$

where $A_{j,m}(t_i)$ and $A_{j,s}(t_i)$ are the pulses, in a segment j at the time (t_i), with the identification of m for the measured and s for the simulated signals. Only is taken into consideration the segment hitted, the nearest neighbours and the core signal. p is a chosen positive number higher than zero.

Corrections are made in the PSA to improve its performance such as crosstalk. The neutron damage correction will be applied in the Post-PSA processing, since it requires the position information provided by the PSA [28]. This effect occurs due to the fast neutrons hitting the gemanium detector producing lattice defects which acts as efficient hole traps. As it will be shown in the post-PSA Analysis in the section 4.2 it is visible on the left of the peak at lower energy a tail due to the charge collection deficit which can be reconstructed back inside the peak energy thanks to the radial dependency of charge trapping produced by the neutron-damage.

The deterioration of the detector signals can be produced by the crosstalk [29] between the segments of the electrically segmented crystals. The crosstalk effect is observable when there are differences between the sum of measured energies in the segments respect to the core energy as function of segment multiplicity. The core signal induces the principal crosstalk contribution and causes about 0.1% of crosstalk per fold in the sum of the segments energy, which can be corrected via a linear model that combines the signal amplitudes of the other segments.

With the information provided by the PSA, MWD and DCFD, i.e., position and time of the interaction, it is possible to apply the Tracking algorithm to reconstruct the path of the γ rays within the full AGATA array. The interactions of γ rays with matter, shown in Fig. 4.4 are considered in the tracking methods, such as the photoelectric effect, the Compton scattering and the pair production [30].
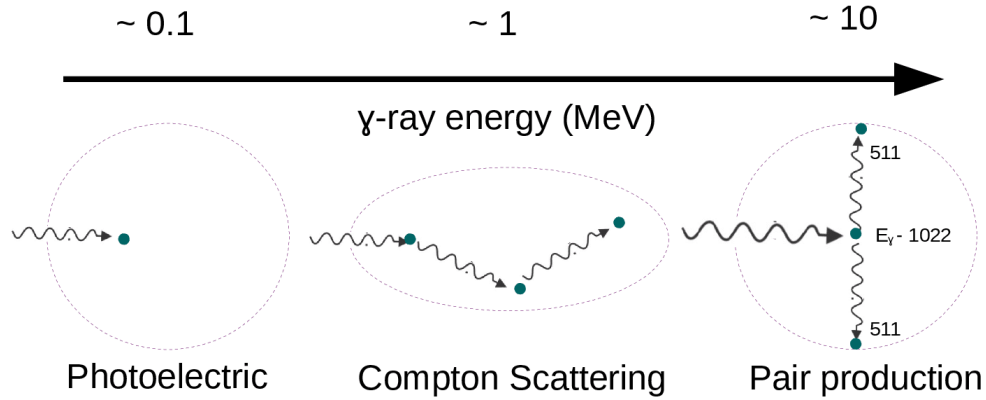
FIGURE 2.5: The main interaction mechanisms of γ rays in the tracking algorithms.

For low energy γ rays, an isolated point of interaction is recognized as a photoelectric absorption event with the total photon energy in the interation point. For γ rays of intermediate energy, from a few hundred keV to some MeV, the Compton scattering becomes the predominant interaction. This mechanism presents a succession of Compton scattering interactions and a final photoelectric effect where the energy of the last Compton scatered secondary γ-ray is realeased. Those events are reconstructed using a FoM represented in the equation 2.2, that evaluates the agreement of the possible interaction points with the values obtained from the Compton scattering formula [31]. For energies of few MeV, the pair production events become significant. The total energy of the γ ray is collected at the first point in this mechanism minus the mass needed to generate the electron-positron pair and eventually more interaction points are generated due to the annihilation photons.

In nuclear structure spectroscopy of the present work, most of the γ-ray energies are between 100 keV to 2 MeV. Therefore, most of the event are of Comptom scattering class.

In this thesis work, the Orsay Forward Tracking (OFT) is used [31]. It is a forward tracking algorithm based on identify interations points of the γ-rays starting in

the first hit. The OFT method starts grouping the interaction points according to their relative angular distance. At the beginning of the algorithm the angular coordinates θ and ϕ of all the interaction points and the distance between points are calculated defining clusters of interaction that might correspond to a single γ-ray [31]. If the cluster has more than 2 interaction points, all the possible interactions points are compared in the FoM mentioned above with the following equation:

$$F_E \propto exp(\frac{E_{s,C} - E_s}{\sigma_E^2}), \qquad (2.2)$$

where E_s s is the scattered energy measured from the interaction point energy, $E_{s,C}$ is the scattered energy obtained from the Compton scattering formula and σ_E^2 is the uncertainty in the determination of the scattered energies due to the position uncertainties of the interaction points.

The procedure is repetead until there are no more interactions in the cluster and for all the possible permutations of the interaction points within the cluster. The sequence which maximises the total FoM is shown in the following equation 2.3, it will be the correct sequence for the cluster, repeating it until there are no more interactions in the cluster and for all possible permutations of the interaction points.

$$F_{tot} = (F_{s \to i \to ... \to k})^{\frac{1}{2k-1}} \qquad (2.3)$$

For the single interaction clusters a FoM F_{sing} is assigned due to the complete energy absorbed in the photoelectric interaction and they are calculated at the end of the tracking process. The next step in the algorithm is to sort clusters in relation to the decreasing FoM. The algorithm will reject the cluster with statistics smaller than F_{track}, and with at least one matching interaction point. F_{sing} is set to be equal to the cluster acceptance level in order to reject as few single interactions clusters as possible. F_{sing} is set to be equal to the cluster acceptance level in order to minimise the flagging of single interaction clusters.

The forward-tracking algorithm was used in this thesis work, because is more efficient and provides a better Peak-to-Total ratio (P/T) that is a signal-to-noise

figure for γ-ray spectroscopy, than the back-tracking algorithm. The forward-tracking algorithm gives better results for all incident photon energies and for all variety of event multiplicities (except the case of high-multiplicity rotational cascades) [31].

2.3   NEDA

2.3.1   The NEDA detector array

NEDA, The NEutron Detector Array [32], presented in Fig. 2.6, is a new generation neutron detector with high-detection efficiency, excellent neutron-γ discrimination, high two neutrons discrimination capabilities and high counting rate capabilities, that has been designed to be coupled to a set of germanium-based gamma detectors like AGATA, EXOGAM2 [33] or GALILEO [34].

Just like the AGATA spectrometer, NEDA was designed to travel to the different facilities in Europe in order to take advantage of the different stable and radioactive ion beams.

The project of design the construction of NEDA started in 2007 involving researched groups from institutes in 9 European countries. NEDA was employed for the first time in a campaign at GANIL with AGATA 1π detector that was devoted to the study of neutron-deficient nuclei using fusion-evaporaton reactions. This thesis work has its origin in this physics campaing.

The crucial parameter of the array is the efficiency to detect and identify one or multiple neutrons in experiments in which emission of neutrons is very scarce surrounded by a high γ-ray background.

In the current experiment, ^{112}Xe nucleus is populated in a fusion evaporation reaction ^{58}Ni(^{58}Ni 2n2p) ^{112}Xe with a extremely weak reaction channel evaporating two protons and two neutrons after the compound nucleus is created. In order to study the excited nuclei after the reaction, the selection of the reaction channel and thus the emitted neutrons from the compound nucleus is mandatory. 90% of the reaction involve only charged particles channel. Having at least one neutron trigger removes 90% of the unwanted reaction channel detection.
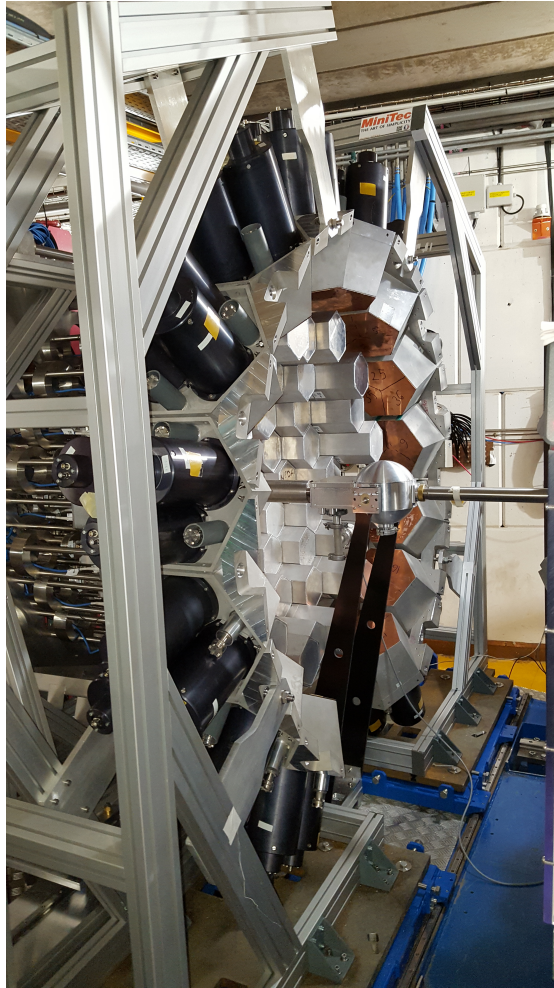
FIGURE 2.6: The NEutron Detector Array coupled to the Neutron Wall at 90°.

For a good identification of the evaporation residues a neutron detector array should have large efficiency, high gamma-ray to neutron discrimination capability and should minimize the multiple neutron scattering that misleads the neutron multiplicity determination. Neutron detectors arrays, like the Neutron Wall [35],[36] or Neutron Shell [37] have been previously constructed and successfully used in nuclear structure experimental research [38].

Comparing with these existing arrays, NEDA maximizes the neutron detection efficiency and minimizes the cross-talk or double hit of one neutron which misleads the number of neutrons emitted due to their scattering. The cross-talk between the detectors or double hit is the main challenge in neutron detectors that falsifies the real multiplicity of the emitted neutron. Futhermore, NEDA is a neutron detector based on a liquid scintillator that provides neutron-γ discrimination resulting from the pulse-shape analysis and ToF information with high discrimination

capabilities between neutrons and γ rays. NEDA uses digital electronics, digital signal proccessing and digital pulse shape discrimination which it will be explained in the following subsections.

The NEDA geometry has been reached from a large amount of studies using Monte Carlo simulations to improve each parameter and each section of NEDA. Using Geant4 simulations [38], a depth of 20 cm was decided for the detector. The size of the PM (photomultiplier) tube is 5 inches and the surface of the detector was optimized to fit the PM tube. An aluminium canning with a thickness of 3 mm is used in order to provide sufficient mechanical stability of the detector [39]. The detector unit is shown in Fig. 2.7 [32].
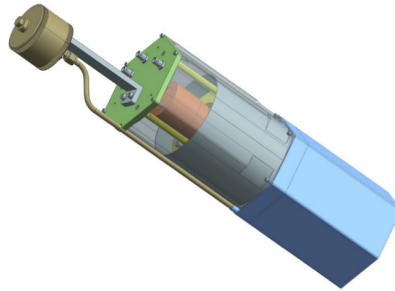
FIGURE 2.7: Drawing showing the design of a NEDA neutron detector. Figure taken from reference [32].

The future NEDA 2π design will consist of 331 single neutron detectors placed one metre from the target and covering a solid angle of 1.88 π s.r. The angular coverage for each individual detector is about 7.5° [32]. This configuration is designed to improve the neutron-γ discrimination, based on Time-Of-Flight (TOF) measurements, and the neutron angular resolution. The geometry for the NEDA 2π configuration at one metre focal distance is shown in Fig. 2.8 [32].

For the 54 NEDA detectors used in this experiment, NEDA detector array was constructed with the shape of a hexagonal prism, see Fig. 2.9 [39], filled with 3.15 l of the EJ-301 liquid scintillator.

The PM tube, described in the chapter 7, is fitted in a hexagonal structure with 146 mm side to side distance [40]. In order to optimize the timing [38] and Neutron-γ Discrimination (NGD) capabilities [39], Hammamatsu R11833-100HA was the PM tube selected [40].
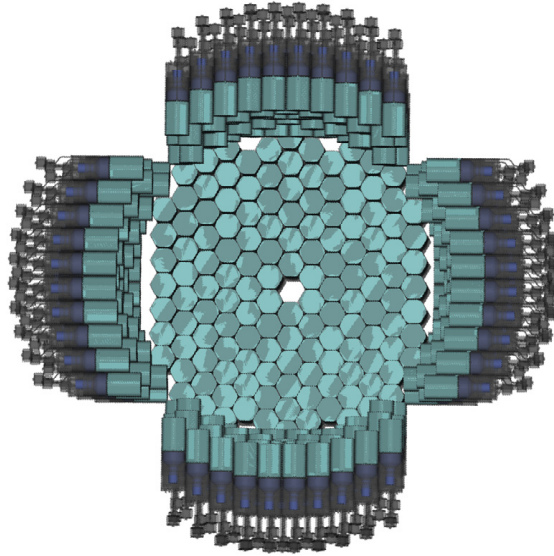
FIGURE 2.8: Proposed NEDA geometry for a 2π angular coverage at one metre distance from the focal point. Figure taken from reference [32].
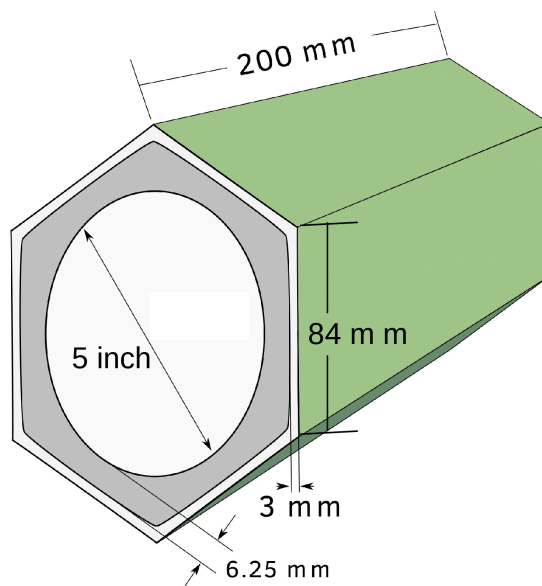
FIGURE 2.9: Schematic picture of the NEDA detector unit.

Regarding the timing, a higher statistics of photoelectrons define better the rising time which brings it to better results in the Constant Fraction Discrimination and Leading Edge algorithms. Another important aspect of requiring a high light yield for the NEDA detector is to achieve a good neutron-γ discrimination. The neutron-γ discrimination is in the tail of the signal when only 10% of the light is present and this is where the difference between neutrons and γ rays is manifested [40].

2.3.2   NEDA coupled to AGATA

NEDA is designed to be an ancillary detector for γ-rays arrays like AGATA. This set-up has large neutron detection efficiency and excellent neutron-γ discrimination at high counting rates.

The neutrons emitted during the fusion-evaporation reaction are measured with NEDA. These neutrons have a Maxwellian distribution with a maximum at energies of a few MeV and due to the kinematics of the reaction, they have an angular distribution peaked at forward angles with respect to the beam direction. NEDA has been specially optimised to have large efficiency in such fusion-evaporation reactions, for neutron multiplicities 2 and 3 [32].
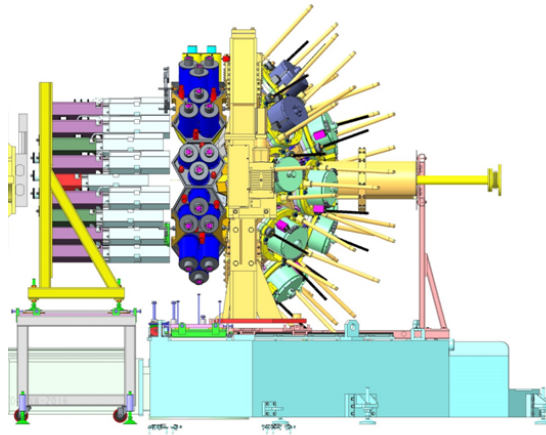
FIGURE 2.10: AGATA coupled to the NEDA and the NWALL detectors.

NEDA and some detector of its predecessor Neutron-Wall [35] were coupled in order to maximise the efficiency of the setup, being Neutron Wall detector located at 90°. The geometry of the configuration array with the complete set-up is shown in Fig. 2.10 [41].

2.3.3   Electronics and data flow

Neutron detection and neutron-γ discrimination are the main objetive for NEDA and its electronics, called NEDA Front-End Electronics (FEE). The electronics of NEDA uses a Global Trigger and Synchronisation (GTS) [19] system to make easier the coupling with other detectors, for example, set-ups including AGATA
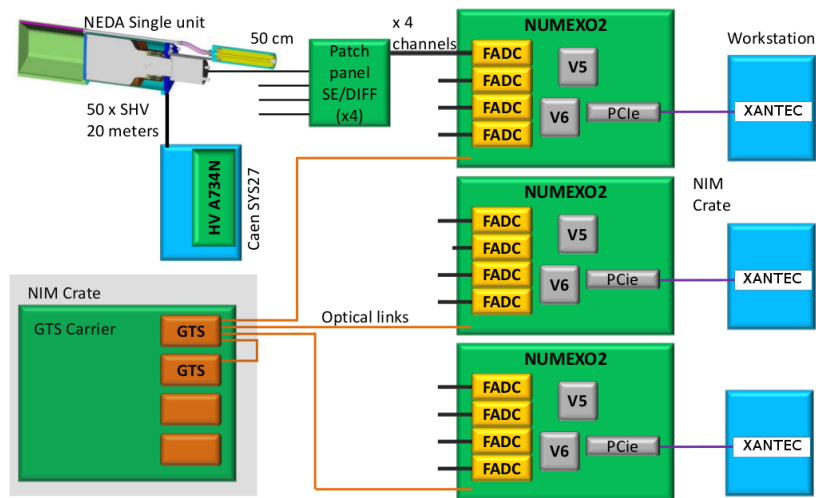
FIGURE 2.11: General scheme of NEDA electronics.

or EXOGAM2. In Fig. 2.11 [42] it is shown a general scheme of the electronics, used in this experiment for 54 channels.

As shown in the previously mentioned figure, the current signal provided by the detector PM tube is connected through a 15 m shielded coaxial BNC cable connected to a patch panel that includes the Single-Ended to Differential (SE-DIFF) conversion as required for the NUMEXO 2 digitizer. The subsequent transmission of the differential signal is done through a HDMI cable, selected taking into account the signal bandwith and the crosstalk between the 4 differential signals transmitted. The shielded coaxial cables have a -0.43 dB at 480 Mhz and the HDMI cables have a bandwidth of 430 MHz and crosstalk levels of -42.29/-48.11 dB for signals with rise-times of 3 and 7 ns, respectively. The SE-DIFF convertor has been developed in the NIM standard and each single board converts the signal of 16 detectors. The SE-DIFF channels use the low-noise fully differential amplifier AD8139 from Analog Devices and each channel is adapted to work in a range of 3 V. The high voltage of the PM tube is giving by the CAEN modules SY527 located at 20m from the detectors.

After that, the NUMEXO2 digitizers, developed for EXOGAM2 and NEDA, acquires and pre-process the data. Each NUMEXO2 digitizer includes a set of 4 Flash Analog-to-Digital-Converter (FADC) Mezzanines which digitize four signals at 200 Msps. NUMEXO2 motherboard has two large FPGAs to make the trigger generation, the process of the digital signal, clocking, data packaging and the

readout of the data to the servers in 16 independent channels.

The two aforementioned FPGAs are called Virtex-5 and Virtex-6. For the triggering of the channels located inside the digitizers, Virtex-5 includes the GTS leaf firmware. The Virtex-5 is also in charge of the readout via PCIe, slow control via Ethernet and the implementation of the ADC interface. The ADC interface is the firmware part that manage the storage of the data and the Validation, Rejection or Time-out by the GTS system. The Virtex-6 FPGA is in charge of the data processing, trigger elaboration and package building.

In the Virtex-6 a PSA algorithm processing is done to generate a trigger when a neutron is detected. The PSA processing is started on the identification of a signal by a leading edge (LED) or a (DCFD). This PSA realizes the neutron-γ discrimination with the charge-comparison method. Also a Time-of-Flight information is used calculating the time between the DCFD zero-crossover signal and an external reference signal that in our case was the cyclotron radio frequency. Following the GTS validation, the data are sent to a server (one server per NUMEXO-2) via an MPO optical fibre and a commercial PCIe interface board produced by Samtec.

As it was mentioned before, the signals were pre-processed by NUMEXO2 digitizers, specifically with 6 digitizers that allow to acquire the 96 neutron detectors, 54 NEDA detectors and 42 Neutron Wall detectors. In the Fig. 2.12 [32] it can be seen a schematic view of the data acquisition system represented for one NUMEXO2 card. The NARVAL system is in charge of realize the data flow for NEDA. It was developed by IPN Orsay using a ADA language for the data flow, and includes from the producer actor which reads the data until the merging of AGATA, DIAMANT and NEDA events done off-line. The filtering software of the actor was developed by the AGATA-NEDA collaboration with C++ for the data flow and they are integrated in shared libraries in the environment of NARVAL.

The NUMEXO2 digitizers are within a sub-network of the AGATA electronics for the NEDA and AGATA GTS alignment. In order to transmit the data from GANIL network to the AGATA network, the blue and the red dashed lines in Fig. 2.12 respectively, a bridge is used. The bridge is done via the MFM Transmitter and the MFM Catcher couple and the MFM2ADF changes the data format. The GANIL network is in charge of the local processing data and the raw events storage. The AGATA network is in charge of the rest of the process until the building and merging which are doing off-line. The process starts with the producer actor which
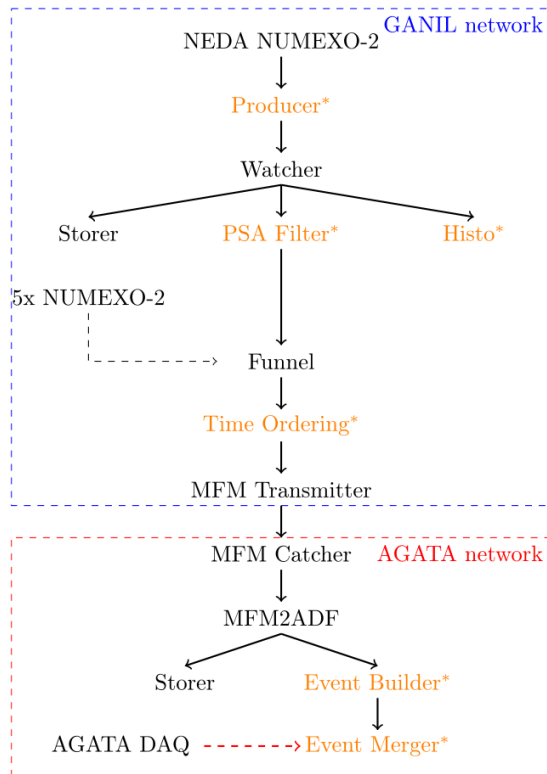
FIGURE 2.12: NEDA data acquisition system diagram. There are two network shared by the NEDA acquisition system, the GANIL and the AGATA network in blue and red dashed line respectively. The transmission of the data between the two networks is performed by one bridge. Figure taken from reference [32].

extracts the data from the Direct Memory Access (DMA) via the aforementioned PCIe interface and send it to the NARVAL environment. Then, the data is send to three actors, a storer, an histogrammer (Histo) and an online PSA Filter. The storer is in charge of store the full events of the digitised signals on disk, that then it can be processed with PSA algorithms. The PSA Filter is a code which executes two different algorithms, the Charge-Comparison (CC) similar to the one used in the FPGA and the integrated rise-time algorithm. A third algorithm will be implemented in the future, the Neural Network [23, 43]. The traces in the output of the PSA were removed to reduce the size of the data. And at last, the third actor is the histogrammer for the data quality monitoring.

Afterwards, the Funnel filter actor takes the output of the PSA Filter, i.e. the reduced frame, and the frame header, provided by the 6 acquisition servers via Ethernet producing a single output to be transmitted to a time ordering filter actor. After this time sorting, the data is send frame-by-frame to the MFM Transmitter. The MFM frames are written in the AGATA Data Format (ADF) using the

MFM2ADF filter actor. Off-line the data flow is split into a storer actor and the builder actor that generates the NEDA and NW events. To know the real neutron multiplicity the NEDA events are reconstructed using neutron scattering algorithms. Finally, the last actor present in the data acquisition system merges the NEDA and NW events with AGATA.

2.3.4   Triggering in AGATA

While the triggering decision is taken after the NGD processing, the triggering time is calculated using a digital constant fraction discriminator (DCFD) which also send the start signal to a Time-to-Digital-Converter (TDC) used to obtain the Time-of-Flight (ToF) of the neutrons.

Considering the average distance and energy of the neutron in the typical fusion-evaporation reaction, the neutron ToF varies between 20 and 80 ns. Thanks to the offline treatment of the signal, the timing resolution of the individual detectors, measured on the γ-ray peak can be reduced from 20 ns down to 3 ns [44].

Both for the NGD and the neutron scattering the ToF is essencial to reject unreal events. It is possible to find out if it is a single or multiple neutron event with the relation between the distance of two involved detectors and their ToF difference, as it will be shown in the section 4.3 of this work.

2.3.5   Pulse shape analysis

The application of Pulse Shape Analysis (PSA) to discriminate between neutrons and γ rays is one of the main developments for NEDA, being a digital system. The PSA is implemented in the NUMEXO2 firmware for triggering and in the on-line data acquisition system.

There exist different algorithms to achieve the NGD by means of Pulse Shape Analysis arised the Charge Comparison during the PSA filter of NEDA. Another algorithm that could have been used is the Integrated Rise-Time (IRT), however it was discarded due to the performance results in the discrimination of the neutrons.

The Charge Comparison algorithm realized the neutron-γ discrimination, comparing the ratio between different gates in the charge (proportional to the light

released in the detector) as is shown in the equation 2.4. The short gate integration I_S starts at the Constant Fraction DiscriminatoR position and is including a few samples (≤ 10 samples), and the long gate integration I_L integrates also the tail of the signal (≤ 70 samples) [44].

$$R_{cc} = \frac{I_L}{I_S + I_L} \tag{2.4}$$

The parameters of the CC algorithm were optimized for the campaign of this experiment using the FoM defined in Ref. [45], where it was obtained a FoM $\geqslant$ 1.7 for the NEDA detectors and 1.3 for the Neutron Wall detectors [44].

Also in this campaign besides the PSA Filter explained above, the pile-up rejection algorithm (PUR) was applied to reject the large amplitude signals, the pile-up events at high counting rates.

To do so, the PUR acts in different steps based on the CFD algorithm. The PUR makes a simple counting of the zero-crossing happening after the CFD. To avoid rejection a to important fraction of the events, only pile-up in the integration windows (short, long, and total energy) needs to be rejected. The PUR uses the CFD algorithm counting the zero-cross events after the CFD. A neural network PSA is under development to obtain for low energy signals the best NGD [23, 43]. However, this was not used in the present work. More than 95% of the raw signals are present at the end of the offline analysis process [44].

2.4 DIAMANT

2.4.1 The DIAMANT detector array

DIAMANT [46] is a 4π array of scintillation detectors for the detection of charged-particle, see Fig. 2.13. DIAMANT was developed to be an ancillary of large γ-ray spectrometers to identify the light charged particles emitted in heavy-ion induced reactions.

It has 60 CsI detectors, each one built of a piece of 3 mm thick CsI scintillation crystal coupled to pin-photodiode by 5 mm plexi-glass light guide, with improved light collection, which are equipped with preamplifiers working in vacuum.
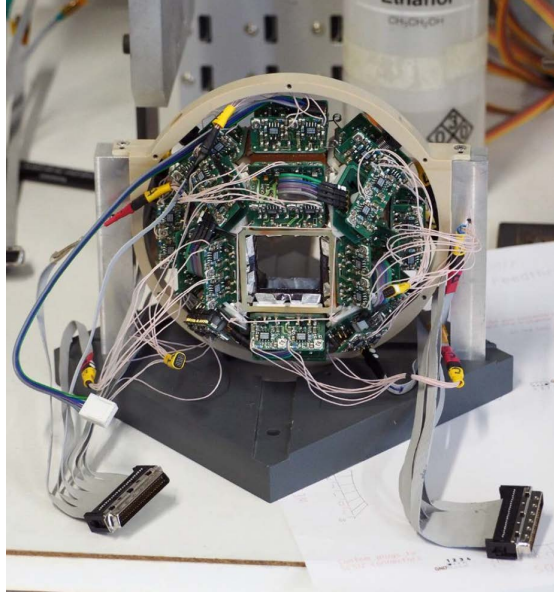
FIGURE 2.13: DIAMANT Array.

A polyhedron geometry was constructed for DIAMANT in 18 square and 8 triangle planes created of single triangle detectors with 10mm thick light guide and sets of 4 square detectors with 14.5 x 14.5 mm^2 as maximum dimension. Between the target and the square planes there is a distance of 32 mm, except in the forward direction, where is replaced by a plane of 8 detectors arranged as a 3x3 array at a distance of 49 mm. The CsI detectors, able to stop completely protons until 25 MeV, have over 70% light-collection efficiency due to a wrapping technique [47]. CsI detectors are able to provide proton discrimination for charged particles using PSA.

In this work DIAMANT is not used as 4π array as the backward angle was removed to do the coupling with the plunger. Three varieties of signals for each detector are derived: the energy, the type of the particle, and a time-reference signal related to the time of the particle-γ coincidence. For deriving the particle type information the zero-crossing method is used, giving the best FoM for the particle discrimination.

2.4.2 DIAMANT coupled to AGATA

Coupling DIAMANT with γ-rays arrays like AGATA enhances the peak-to-background ratio in the performance. The improvement of the statistics is remarkable and also the light charge particle detector permits a good total Doppler shift correction that

is crucial for the improvement of the peak-to-background ratio. Detailed calculations have been developed which establish a number of relations giving the values of the peak-to-background ratio of a γ-transition and the observational limit [46].

2.4.3   Electronics and data flow

The CsI light charged particle detector, DIAMANT, uses as NEDA the NUMEXO2 Digitizer electronics. The particle energy, particle-type and time-reference information are collected for 16 channels by each NUMEXO2 board. The zero-crossing method is applied using a α-proton particle discrimination FoM. For the particle-γ coincidence the timing signals are derived by a non-delay-line Constant Fraction Discriminator. This data is send to the NUMEXO2 digitizers as well as for the NEDA data, using the Virtex 6 for the signal processing and the Virtex 5 for the time stamp and the readout as well. In this case, the readout is done via ethernet instead of the optical fiber of NEDA, since the particle identification is fully done inside the NUMEXO2 board and it is not necessary to transfer the sampled data. The data acquisition is also with the same process of the NEDA one, like it can be seen in the Fig. 2.14. Differently from NEDA, the information from DIAMANT does not participate in the GTS Trigger, nevertheless, all DIAMANT data are timestamped to be able to reconstruct the events and use the particle identification in the analysis process.
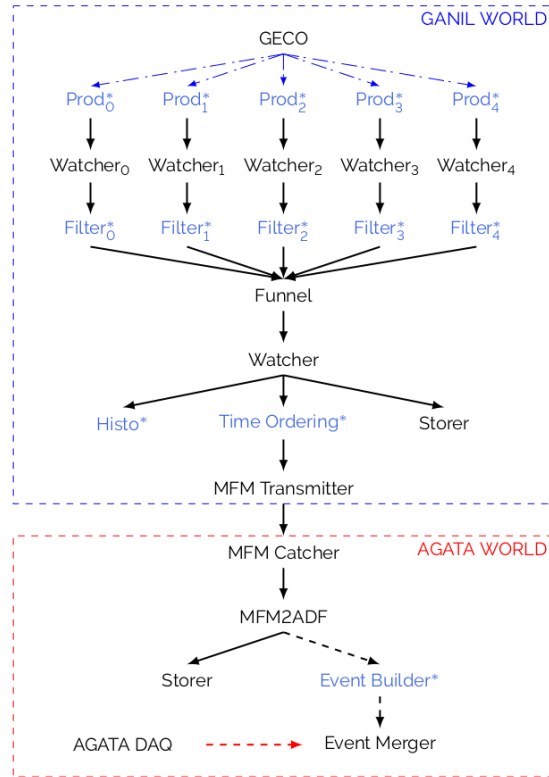
FIGURE 2.14: DIAMANT data flow diagram. There are two network shared by the DIAMANT acquisition system, the GANIL and the AGATA network in blue and red dashed line respectively. The actors marked with an asterisk are actors developed in C++ within the collaboration, in particular the filter following the producers (Prod) contains the NEDA on-line PSA processing, and the others are standard NARVAL actors. The transmission of the data between the two networks is performed by one bridge.

2.4.4 Pulse shape analysis

The identification of the reaction channel requires the identification of the light charged particles emitted. The type and quality of data obtained with DIAMANT is shown in Fig. 2.15. In the figure one can identify the different light charged particles vs. the energy in the left and vs. the counts in the right.

The CsI detectors of DIAMANT have an intrinsic particle discrimination capability, since different particles excite in different proportion the scintillation light components that have different lifetime, completely trigger less. By selecting gates in the charged light particles identifier, the γ-rays corresponding a certain reaction channels could be unequivocally identified and with conditions in the particle time, the random events are well rejected as the same time that improve the selection of the γ-rays corresponding to the reactions.
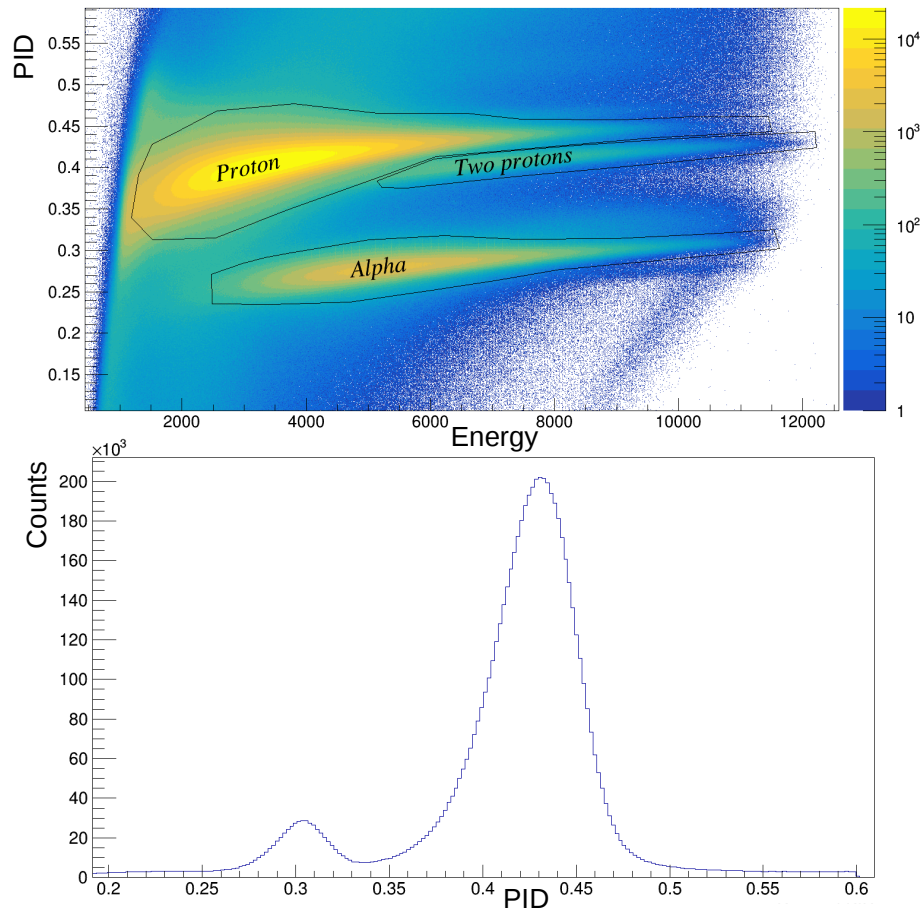
FIGURE 2.15: Illustrative spectra obtained for the particle identification of a DIAMANT CsI detector. PID is shown vs. energy in the left figure and vs. counts in the right figure.

2.5 Plunger

2.5.1 The Orsay plunger device OUPS

The Orsay Plunger Device OUPS [48], shown in Fig. 2.16, as its name suggests, is a plunger device built in the CSNSM in collaboration with the IPN Orsay to do measurements of Recoil Distance Doppler Shift and the Time-Differential Recoil-In-Vacuum.

The Orsay Plunger Device OUPS was developed to be suitable to the different experimental setups and facilities. The plunger device aims at providing a stretched target and stopper or degrader thin foil which are mounted parallel to each other at a variable distance to measure the lifetimes of excited nuclear states in the picosecond range via Recoil Distance Doppler Shift (RDDS) method [49].
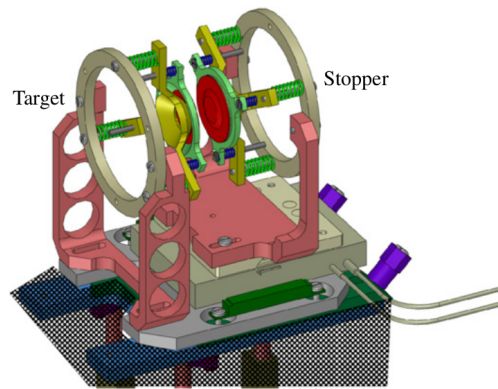
FIGURE 2.16: Three dimensional view of the Orsay Plunger Device OUPS. Figure taken from reference [48].

The nuclear reaction takes place in the target of the plunger device. After, the emiting nuclei produced in the reaction emits γ rays coming from de-exciting nuclear states. These γ rays could be emitted before or after the stopper or degrader foil, therefore, they could be emitted at two distinct velocities. It is feasible to separate the γ rays using the Doppler shift of the γ-ray energys taking into account that the stopped γ rays do not have Doppler shift in the energy (unshifted component) and the ones emitted before the stopper will have a Doppler shift (shifted component). The intensities of these two components are necessary to extract the lifetime of the nuclear state. A lifetime range of one to a few hundreds of picoseconds can be measured using the plunger device with a RDDS method. When performing experiments with this method, the range of target-degrader foil distance, is defined by the recoil velocity of the reaction product and the expected lifetime of the state of interest.

In general for fusion-evaporation reactions, a stopper is used in the Plunger Device after the target. In our work the plunger device was used in differential mode, i.e. a degrader was put after the target to maximize the relation between the peak resolution and the separation between the unshifted and shifted components. As is shown in the Fig. 2.17 a simulation was used to decide the thickness of the degrader. The resolution of the peaks is clearly improved with a degrader instead of a stopper as it can be seen from the spectrum shown in the upper panel (stopper) compared to the others (degrader). The thickness of the degrader is of considerable relevance as well due to the importance of the separation of the two components of the peaks in the RDDS measurements. It can be seen in the figure a better separation of the components when the thickness is the largest, i.e. in the second

spectrum. Accordingly to this simulations, the plunger device was designed with a ^{58}Ni with 1mg/cm^2 target and a ^{197}Au with 5mg/cm^2 degrader.

The Orsay Plunger Device was designed taking into consideration the transparency of the set-up in order to minimize the absorption of the γ rays emitted from the de-exciting nuclei. In the traditional plunger devices this obstacle is solved using a coaxial geometry to place the mechanics far away from the target. However, this geometry is laborious to be coupled with detectors and most importantly, the reaction products must have a small angle relative to the beam. To overcome this variety of inconveniences the Orsay Plunger Device is constructed with a linear piezo motor assembly on which the mechanics for target and degrader foils are mounted. This construction, highly compact, is designed to collect also the outgoing reaction products with large angles respect to the beam line. The base of the plunger is shown in the Fig. 2.18. It is a piezo-electric linear motor, named PI N-661 Miniature Linear Stage, with 20 mm of movement range and 70 mm x 50 mm x 20 mm size. A force of up to 10 N can be achieved by this assembly. The movement is performed by the upper half of the PI N-661, which can be positioned with a precision of 40 nm.

On top of the mentioned PI N-661 Miniature Linear Stage is installed the plunger device as it is shown in Fig. 2.19. The assembly parts are, on one side, a target support frame on top of an aluminium plate and on the other side of the plate a moving degrader supporting the frames over the motor. This moving structure allows to change the distance between the target and the degrader foils from few to some tens of mm with a sub-micrometer precision. The motor is precise to change the position of the degrader foil within some tens of nanometers provided that the plunger rigid structures have to do feedback movements. The OUPS Plunger Device gets stretched the target and degrader foils by using a mechanism that allows to pull the foils over metallic cones machined with high precision as shown in Fig. 2.20. A good stretching is necessary in order to have a precise definition of the distance between target and degrader foils. The parallel adjustment of the target and degrader frames uses three screws attached to the stretcher cone and to the rings used to fix the assembly with the plunger device.
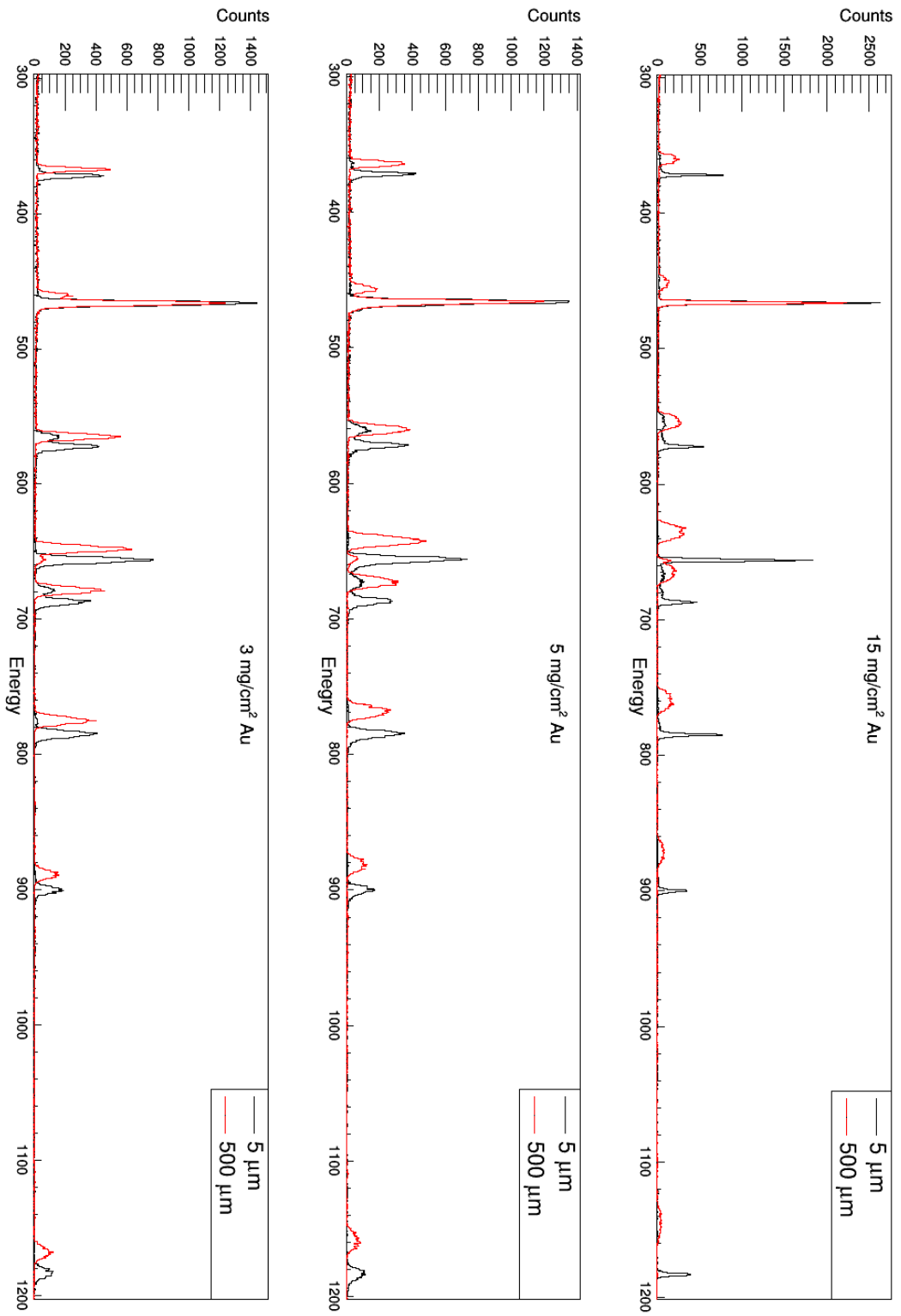
FIGURE 2.17: Simulation for the stopper/degrader comparison and the thickness. A stopper of 15 mg/cm^2 Au is set in the first spectrum. A degrader of 5 and 3 mg/cm^2 is set in the second and third spectrum respectively.
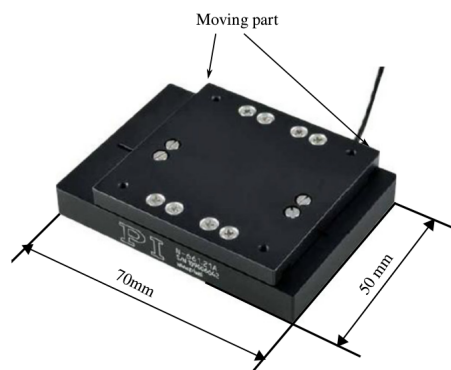
FIGURE 2.18: The PI N-661 Miniature Linear Stage. Figure taken from reference [48].
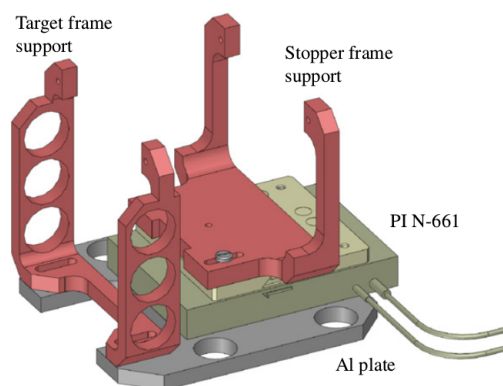
FIGURE 2.19: Core of the Orsay Plunger Device. Figure taken from reference [48].
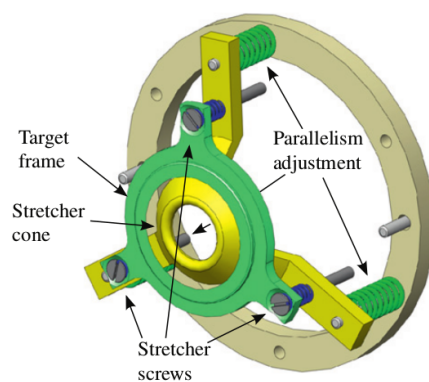
FIGURE 2.20: Target frame and stretch cone. Figure taken from reference [48].

2.5.2 The plunger device coupling to DIAMANT

The plunger device is a passive tool which has a mechanic coupling with the light particle detector DIAMANT, shown in Fig. 2.21, contained within the reaction

chamber. The device was designed to make DIAMANT detector array as efficient as possible.

In order to do that the geometrical center of DIAMANT was displaced forward when coupled with the plunger, effectively using only the half of the solid angle forward. It is relevant to comment that, due to the kinematics of the reaction, the detection efficiency and discrimination capability are significantly larger in the forward half of the solid angle covered by this DIAMANT configuration.
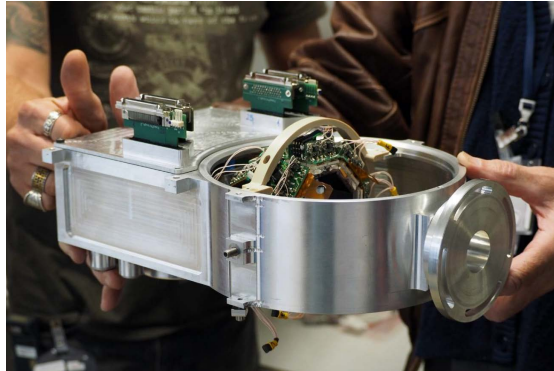
FIGURE 2.21: The Orsay Plunger Device OUPS coupled with DIAMANT.

2.5.3 Feedback system

For short lifetimes measurements a feedback system to achieve stability in the target-degrader distance is necessary. The feedback system was tested in an experiment performed at the IPN Orsay Tandem accelerator laboratory using the Orgam germaniun detector array [48].

The electronic feedback system is in charge of correcting the changes in the target and degrader foils due to the target-beam interaction. It is so important to correct when short lifetimes are measured because these changes in the foils could be relevant in comparison with the distance between them. In order to do the correction, the two foils are used as a capacitor and, therefore, the capacity value changes as a function of the distance between them. The feedback system involves a high-precision pulser of type BNC Model PB-5, a spectroscopic amplifier Ortec 571, an impedance matcher circuit, a National Instruments BNC-2110 BNC adapter, and a National Instruments PCIE-6361 X Series DAQ, a PCI express card mounted in the control PC. A variation of 2.5% in the FWHM was detected with

changes in the ambient temperature. The PI N-661 linear stage was controlled by the PI E-861 Controller, connected to the control PC via a USB interface. A schematics of the electronics used to control the Orsay Plunger feedback system is shown in Fig. 2.22.
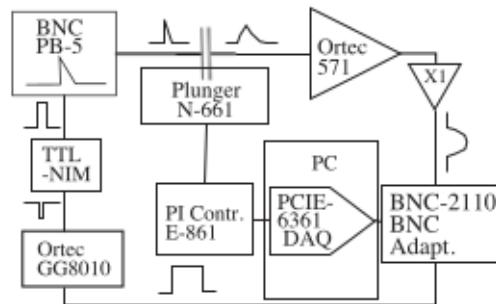
FIGURE 2.22: Schematics of the electronics in the Orsay Plunger Set-up. Figure taken from reference [48].

A LabVIEW application controls the feedback system which supervises the sampling of the output of the Ortec 571 amplifier via the PCIE-6361 DAQ board, an online processing to extract the pulse-height at the output of the Ortec 571 amplifier, a closed loop feedback controlling the PI N-661 to keep the capacitance as stable as possible and a slow control of the plunger system modifying the target-degrader foil distance, starting and stopping of the feedback, loading and saving configurations, and security functions.

Chapter 3

Experimental conditions

3.1 Introduction to the experimental activity

This experiment was performed in the first AGATA, NEDA-NW, and DIAMANT campaign in 2018. The set-up included a plunger device for the determination of the lifetimes of interest with the RDDS technique that will be described later.

The most adequate reaction mechanism to populate excited states in neutron-deficient nuclei, using stable beam and target, is the fusion-evaporation. In the following paragraphs, an introduction to the reaction mechanisms and specifically to the one used for this experiment will be presented.

3.2 Reaction mechanism

Nuclear reactions between an accelerated projectile and a target can be classified according to the energy in center of mass and impact parameter, that define the possible reactions that may occur.

The reaction mechanism is use to populate the nucleus of interest in an excited state or to excite the nucleus of interest. The reaction mechanisms at energies around the Coulomb barrier, possible at different ranges of the impact parameter b, are schematically represented in Fig. 3.1.

When the impact parameter b is larger than the sum of both nuclear radius (projectile and target) mainly elastic scattering takes place and only inelastic Coulomb
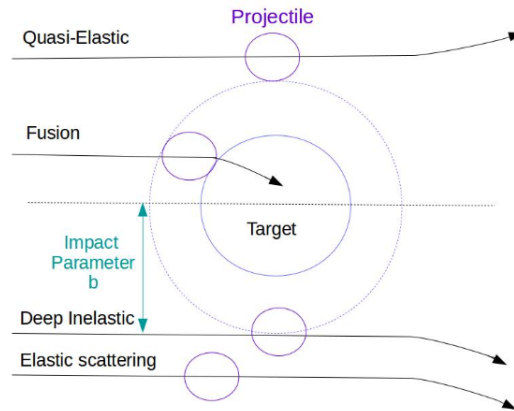
FIGURE 3.1: Heavy-ion collisions classification according to the impact para-
meter.

excitation may appear. The reaction mechanisms from nuclear inelastic excitations
and quasi-elastic reactions to deep inelastic collisions are occurring when the im-
pact parameter is decreasing. For lower impact parameters, fusion reactions arise
generating a compound nucleus which fissions or, by means of liberate energy with
the evaporated particles, produces the residual nucleus in a fusion-evaporation re-
action. The fusion-evaporation reaction is the one used in this experiment to
populate the nucleus of interest and will be described in more detail in the follow-
ing section.

3.3 Fusion-evaporation reactions

As it was explained above, the fusion-evaporation reaction mechanism occurs when
the accelerated projectile and the target nuclei have a large overlap and the energy
is above the Coulomb barrier. After the fusion of both nuclei, a compound nucleus
is formed as a system with the energy of the reaction which, if there is not fission,
it is liberates via the particles evaporation, tipically neutrons, protons and alphas.
After the evaporation process, the reaction product nucleus de-excites by γ-ray
emission.

Fig. 3.2 [50] shows schematically the production of the compound nucleus, which
loses memory of its origin from the beam and target to conform itself with the
sum of the neutrons and protons of target and projectile. Then, in the time scale
of 10^{-19} seconds evaporates light particles. In the residual nucleus, high excited

states with high angular momentum are populated in the particle evaporation process and after γ-ray emission until the nucleus arrives to the ground state.
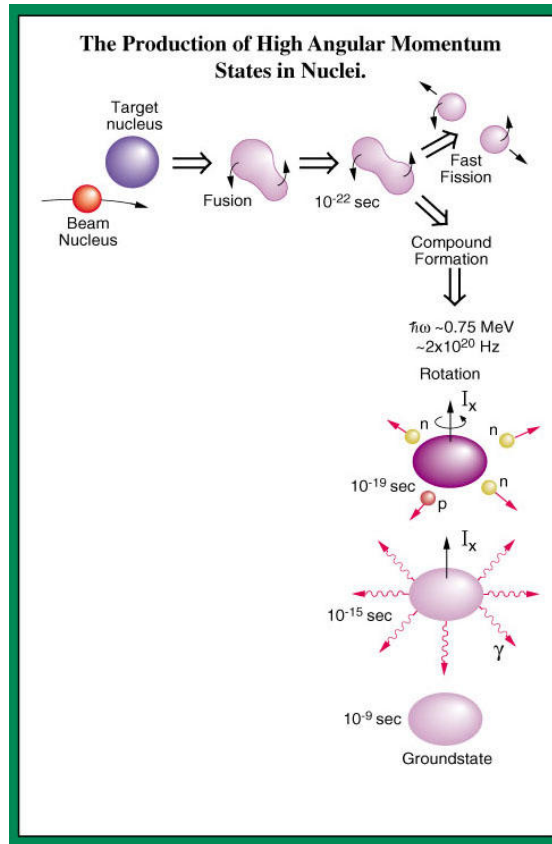
FIGURE 3.2: High angular momentum states in nuclei production.

3.4   Cross sections

As mentioned in the previous chapters, a fusion-evaporation reaction, aiming at producing the ^{112}Xe nucleus, was performed with the ^{58}Ni beam, delivered by the GANIL accelerator complex with an energy of 250 MeV. The beam impinged into the ^{58}Ni target with 1mg/cm^2 thickness that was followed by the Plunger degrader foil. The γ-rays were measured with AGATA [14] in coincidence with the neutron array NEDA-Neutron Wall (NW) [32, 35] and the charged particle detector DIAMANT [46] coupled to the OUPS plunger device [48].

The experiment was performed with a trigger condition of one neutron identified in NEDA-NW in coincidence with at least one γ-ray in AGATA. The average beam current was measured to be 4 particle nA, i.e. 32 electrical nA with a ^{58}Ni

charge state of 8. This trigger allows to avoid 90% of unwanted reaction channel detection.

Generally, in the neutron-deficient side of the Segrè table, at energies close to the Coulomb barrier, with stable beams and targets, the fusion-evaporation reaction provides the higher production cross sections. In our case, the nuclear reaction conditions, i.e. the projectile-target combination and beam energy, were selected to have the maximum cross section of our reaction channel of interest, the ^{112}Xe nucleus. The estimates for the fusion-evaporation cross sections are calculated with the Statistical Hauser-Feshbach theory. In this theory, after the formation of the compound nucleus at a calculated angular momentum and excitation energy, the emission of particles and γ-rays is estimated using transmission coefficients, level densities and emission probabilities. Well known software modeling the statistical theory exist and in this thesis both PACE4 [51] and HIVAP [52] have been used, finding the best agreement using HIVAP. The statistical calculation provides the cross section estimates for the main reaction channels with the fusion evaporation reaction, mentioned before, that are summarized in table 3.1.

The reaction channels populated by the reaction are shown in Fig 3.3. As it is explained before, even if there is a large number of channels populated with sizable cross section, the one neutron trigger reduces largely the contribution of these channels to the acquired data. The particle selection when constructing the γ-γ coincidence matrices also helps to reduce further the contribution of other reaction channels than the one of interest. By comparison the statistical calculation with the analysis spectra, the most populated evaporation residues are the ^{112}Te (4p) and ^{112}I (3p1n). The ^{112}Xe cross section in the statistical calculation is approximate. The experimental cross section estimates from previous experiments, dealing with the ^{112}Xe energy level scheme, was about 100 μb, in fair agreement with the HIVAP calculation.
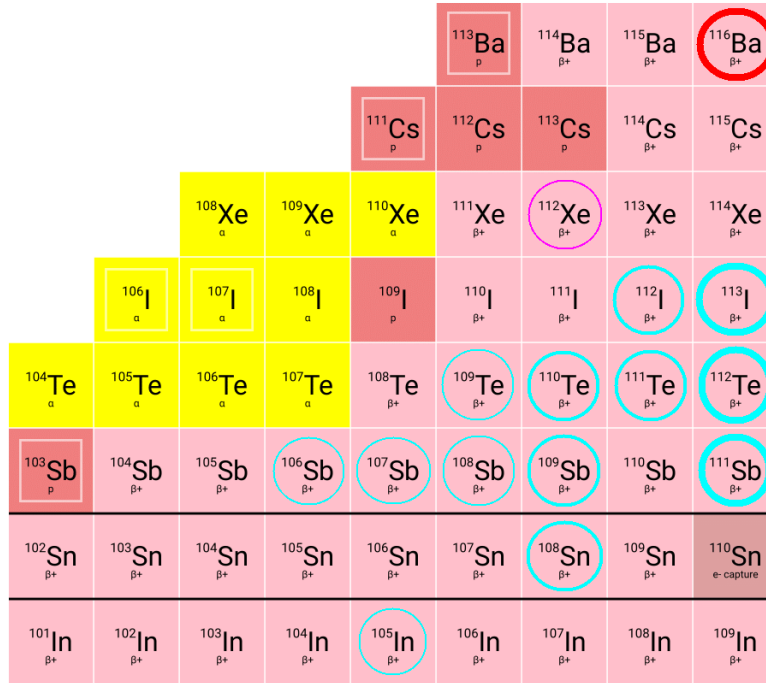
FIGURE 3.3: Nuclide chart showing the compound nucleus inside a red circle, the interested nucleus in purple and the reaction channels in cyan. The width of the circles is proportional to the cross section.

TABLE 3.1: List of reaction channels cross sections calculated with HIVAP software for the reaction ^{58}Ni + ^{58}Ni with the compound nucleus ^{116}Ba.

Z	N	Particles evaporated	A	Percent (%)	cross-section (mb)
52	60	4p	^{112}Te	25.34	147
53	60	3p	^{113}I	23.28	135
51	60	5p	^{111}Sb	13.69	79.4
50	58	α4p — 6p2n	^{108}Sn	5.02	29.1
51	58	α3p — 5p2n	^{109}Sb	4.83	28
52	59	4p1n	^{111}Te	4.72	27.4
52	58	α2p — 4p2n	^{110}Te	2.81	16.3
53	59	3pn	^{112}I	2.34	13.6
50	56	2α2p — 6p4n	^{106}Sn	0.67	3.86
51	57	α3pn — 5p3n	^{108}Sb	0.42	2.45
52	57	α2pn — 4p3n	^{109}Te	0.4	2.34
49	56	2α3p — 7p4n	^{105}In	0.22	1.28
51	56	2αp — 5p4n	^{107}Sb	0.11	0.623
54	58	2p2n	^{112}Xe	0.09	0.5

An example of the trigger selectivity is shown in Fig. 3.4, where the runs with and without the neutron trigger condition are compared. At least one proton condition in DIAMANT was used. In the run measured with the trigger condition it can be observed that the 3p and 4p reaction channels, the two most populated in the

experiment, are largely suppressed and therefore the 3pn and 4pn channels are enhanced.
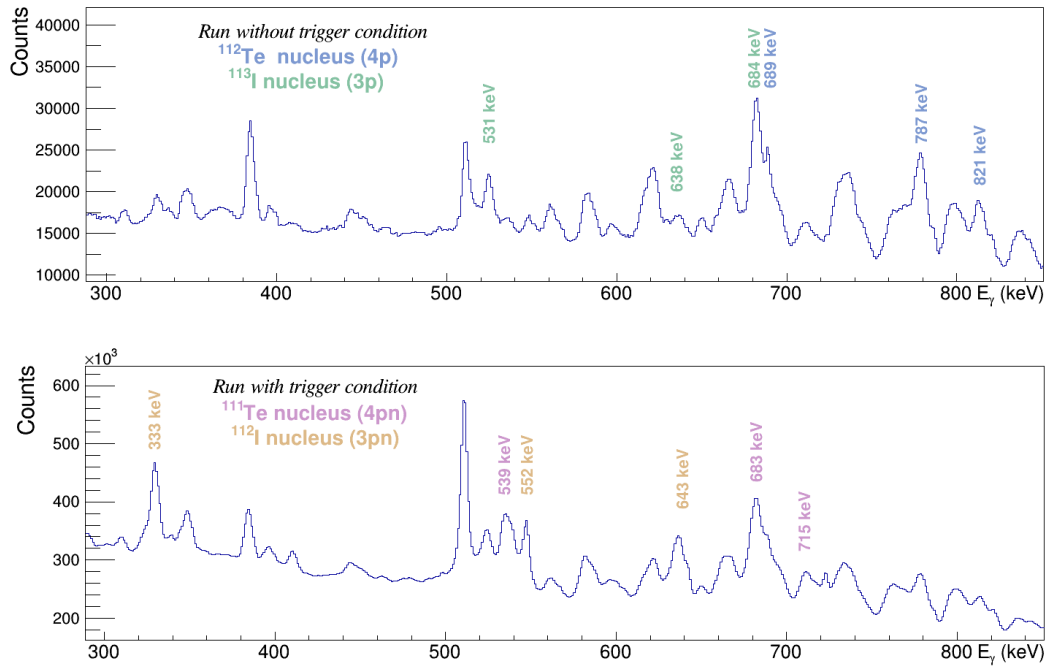
FIGURE 3.4: Runs comparison with (below) and without (above) the one neutron trigger condition.

3.5 AGATA efficiency

A calibrated ^{152}Eu source was used to determine the absolute efficiency of AGATA detector when using tracking. In general the description of the efficiencies in systems of Ge detectors is complex and empirical functions, that describe the logarithm of the efficiency as a function of the logarithm of the γ-ray energy, are normally used 3.1. In the present case the efficiency function used to correct the measured γ-ray areas is taken from the Radware software [53]. The final calibration is shown in the Fig. 3.5.

The determination of the absolute efficiency requires a calibrated activity ^{152}Eu source, in our case, at the moment of the experiment, the source had an activity of 150534 (3011) Bq.

$$\epsilon_{peak}(E_\gamma) = exp[(A + Bx + Cx^2)^{-G}] + (D + Ey + Fy^2)^{-G}]^{-\frac{1}{G}}, \qquad (3.1)$$

$$\text{being } x = \log(\frac{E_\gamma}{100keV}) \qquad (3.2)$$

$$\text{and } y = \log(\frac{E_\gamma}{1000keV}) \qquad (3.3)$$

In this function the parameter C is fixed to zero [53] and the free parameters A,B,D,E,F and G were used for the calibration (see table 3.2) where the low and high range energy is taken with different expression. In the case of energies lower than 200 keV there is a decrease of the efficiency due the rejection of the single interaction events in the tracking algorithm to improve the P/T ratio.

In previous experimental activity with DIAMANT, the detector was using a 4π configuration surrounding the target which causes absorption in the low energy region, at 121 keV. In this experiment the target is not surrounded by DIAMANT and the AGATA detector is facing the target side without DIAMANT detectors, nevertheless, there is absorption of low energy γ-rays due to the plunger mechanics. The ^{152}Eu source was placed intentionally between the target and degrader foils to measure the efficiency.

TABLE 3.2: Calibration parameters used in the efficiency calibration fit curve.

A	B	C	D	E	F	G
4(5)	12.0(14)	0	1.506(11)	-0.39(2)	-0.06(3)	1.5(0.3)
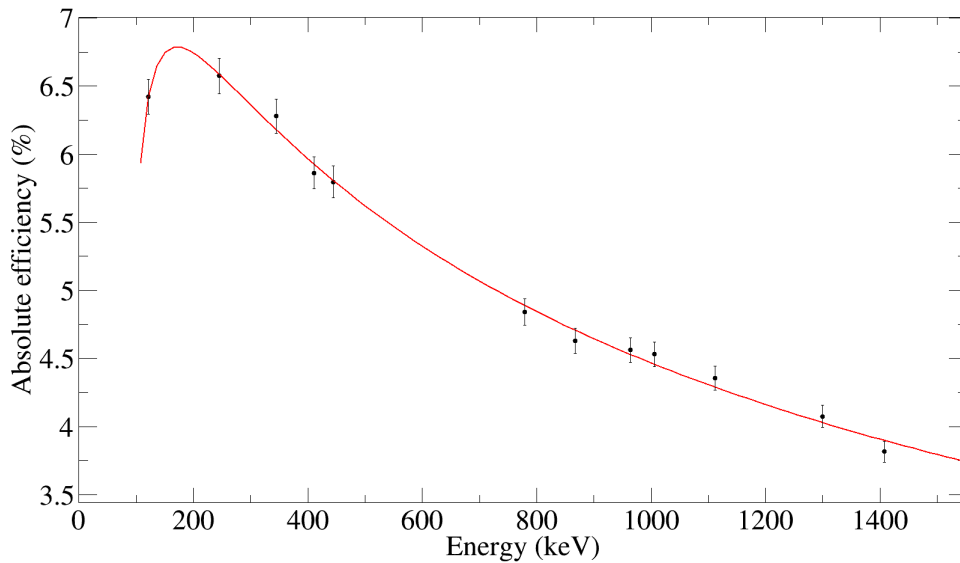
FIGURE 3.5: Absolute efficiency curve using a ^{152}Eu source.

3.6   NEDA-NW and DIAMANT efficiencies

Two quantities are relevant when describing the performance figures of NEDA-NW, namely the Neutron discrimination and identification efficiency and second the neutron-γ discrimination factor. Additionally, there is a third factor, the crosstalk effect which introduces ambiguity in the determination of the real neutron multiplicity. Measures have been taken to minimize this effect (see Chapter 4.3.2).

The neutron detection efficiency was determined using a run without the one-neutron trigger condition. It has been calculated using the 3p1n reaction channel, leading to ^{112}I, because is the nucleus with the highest cross section for a reaction channel involving neutron emission. To have a cleaner spectra, the 7^- to 5^- transition of 333 keV was used to set a coincidence condition while the efficiency was measured using the 11^- to 9^- transition of 552 keV.

The areas summarized in table 3.3 were used, i.e. the area of the 552 keV transition when applying proton + 1 neutron condition divided by the area of the same transition when at least one proton condition is applied. The final result was excellent, with an efficiency of $n_{eff} = 30(6)\%$.

We call neutron-γ discrimination factor to the suppression factor of the γ-rays, emitted by a nucleus corresponding to a reaction channel without neutron emission, in the one neutron selected spectrum with respect to the spectrum without

TABLE 3.3: Areas used to measure the NEDA efficiency using the 11^- to 9^-, 552 keV transition in ^{112}I.

Particle condition	Area (counts)
1n1p	100(13)
At least 1p	333(49)

neutron condition. It is an indication of how well our PSA algorithm works.

A neutron-γ discrimination factor of 4(2) per mil (i.e. about 1/250) was obtained comparing spectra without neutron trigger condition using the 0n4p and 1n4p particle conditions. This factor was determined using the 689 keV transition, 2^+ to 0^+ in the 4p reaction channel, that corresponds to the ^{112}Te nucleus.

The neutron-γ discrimination is different in NEDA and NW as it can be noticed in Fig. 3.6. The PSA (see chapter 2) in NEDA is performing better to discriminate between neutrons and gammas because NW, located at 90 degrees, is composed of older detector and provides a worse neutron-γ discrimination by PSA, more likely due to the lower light yield in the detection process.
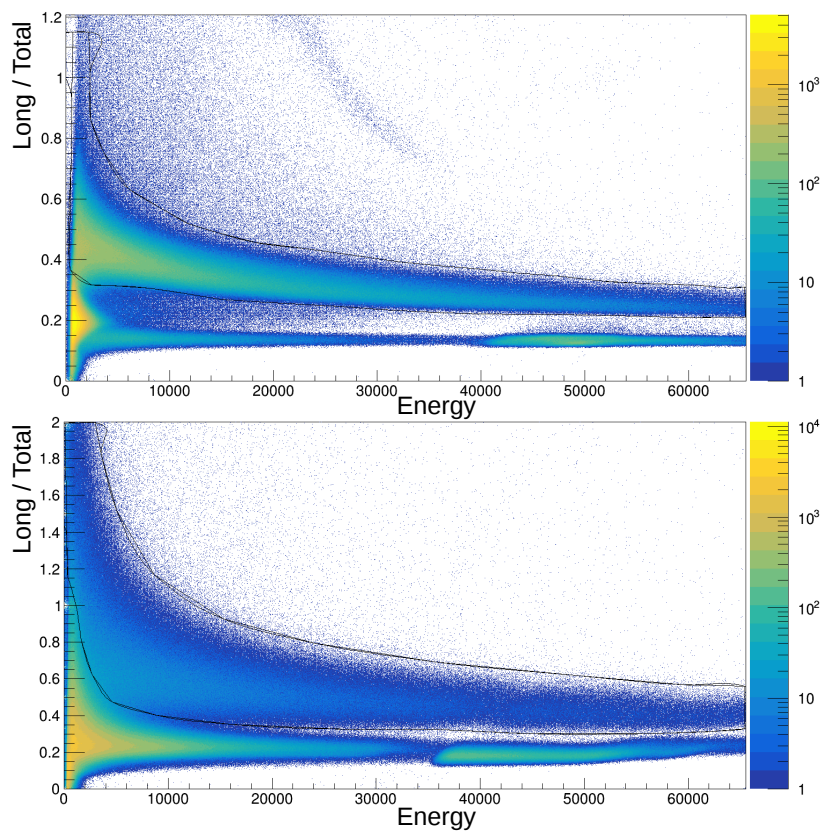
FIGURE 3.6: Neutron-γ discrimination comparison in NEDA and NW.

The proton efficiency is also important since the detected protons are used to select or identify the reaction channel under consideration. The probability of detecting a number x of protons when a number n of protons has been emitted in the reaction ($x \leq n$) is given in the equation 3.4.

$$P(x) = \frac{n!}{(n-x)!x!}p^x(1-p)^{n-x} \tag{3.4}$$

Being x the number of protons detected, n the total protons emitted and p the proton detection efficiency. This binomial distribution is used to calculate the proton efficiency in the 3p1n channel reaction. For this purpose, it is used the areas ratio of the 210 keV transition between three and two protons strict conditions, as shown in table 3.4. With this values the proton detection efficiency of DIAMANT is determined to be 31(4)%.

The proton efficiency for this experiment is reduced respect to the standard DIAMANT efficiency, but it has to be taken into account that this experiment has been performed with a reduced configuration of DIAMANT in order to make it compatible with the use of the OUPS plunger device.

TABLE 3.4: Areas used to measure the DIAMANT efficiency using the 210 keV transition in ^{112}I.

Particle condition	Area (counts)
1n3p	4320(52)
1n2p	29560(139)

The particle identification in DIAMANT is working well and it is shown in Fig. 3.7. The figure also shows the detection of scattered light ions, probably ^{12}C or ^{18}O, in the detectors closer to the beam axis. However, this does not influence the particle selection due to the gates performed during the data analysis.
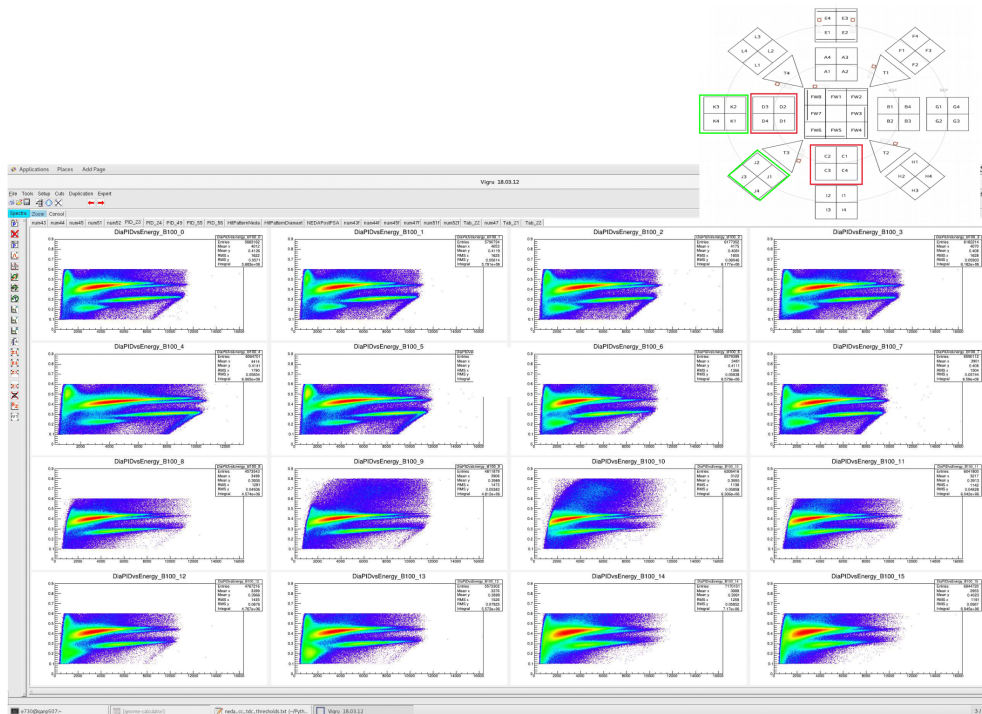
FIGURE 3.7: Particle identification in DIAMANT.

3.7 Plunger distances

To measure the range of lifetimes of the transitions of interest in our nucleus is decisive to have well determined the real distances of the plunger from the target to the degrader. For this purpose, the plunger contains a feedback system described in the section 2.6.3.

Due to the high beam current in the plunger and some problems with the Lab-View software which controlled the plunger, sometimes was necessary to run the feedback system manually. Because of that, an offline calibration of the distances had to be done.

The distances between the target and the degrader used in the experiment were ranging from 20 to 1500 μm.

For the lowest distances between 20 and 40 μm there were almost no fluctuations and for the highest ones between 200 and 1500 μm the variation of the nominal distance is less relevant for the determination of the lifetime. Between 50 and 100 μm is more problematic and a there is a loss of statistics. In the Fig. 3.8 it is shown the calibration of the data for each distance, going from top; 20 μm, 40

μm, 70 μm, 100 μm and 200-1500 μm respectively by gating on the time with a standard clock reference.
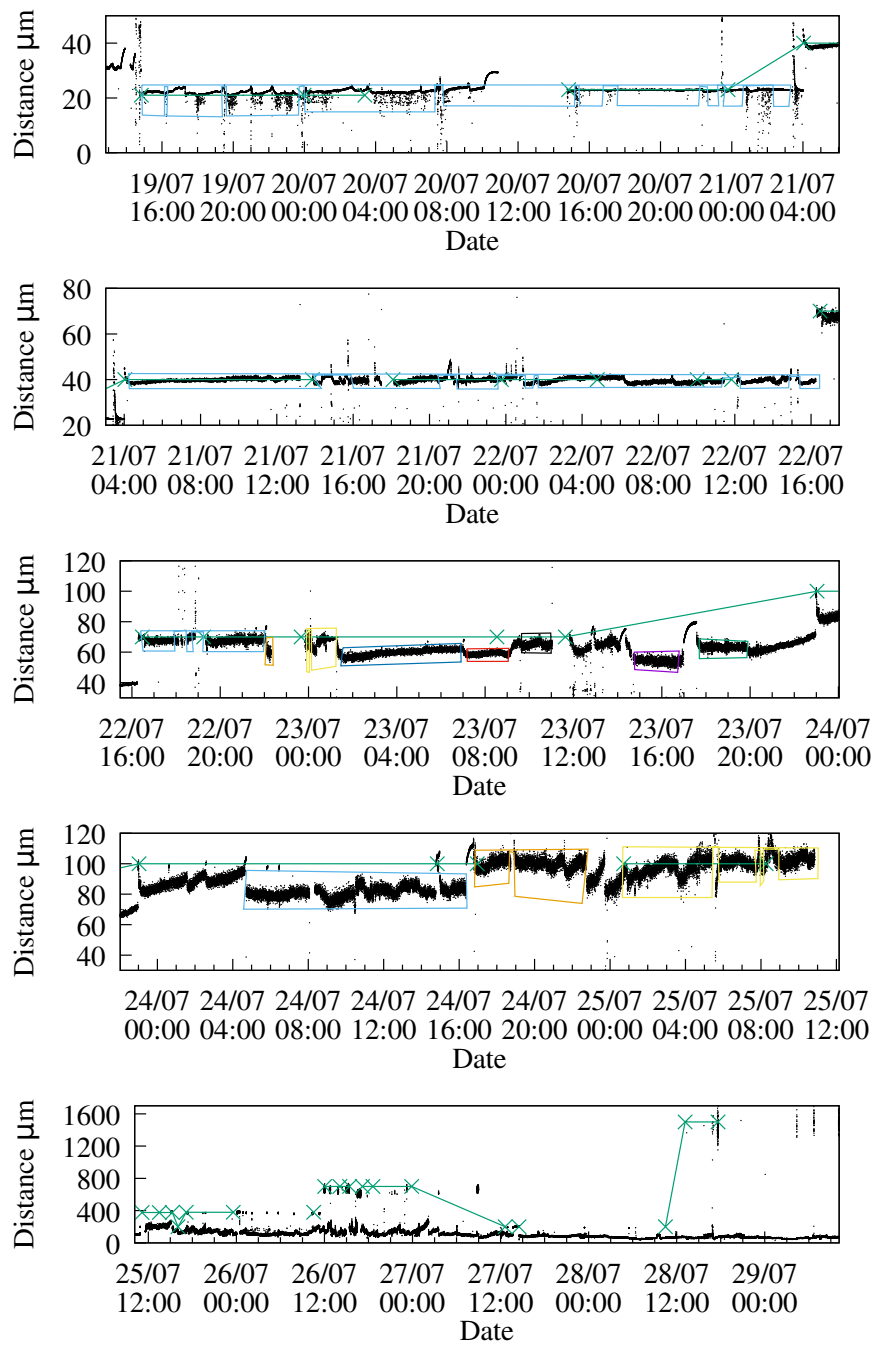
FIGURE 3.8: Plot of calibrated distance measurements and foreseen distances. From the top, 20 μm, 40 μm, 70 μm, 100 μm, and 200-1500 μm.

The time intervals of each distance are shown in Fig 3.9 and the final distances were extracted as the mean and rms of these histograms. The gates done mentioned above are summarized in table 3.5 and also the time of the beam running lost in each one due to the fluctuactions in the distance. Futhermore, checking this gates, some of them had to be removed because there was not enough statistics to conform a single distance. Specifically, the distances 4, 5 and 6 were removed.
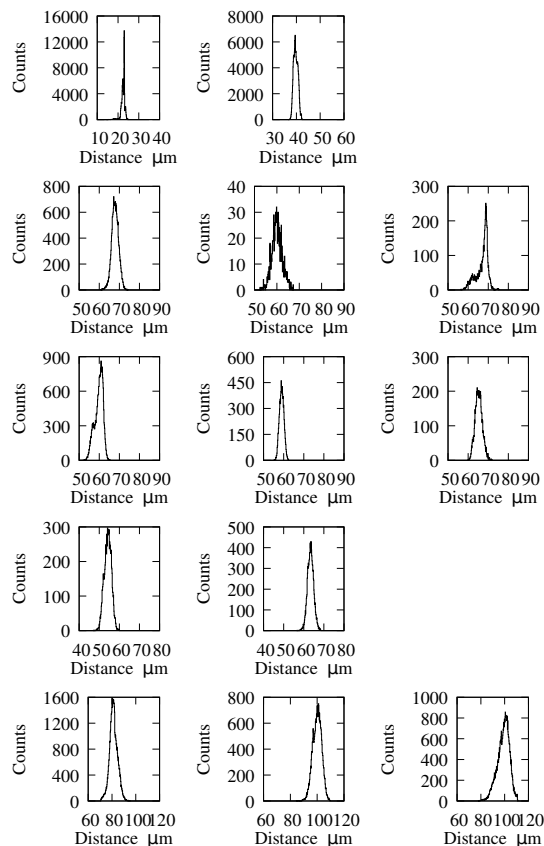
FIGURE 3.9: Histograms of measured distances for the different gates used for calculating the distances.

TABLE 3.5: Plunger distances gated.

Gate	Plunger distances (um)	Total time gated	Total time lost
1	22.44	25h 24min	5h 43min
2	39.68	28h 09min	5h 23min
3	66.67	9h 07min	8h 10min
4	59.57	1h 31min	3min
5	54.18	1h 57min	4h 08min
6	63.31	2h 09min	3h 09min
7	81.23	11h 46min	5h 47min
8	99.35	14h 08min	2h 57min

The 9 distances finally taken into account for the lifetime analysis are shown in table 3.6. The distance with the shortest time of measurement was 67 μm with around 9 hours in total. In some occasions, the data with less statistics have been removed from the lifetime determination fit.

TABLE 3.6: Final distances.

Plunger distances (um)	Time
22.4(0.9)	25h 24min
39.7(0.9)	28h 09min
67(5)	09h 07min
81(3)	11h 46min
99(6)	14h 08min
200(15)	18h 47min
380(15)	18h 08min
700(15)	22h 31min
1500(15)	20h 43min

Chapter 4

Data analysis

4.1 AGATA data processing

In this section I will describe the AGATA data analysis which comprises from the local level processing until the tracking filter with two mainly subdivisions; the local and the global level analysis of the data.

An accurate processing including all the corrections and calibrations is particularly relevant for RDDS lifetime measurements as the present one, since it affects the energy resolution. The scheme of the data processing is shown in Fig. 4.1 and it will be explained in the following sections.

4.1.1 The Local level processing

The Local Level processing of the AGATA data is performed at two distinct times with clear differences. During the experiment it is performed in the on-line (or near-line) mode and it is a fundamental ingredient of the monitoring of the on-going measurement. After concluding the experiment, it is performed off-line including further checking of the parameters as well as the Post-PSA filter, that is described in the following sections.
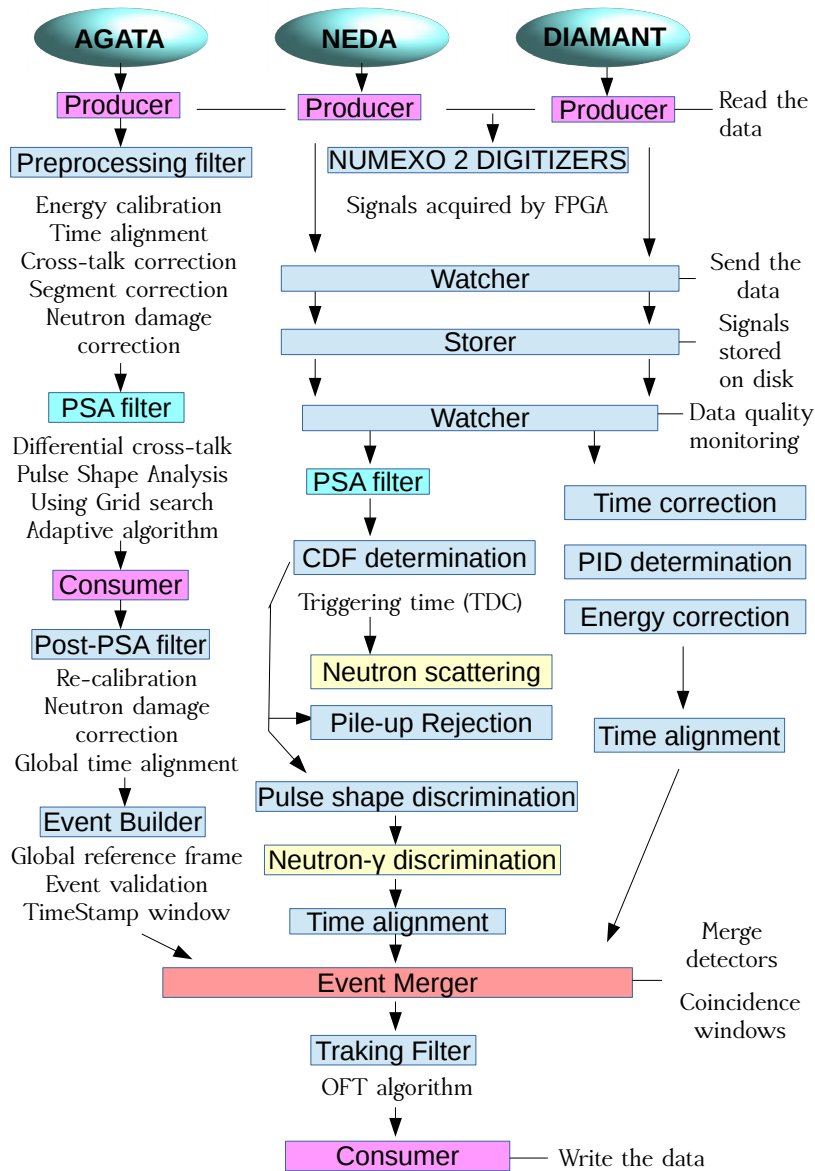
FIGURE 4.1: Scheme of the AGATA, NEDA and DIAMANT data processing.

4.1.1.1 Local level processing through the experiment

In the present experiment, the high counting rate and multiplicity, prevented the detector traces to be stored, thus the local level processing during the experiment included the final determination of the interaction points of the γ-ray in the detector segments determined with the PSA. The accurate PSA requires that energy and time calibrations as well as cross talk corrections are properly done on-line. The PSA performed on-line is necessary to provide the interaction points in the

detector. Some of the corrections, as the neutron damage, require the PSA information and are performed in the Post-PSA filter, that will be described in the following subsection.

In our study is important to get the best energy resolution in order to determine correctly the areas of the two RDDS components of the γ-ray. In order to do that it is fundamental to reconstruct the sequence of interactions using the PSA information and the tracking algorithm. The Doppler correction is then performed knowing the first interaction point.

It is important to remark that the initial energy calibration, performed at the beginning of the experiment, has to be redone in particular checking for small variations over the time of the experiment. Energy calibration performed during the experiment will need a more precised recalibration for most of the segments of each detector. This will be explained in the following subsection.

The energy calibration was automatically done employing the RecalEnergy program [54] in the 36 segments with a shared core contact in each AGATA detector, searching in the energy spectra and executing a Gaussian fit for the γ-ray peaks using a linear fit fixing the offset to zero.

^{60}Co and ^{152}Eu Sources in front of AGATA were employed for the energy calibration of the each segment of the AGATA detector (36 segments) and the two signals with different gain outputs from the preamplifier of the central core. The obtained energy calibration coefficients were applied to all the channels in this experiment, $(36 + 1 + 1) \times 34 = 1292$ channels. The energy calibration of each segment is also used to scale the amplitude of the recorded traces for the PSA.

The crosstalk is another effect that has to be taken into account since it implies signal deformation and requires corrections. The crosstalk is partly due to the closely packed circuitry of the detector and analog electronics, but also is connected with the use of an AC coupled preamplifier. Two crosstalk corrections are performed on the signals, namely the "proportional" Crosstalk and the "Derivative" or "Differential" crosstalk. The proportional crosstalk effect consists on the fact that when two or more segments in the same crystal have net charge, the summed energy is smaller than in the case when only one segments had net charge. This effect is almost linear with the number of firing segments, namely the multiplicity [55]. The Derivative or Differential crosstalk affect the segment

signals during the risetime and the correction is of paramount importance for a correct PSA [29].

The acquisition of the crosstalk correction coefficients was achieved with the sorting of the energies of the segments in reference to the numbers of firing segments and deducing the shift from the nominal energy of the two principal transitions in the ^{60}Co source.

The xTalkSort code [54] generates the cross talk matrices, used in the measured energies correction and the restoration of the baseline. Also, the inverse of the cross talk correction matrices are used during the PSA analysis.

The AGATA sub-arrays easily reach thousands in number of segments and therefore corresponding electronic channels. With such numbers it is not uncommon that segments are not present in the data due to malfunctioning. There are some other corrections which should be done for some damaged segments grouped as broken, lost or unstable that could be recovered or dismissed if it is not possible to apply the correction. To perform the correction in broken segments, the core energy is used since it corresponds to the sum of all segments energies in the detector. The xTakSort mentioned above is used for that purpose in each case. In this experiment the broken segments were the E6 segement of 00A detector, the B3 segment of 01B detector and one lost segment was C1 in 11A detector.

Futhermore, to perform a reliable PSA for the interaction points of the γ rays, the time of all the segments has to be aligned to the core time. Subsequently, it is relevant a precise time alignment correction. With the core as trigger, the alignment coefficients for the time for all segments in each detector are obtained. Those coefficients will be used to align every signal. Thereafter at the level of the Post-PSA the time alignment correction will be applied again.

The PSA algorithm applies different time shifts on the traces around TZero reference as a way to determine the best time for a given interaction. The final time reference considers the sum of the net charge time and the core time. However, this reference depends on the PSA database and the time references have to be aligned to each other afterwards.

The Pulse Shape Analysis is used to determine the interaction positions of the γ rays which is crucial for the reconstruction of its path through the detector. This analysis was accomplished with the PSA Filter actor using the Adaptive Grid

Search algorithm [26]. This algorithm compares the experimental signals with the calculated ones using a minimization procedure with a variable grid, in order to optimize the processing time.

Finally, as part of the local level processing done during the experiment, it was included the neutron damage correction, that uses the PSA position information. Nevertheless, the neutron damage correction required improvements in the offline analysis and, therefore, it will be described in the following section.

4.1.1.2 Post-PSA filter

As mentioned before, during this experiment we resorted to the on-line PSA to avoid the recording of all the detector traces, thus, the corrections required for the PSA were as well performed on-line and this was our starting point for the off-line analysis were is extensively used the so-called Post-PSA filter. The Post-PSA filter includes the energy re-calibrations, neutron-damage corrections and detector time alignment performed after the experiment.

Regarding the neutron-damage corrections, it is well known that defects in the crystal lattice appear when the fast neutrons, i.e. MeV neutrons, interact with the germanium crystal. The AGATA detectors have large size and therefore a high probability of the charge carrier being trapped. The Neutron Damage (ND) in the energy signal is due to a long exposition to fast neutrons. This exposition produces defects in the AGATA detectors which appear as electron or hole traps. Due to the lower mobility of the holes compared with the electrons, the neutron damage appears more first in the segment signals. Trapping of charges (electrons or holes), causes an incomplete charge collection and it shows up in the γ spectrum with a tail on the low energy side of the peaks as can be seen in Fig. 4.2. The neutron damage correction reconstructs the energy of the tail inside the peak by means of an estimation of the mean free path of electrons and holes considering the shape of the signals using the program SortPsaHits [54]. For this work all the detectors besides the 1A, 3A, 3B and 3C were corrected. The improvement after the correction is shown in Fig. 4.2 as the blue line.

Once the neutron damage correction is applied to the best of our ability, the ultimate energy calibration is implemented at this level in the same way explained in the previous subsection, since it could be an erroneous determination of the
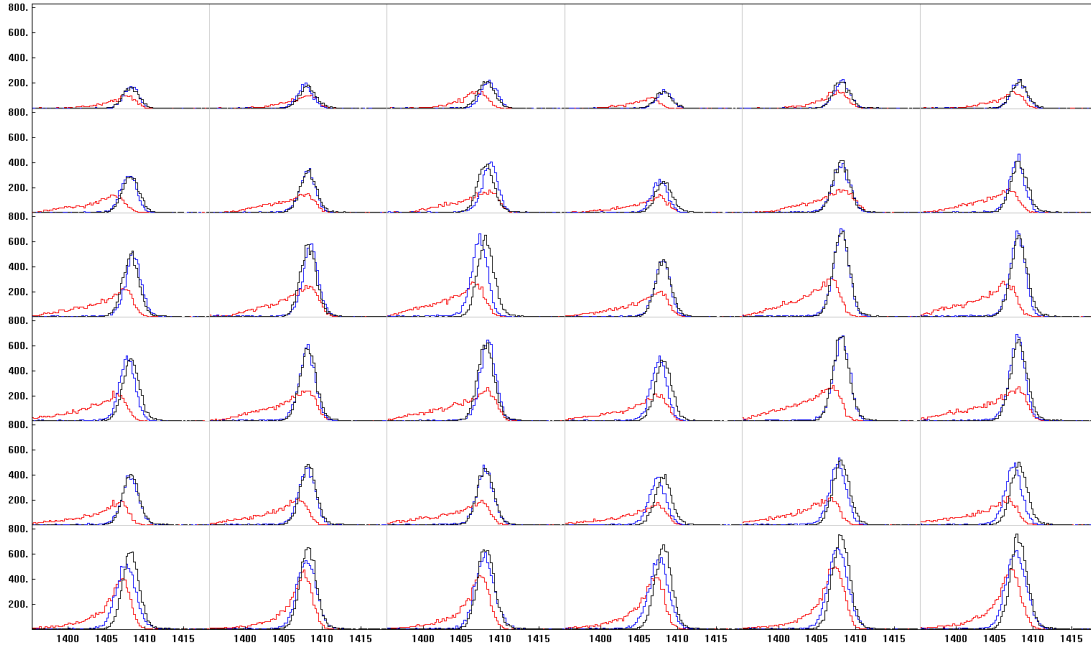
FIGURE 4.2: γ spectra showing counts vs energy, with PSA data as the red, ND corrected data as the blue and the black line as the data after the final energy correction.

peak energy centroid originated by the deformed shape of the peak. This latter correction was performed when only nominal and the corrected peak centroid had equal or larger than 0.3 keV energy difference.

The application of the energy calibration coefficients in all the channels produces the peak correction shown in Fig. 4.2 (black). The back segments of the detectors in the figure correspond to the row with lower intensity in the γ peaks.

In this experiment the sum energy of all segment was forced to be equal to the energy measured in the core with the ForceSegToCore option in the algorithm unless for the 05B detector for which the core resolution obtained was not acceptable at low gain and therefore the option was avoided for the last three runs.

While improving the resolution, using the option of forcing the energy of the segments to the core has the disadvantage that at high counting rates the core signal suffers more pile-up than the segments. In our case the usage of the sum of the segments is the suitable option since clearly it improves the FWHM of the peaks. The last action performed in the Post-PSA filter of the local-level processing is the alignment of the time of the different AGATA crystals core signals (Detector time). This alignment is necessary in order to maximize the time resolution of the

full array and therefore be able to get a narrow time window in the builder and merger actors in the global level.

In order to do the detector time alignment a 35 x 35 matrix is constructed by the global time alignment with the TZero centroid of all possible combination of detectors. It is realized by the program SolveTT.py [54], which searches the best time shift, aligning the detectors at t= 500ns as it is shown in Fig. 4.3. The black histograms in the figure are the already corrected time spectra. The gaps at the diagonal of the spectra are the time alignments of the detectors with themselves.

4.1.2   The global level processing

The global level processing is the step in the data processing where the AGATA data events are built with all the capsules with energy information within the time window and after that the AGATA events are merged with the ancillary detector data. The procedure will be described in sections 4.2 and 4.3 just before discussing the tracking filter.

In the DCOD data flow system, the Event Builder actor is the one in charge of putting together all the sub-events corresponding to the different AGATA detectors. Event building is also done for the data of the light charge particle detector DIAMANT and the neutron Detector NEDA. The data stream coming out of the event builder is formatted in ADF (AGATA Data Format) and stored in different files for each detector. The Event Merger actor is in charge of assembling the AGATA and complementary instrumentation data to produce the complete event that contains all the information. The Event Merger actor uses the timestamp information from the different detector information when inside the pre-selected time window. Differently from the Event building, also based on timestamp information, the Event Merger could use time windows shifted a pre-determined offset, that is caused by the nature of the detection system and instrumentation associated to the complementary detectors. The time window for the events build of AGATA was determined to be 200 ns and for the building of NEDA-NW and DIAMANT and the merger actor 300 ns.
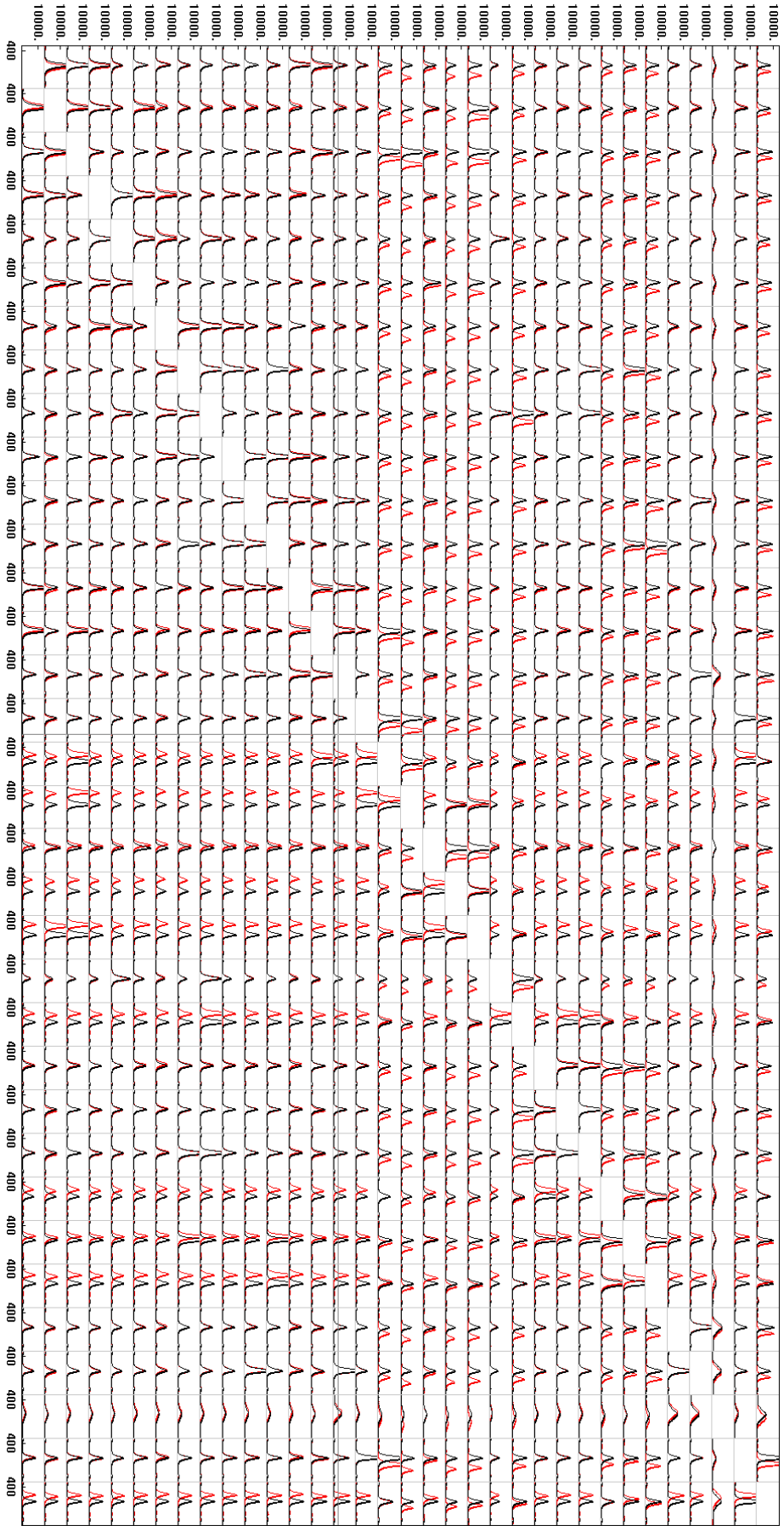
FIGURE 4.3: Global time alignment in the γ spectra, counts vs energy, with the red line representing data before the correction and the black line as the data after the GTA correction.

4.1.2.1 Tracking filter

The tracking filter is the actor that reconstructs the sequence of interactions corresponding to the detection of a γ-ray inside AGATA. In general the most common interaction in the range of energies of interest is the Compton Scattering. The Tracking procedure requires the data energy calibrated and the PSA optimized properly.

The OFT algorithm [31] was used in this experiment. The OFT parameters have been optimized to achieve the best relation between the efficiency and the peak-to-total ratio. In a first step, the forward tracking algorithm groups together the interaction points in clusters for the same interaction method depending on their relative angular distance using the optimal three empirical parameters.

The four parameters of the OFT algorithm are σ_θ, P_{track}, P_{sing} and the cluster reduction factor. The first one is the effective position resolution of the interaction points, the second one is the acceptance level of multiple-interaction clusters, the third one is the minimum probability to accept single interaction clusters as it was explained in the section 2.3.4 and the last one is the clustering reduction factor which divides by two the cluster and it makes the processing time shorter.

The optimization of these empirical parameters was done with the aim of improving the peak to background ratio and the efficiency. The OFT algorithm was applied directly to the beam data with three peaks of reference at different core energies, 384, 511 and 1256 keV as it can be seen in Fig. 4.4. These best spectra were achieved optimazing the empirical parameters to: $\sigma_\theta = 0.95$, $P_{track} = 0.03$, $P_{sing} = 0$ and cluster reduction factor 2.

4.2 NEDA and Neutron Wall data processing

In this chapter the off-line data analyisis of NEDA and NW detectors is described. As mentioned in Chapter 3 NEDA and Neutron Wall use the Charge Comparison algorithm and the ToF to discriminate between neutrons and γ-rays. Both parameter determinations were improved in the off-line analysis comparing with the ones performed at the trigger level, in the Virtex6 FPGA from the font-end electronics, as well as the calculated on-line in the NEDA acquisition servers. Charge
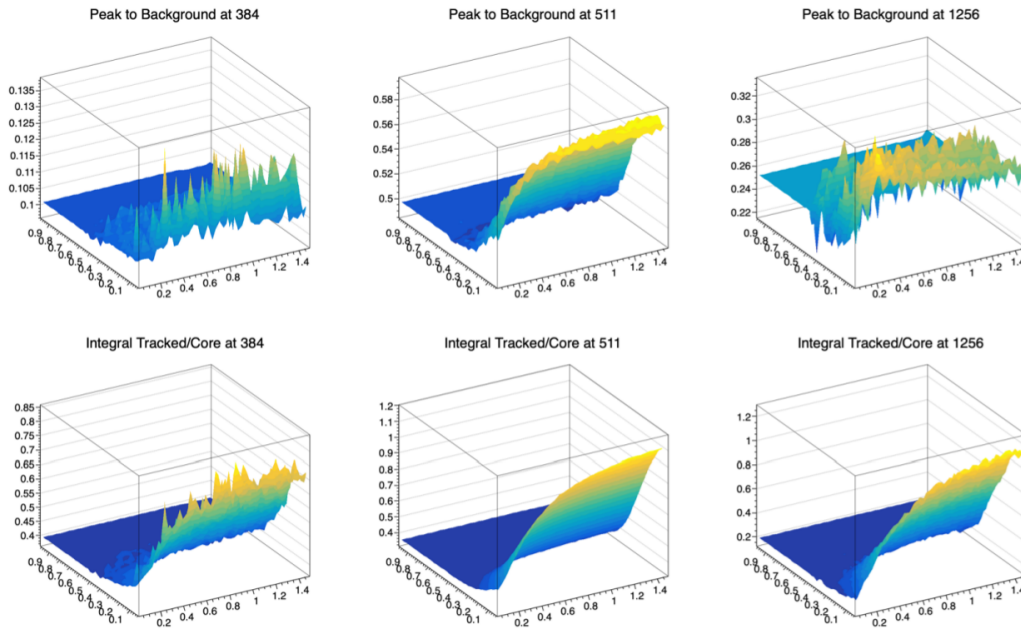
FIGURE 4.4: Spectrum at 3 different energies for the best OFT tracking parameters used in the algorithm. The relation between the peak to background and the integral tracked to core at the different energies are shown.

Comparison and the Time of Flight determinations were improved compared to those realized at the trigger level in the Virtex6 FPGA.

4.2.1 Time of Flight determination using a Digital Constant Fraction Discriminator (DCFD)

As mentioned before, one of the two quantities that allows us to discriminate between neutrons and prompt gammas is the Time of Flight (ToF). The determination of the ToF requires a DCFD analysis of the detector signal in order to obtain the best time reference. The DCFD result provides the start for the TDC (Time to Digital Converter) that provides the ToF.

The ToF determination is shown in Fig. 4.5 using the neutron detector DCFD as a start signal and the delayed accelerator radio-frequency (that is synchronized with the accelerated ion bunches) as stop.
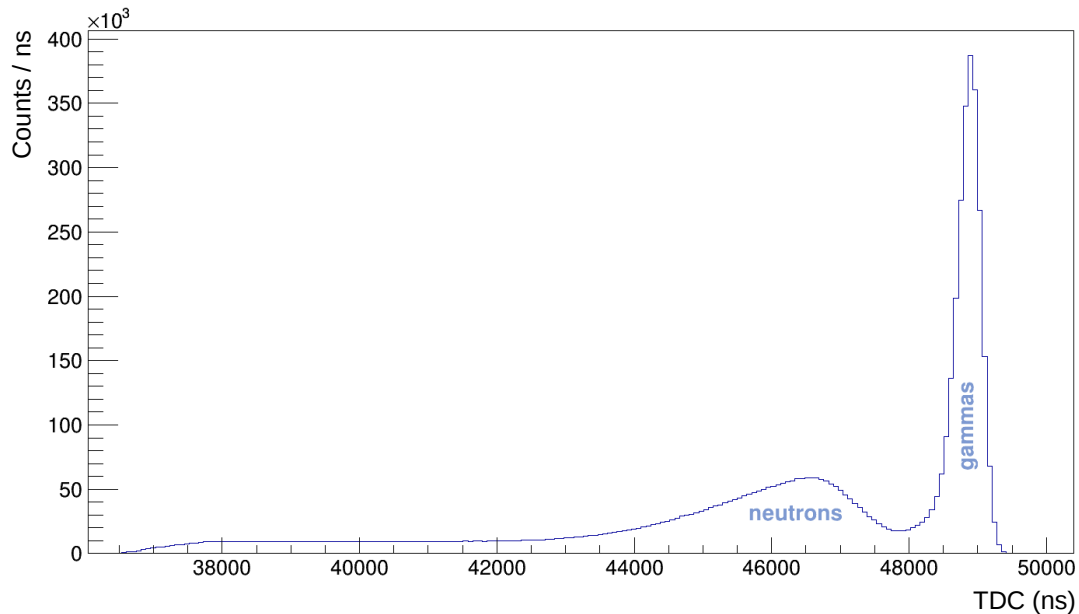
FIGURE 4.5: Result of the ToF in the detector 14 of NEDA.

4.2.2 Pulse shape analysis

As it is explained in the section 2.4.3, the NEDA digital electronics is based on NUMEXO2 cards. The FPGA's in the NEDA NUMEXO2 board incorporates the Pulse Shape Analysis (necessary to provide the neutron detection trigger) as well as the DCFD and TDC that provides the timing and ToF. Both the NUMEXO2 and the off-line processing use the PSA developed to discriminate between neutrons and γ-rays.

Two algorithms were implemented for the PSA, the Charge Comparison (CC) and the Integrated Rise Time (IRT) [45], but the first one was selected since it had better results.

The CC algorithm is realized by performing two intregrations in the digitized pulse. One integration is short and the second long. The discrimination is achieved by evaluating the ratio of the two components, since the relative intensity of these two components depends on the nature of the detected particle. In order to achieve the best FoM, the parameters of the CC algorithm, i.e. the start time of the integration, the short and long integration intervals, were optimized. Fig. 4.6 shows the results of the CC algorithm where the location of gammas (left peak) and the neutrons (right peak) are well separated. As it can be seen in Fig. 4.7, a good neutron-γ discrimination is obtained with the ratio between the long integration

over the total charge, i.e. the sum of the short plus long integrations, in the vertical axis and the total amplitude (light) collected in the detector in the horizontal axis.
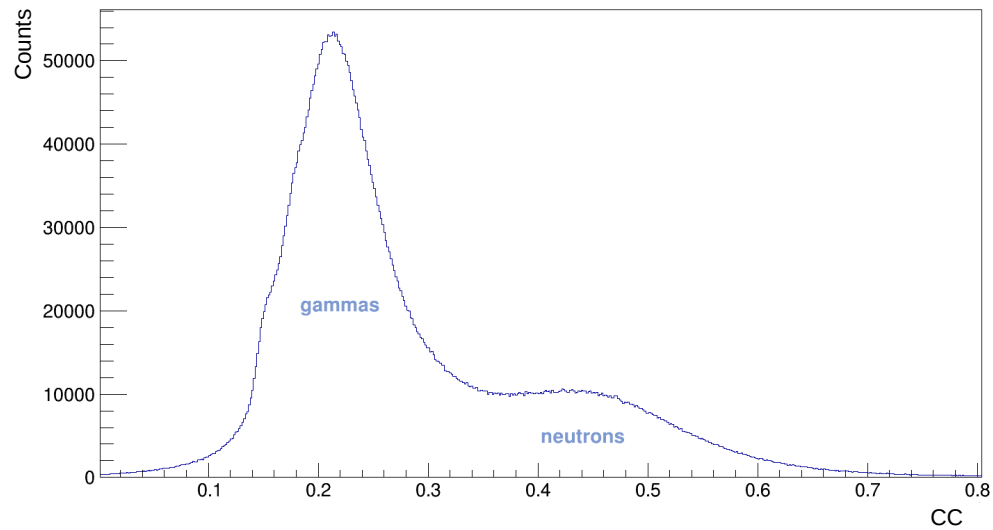
FIGURE 4.6: Digital Charge Comparison between neutrons and gammas in the detector 14 of NEDA.
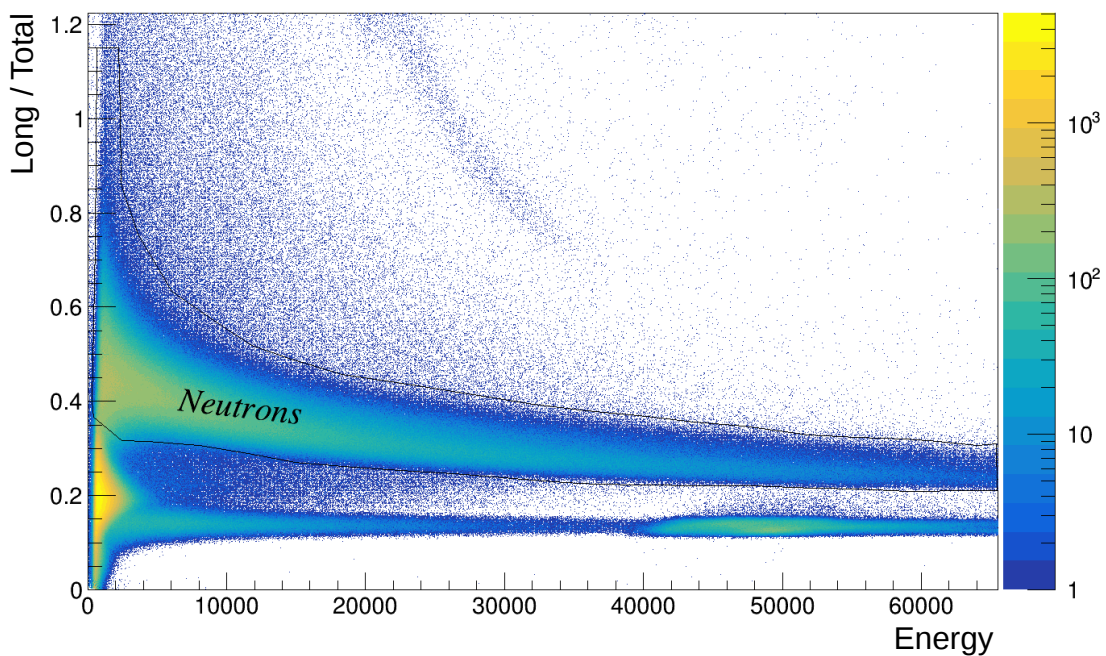
FIGURE 4.7: Neutron-γ discrimination using the total Energy of a NEDA detector. The 2D condition use to select neutrons is plotted in the figure.

In order to be more selective and to clean further the γ spectrum, i.e. to achieve a better identification of the neutrons and the gammas the Time of Flight vs PSA

information can be used as it is shown in Fig. 4.8. In this figure it can be seen the gates done for the selection of the neutrons.
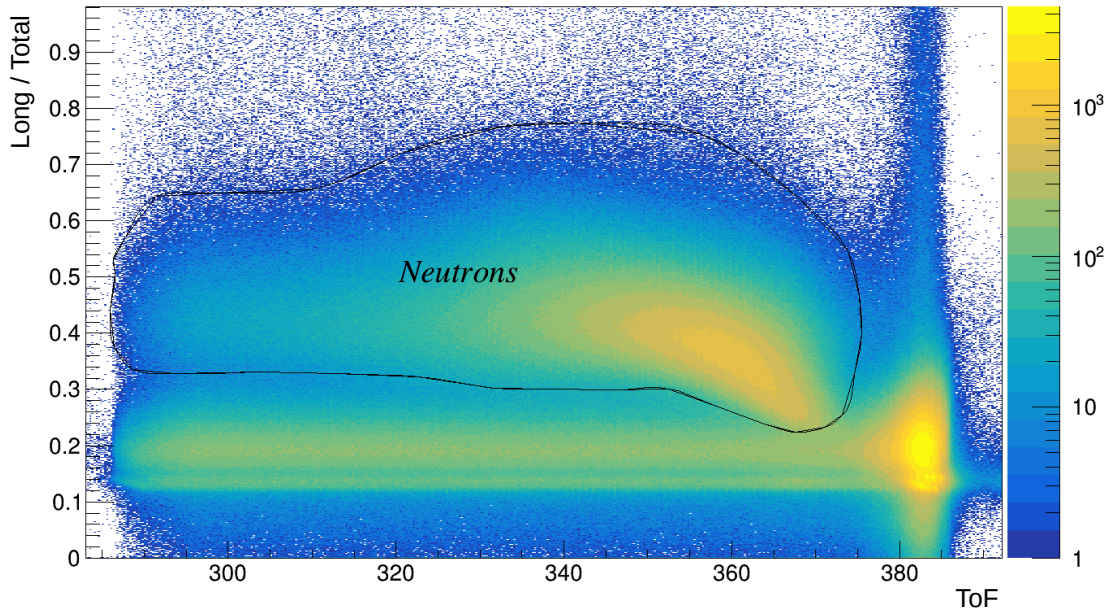
FIGURE 4.8: Neutron-γ discrimination using the Time of Flight of a NEDA detector. The 2D condition use to select neutrons is plotted in the figure.

The neutron 2D condition displayed in Fig. 4.8 corresponds to the one used for the identification of the neutrons in the corresponding detector.

4.2.3 Neutron scattering

The time determined with the DCFD discussed in section 1.3.1 is also used to determine if a multiple neutron event in the NEDA detectors corresponds to a single neutron scattered or is a real multiple neutron event. When two or more detectors have signals from a single neutron scattered, we call it a neutron cross-talk event. Since the detected neutron multiplicity is used to discriminate between reaction channels, is an important parameter to reduce the neutron crosstalk as much as possible in neutron detectors.

The ToF difference is used to determine the DCFD differences that allow to distinguish between the real and scattered multiple neutron event.

The method employed to determine the real neutron multiplicity is explained in [39] using the detector centroids (Δr) and the TOF (Δt) difference of two fired

detectors in the neutron array. A scheme of the situation is represented in Fig.
4.9. The method evaluates each pair of coincident neutron signals and if the Δt is
large enough to cover the distance Δr, the two signals come from neutron cross-
talk and a single neutron is detected. If not, they are a real two neutron event.
In each event, this method is used in all the combinations when two detectors are
fired.
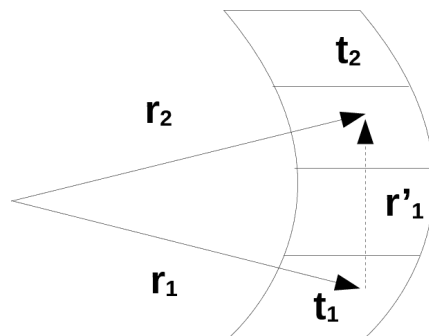
FIGURE 4.9: Neutron Wall scheme represented to show two neutron events
which times are assigned as t_1 and t_2 and s scattered event t'_1.

In Fig. 4.10 it can be observed the neutron scattering using the method described
above, comparing the distance between two firing detectors and the difference of
neutron ToF between them.
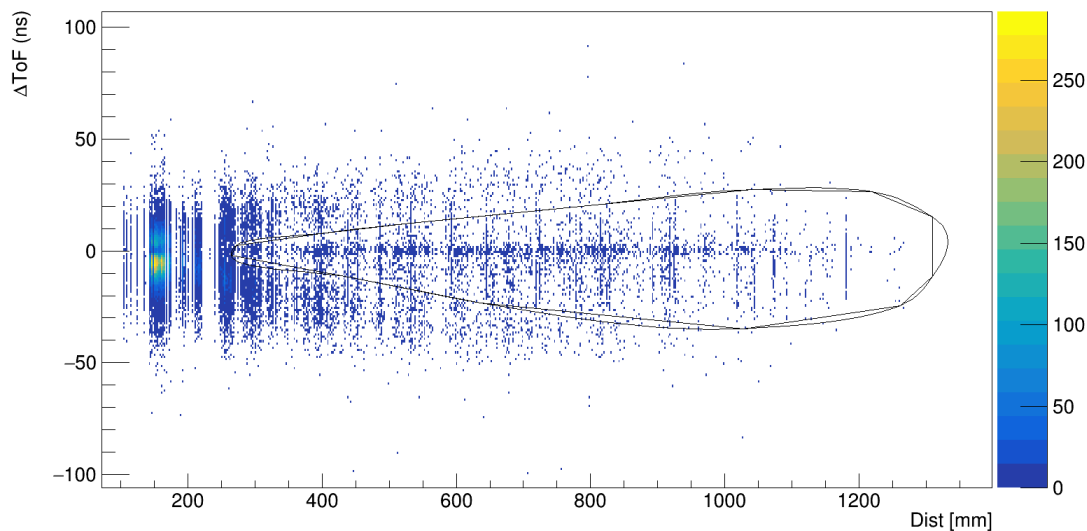
FIGURE 4.10: Plot showing the distance and Time of Flight difference between
two NEDA detectors for the events that correspond to a multiple neutron de-
tection.

4.2.4   Time alignment

NEDA and NW detectors were time aligned, shown in Fig. 4.11. The alignment is also required to do properly the merging with the AGATA data.
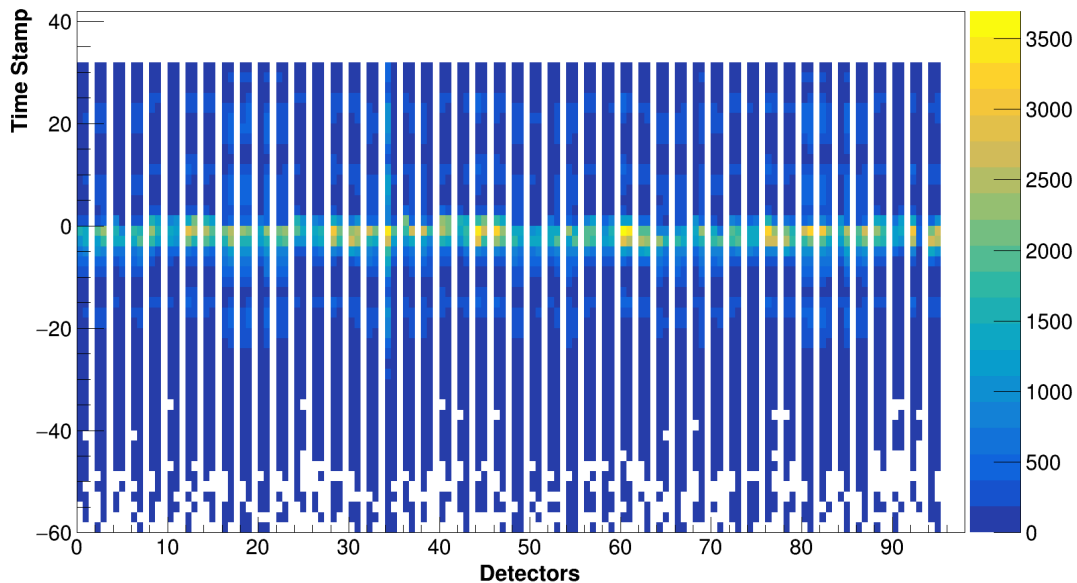
FIGURE 4.11: Time alignment of NEDA detectors.

4.3   DIAMANT data processing

4.3.1   DIAMANT particle identification

The selection of the light charged particles with DIAMANT detector is also important to improve the selection of the γ spectrum owing to the low cross section of the reaction channel of interest. The particle identification in DIAMANT is done also with Pulse Shape Analysis for the selection, 2D conditions on the Energy vs. Particle identification parameter (from PSA), are used. The signal processing is done on the sampled signal inside the NUMEXO2 FPGA, that provides three output parameters: time, particle-type and energy.

In Fig. 4.12 is shown an example of the 2D conditions used to identify the different detected particles or group of them (e.g. two protons detected).
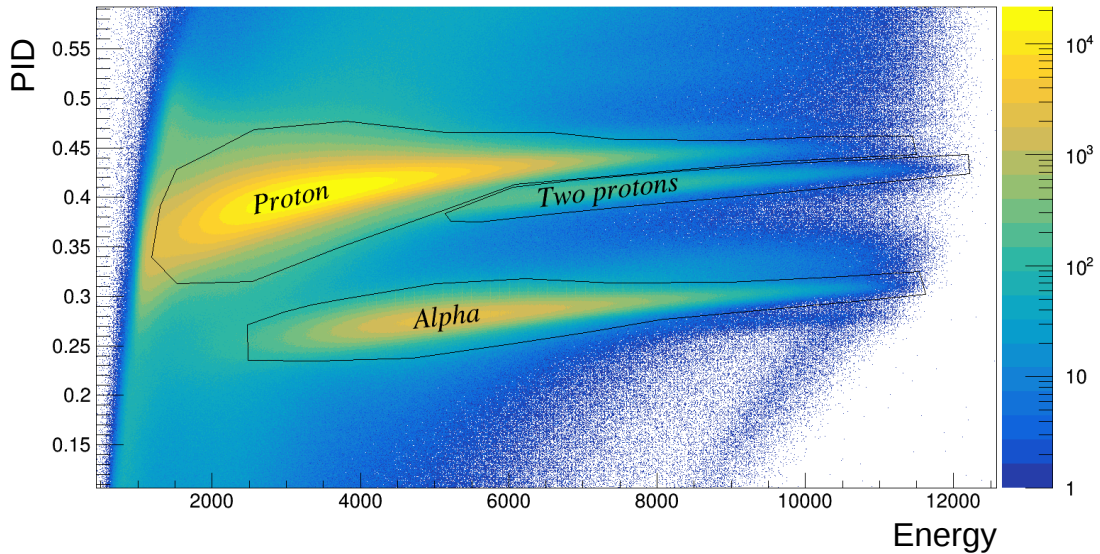
FIGURE 4.12: Particle identification in DIAMANT detector.

The NUMEXO2 DIAMANT firmware determines the energy deposited by the particle using the flat top of a pole-zero compensated trapezoidal shaper. The decay of the DIAMANT pre-amplifiers is large and the shaper uses a peaking time of the order of 10 microseconds. For the particle identification, a second trapezoidal shaper with a peaking time shorter, of the order of 1.25 microseconds has to be processed. The particle identifier is determined using the ratio between the value of the shorter trapezoidal shape flat top and the value of the longer trapezoidal flat top. Note that for the longer trapezoidal shaper flat top value, the energy (as define above) is used. For the trigger and time a digital constant fraction discriminator module is used in the FPGA.

4.3.2 Time alignment

To conclude, in the same way as with NEDA and NW detectors, DIAMANT detectors were time aligned as it can be seen in Fig. 4.11.

4.4 Plunger RDDS data processing

The method for the measurement of the lifetimes using the Recoil Distance Doppler Shift Method (RDDS) [56] employing a plunger device is described in this section.
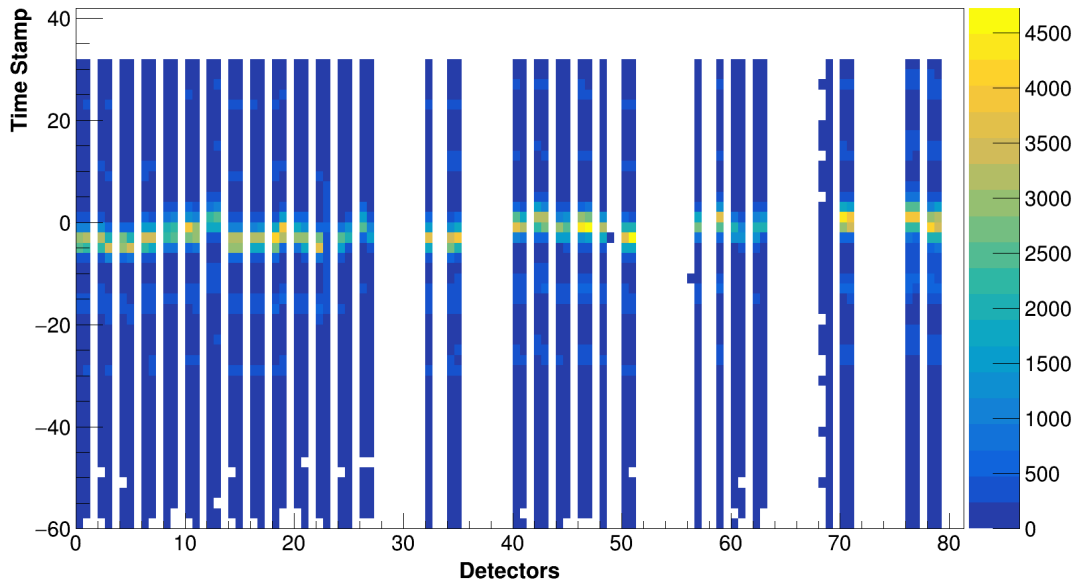
FIGURE 4.13: Time alignment of DIAMANT detectors.

The plunger device as well as the selection of target and degrader combination is described in Chapter 3.

The application of the aforementioned method is because in the experiment we expect lifetimes states ranging from 10^{-12} to 10^{-9} s. For the analysis of the plunger (RDDS) data two methods were used in the RDDS data analysis, the Decay Curve Method (DCM) and the Differential Decay Curve Method (DDCM). To validate both methods the known 9^- state lifetime of ^{112}I was used. The energy resolution of Ge detectors, like AGATA, allows to observe two separate γ-rays components of the transition in the energy spectrum. One peak corresponds to γ rays emitted in flight before the degrader and other peak corresponds to γ rays emitted after the degrader, once the nuclei have slowed down, as it is shown in Fig. 4.14.

The experiment has been performed with a plunger composed of target and degrader instead of a stopper, i.e. in differential mode, in order to improve the resolution of both components and minimizing the tails consequence of the stopping process. γ peaks of this experiment has been improved working with a plunger composed of a target and a degrader instead of a stopper, as discussed in subsection 2.6.1.

It is possible to determine the lifetime analyzing the development of the intensity ratio of shifted and unshifted components (before and afted the degrader) as a

function of the distance between the target and the degrader via the DCM and the DDCM methods as it will be explained in the following subsections.

As described in Reference [56], the RDDS technique measures the intensity of the components of the γ-ray transition, that follows the decay curve, (see equation 4.1 for the unshifted component), as a function of the plunger distance.

$$R(t) = \frac{I_u(t)}{I_s(t) + I_u(t)} \tag{4.1}$$

Where I_u and I_s are the unshifted and shifted intensities of the peaks, that correspond to the emission after and before the degrader, respectively. The components are named unshifted and shifted because the Doppler correction for the full energy spectrum is done with the velocity of the ions after the degrader and, therefore, resulting in an shifted energy for the γ-rays emitted before the degrader. $R(t)$ is the ratio between the γ rays emitted after the degrader and the total γ rays and depends on the time of flight with the velocity before the degrader and the distance between the target and degrader foils. While this distance increases, the $R(t)$ ratio is expected to decrease. The consequent decay curve can be fitted using the Bateman equations [56] with the methods explained in the following subsections.

The distance between the foils is well defined by the plunger and the decay of the nuclei takes place after and before the degrader. The energy of the γ rays emitted in flight in both cases will be Doppler shifted as it is shown in the equation 4.2 with a detector placed at an angle θ with respect to the beam axis.

$$E_\gamma = E_{\gamma 0} \frac{\sqrt{1 - \beta^2}}{1 - \beta \cos \theta} \tag{4.2}$$

being E_γ and $E_{\gamma 0}$ the measured and the real energy of the γ-ray transition respectively, $\beta = v/c$ the recoil velocity and θ the angle between the direction of the recoil and the γ ray. To be precise, $E_{\gamma 0}$ is the energy of the emitted γ ray depopulating the level of interest after the degrader in the rest reference frame.

The Doppler correction of the emitted γ rays is presented in Fig. 4.15 as a function of the angle. The velocity is determined from the optimization of the Doppler correction for the 552 keV peak, corresponding to the $9^- \to 7^-$ transition of ^{112}I. Before the Doppler correction in (a), the energy depends on the angle and after
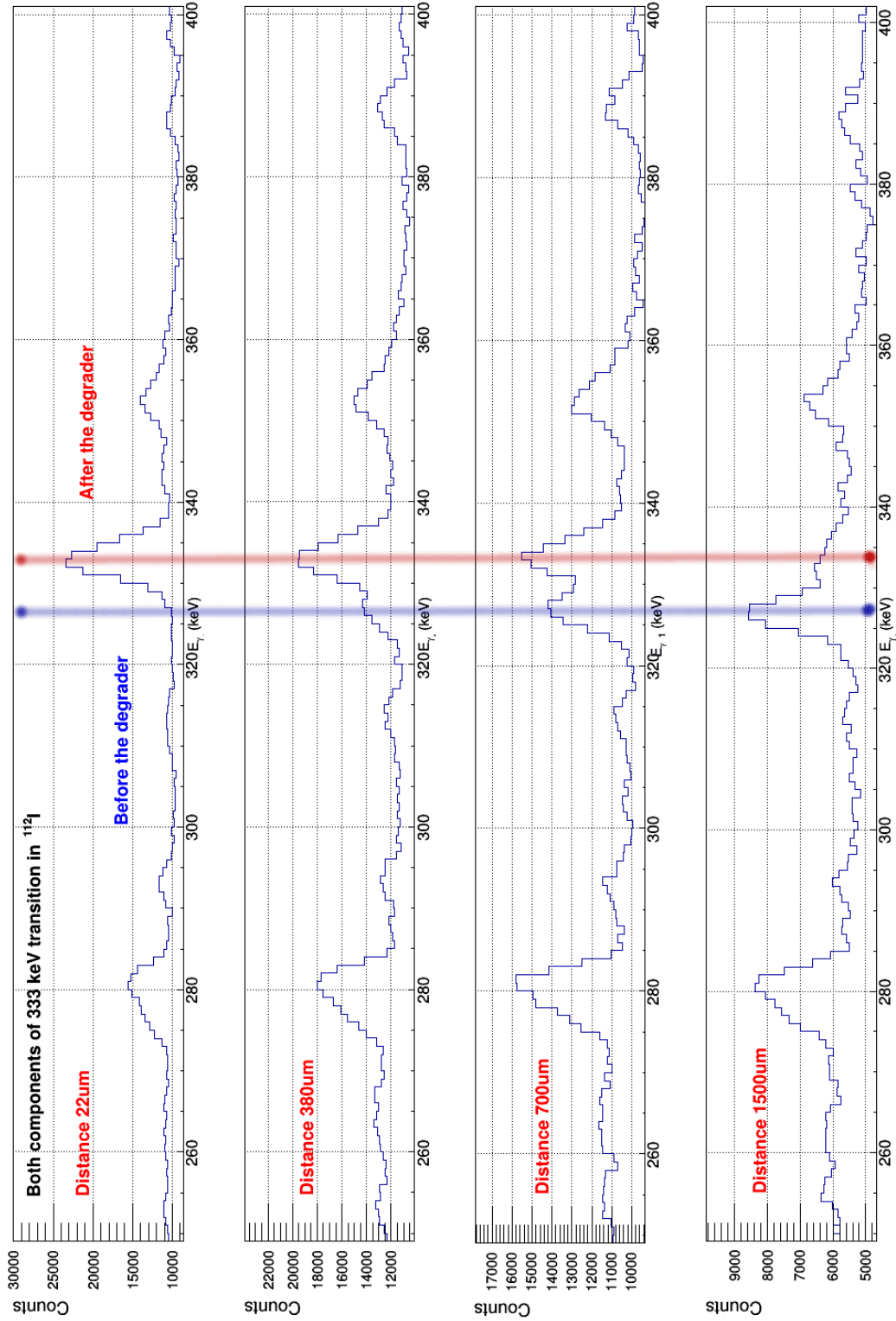
FIGURE 4.14: The two components in the γ-ray spectrum due to the different velocities, before and after the degrader, respectively from low to higher energy for different distances of the plunger.

the correction in (b) this dependence affects the width in the case of the shifted component. The optimum β obtained was 0.038 and 0.013 before and after the degrader respectively.

(a)

(b)
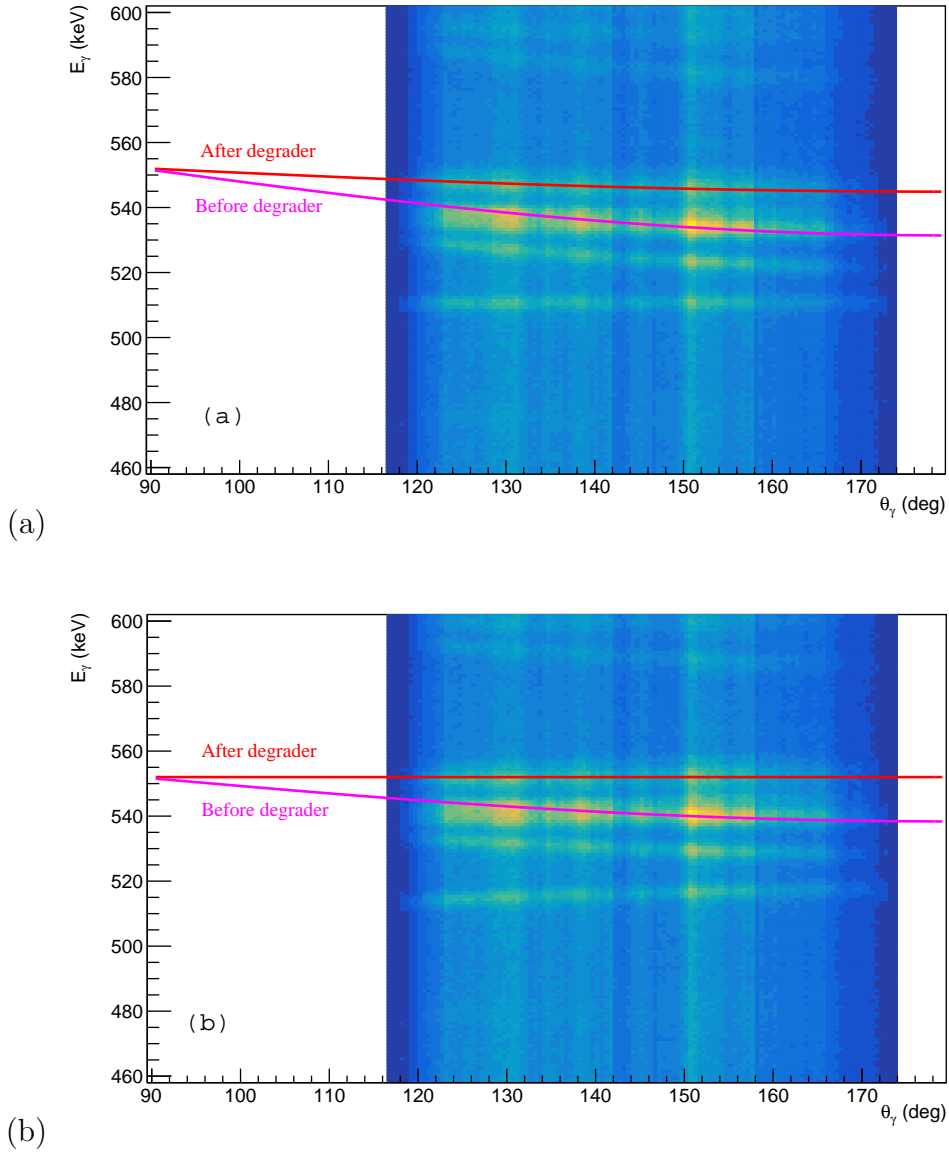
FIGURE 4.15: The γ-ray senergy as a function of the angle before (a) and after (b) the Doppler correction. The velocity is indicated as the red and purple line before and after the degrader respectively.

4.4.1   Decay curve method

The aforementioned equation 4.1 is the ratio of the intensities, needed to fit the decay curve. For only one excited level, the decay curve is the following equation

4.3 [56],

$$R(t) = n(0)e^{-\frac{t}{\tau}}, \tag{4.3}$$

where $n(0)$ is the initial population of the level and τ is the lifetime of the level.

Normally more levels are involved populating the nuclear states of interest and the level-feeding pattern becomes more elaborated like the one presented in Fig. 4.16 and the lifetime determination is through solving the system of Bateman differential equations.
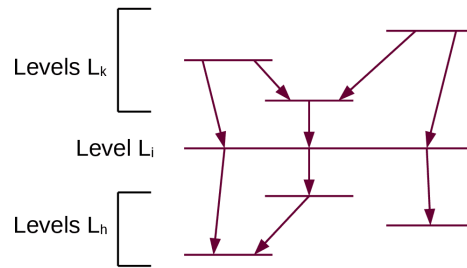
FIGURE 4.16: Schematic energy level spectrum with the level i as the interested one, populated by the levels k and deexcites via γ-rays transitions to the levels h [56].

Therefore, taking into account the level scheme above with the labels of the levels shown in Fig. 4.16, the differential equation for the level of interest i is [56]:

$$\frac{d}{dt}n_i(t) = -\lambda_i n_i(t) + \sum_{k=i+1}^{N} \lambda_k n_k(t) b_{ki}, \tag{4.4}$$

where $n_i(t)$ and $n_k(t)$ are the number of nuclei in levels i and k at time t, N is the highest feeding level number and b_{ki} are the branching ratios from levels k to levels i. λ is the decay constant of the level indicated, correlated with the level lifetime τ and the half-life $t_{1/2}$ though the equation 4.5.

$$\lambda_i = \frac{1}{\tau_i} = \frac{ln2}{t_{1/2}} \tag{4.5}$$

The solution of the differential equation with respect to the decay curve is the equation 4.6:

$$R_i(t) = P_i e^{-t\lambda_i} + \sum_{k=i+1}^{N} M_{ki}[\frac{\lambda_i}{\lambda_k}e^{-t\lambda_k} - e^{-t\lambda_i}] \tag{4.6}$$

$$\text{being} \quad M_{ki}\frac{\lambda_i}{\lambda_k - 1} = b_{ki}P_k - b_{ki}\sum_{m=k+1}^{N} M_{mk} + \sum_{m=i+1}^{k-1} M_{km}b_{mi}\frac{\lambda_m}{\lambda_k} \tag{4.7}$$

where P_i and P_k indicate the direct feeding intensity of the i and k levels.

With the aim of determine the lifetime of the excited state of interest, this function $R_i(t)$ is fitted to the experimental data. Large numbers of free parameters are involved in the fit. For this reason and the fact that all the feeding states might not be known, the fit of the data is a complex task. In the following subsection another method that gives better uncertainties in the lifetime determination, the Differential Decay Curve Method (DDCM), will be explained.

4.4.2   Differential decay curve method

4.4.2.1   Singles analysis

The DDCM [56] is an alternative method that eludes problems of the standard analysis like the uncertainties in the absolute position of the degrader with respect to the target.

The DDCM is a method for the lifetimes determination of excited nuclear levels when all feeders are known, using the derivative of the intensity of the unshifted component of a depopulating transition as a function of the target to degrader distance.

Initially from the result of integration the Bateman differential equations described in 4.6;[56]:

$$-n_i(t) = -N_i(t) + \sum_{k=i+1}^{N} b_{ki}N_k(t) \tag{4.8}$$

Using the derivative of the decay function $N_i(t)$ the equation for the lifetime of the level is:

$$\tau_i(t) = \frac{1}{\lambda_i} = \frac{-N_i(t) + \sum_{k=i+1}^{N} b_{ki} N_k(t)}{\frac{d}{dt} N_i(t)} \qquad (4.9)$$

The decay curves $R_i(t)$ are directly proportional with the functions $N_i(t)$ $N_k(t)$ as $R_i(t) = N_i(t)/\alpha$ and $R_k(t)$, therefore it can be gained the equation 4.10.

$$\tau_i(t) = \frac{1}{\lambda_i} = \frac{-R_i(t) + \sum_{k=i+1}^{N} b_{ki} \alpha_{ki} R_k(t)}{\frac{d}{dt} R_i(t)}, \qquad (4.10)$$

being

$$\alpha_{ki}(t) = \frac{w_k(\Theta) \cdot \epsilon(E_\gamma k)}{w_i(\Theta) \cdot \epsilon(E_\gamma i)} \qquad (4.11)$$

the factor of proportionality determined via the detector efficiencies $\epsilon(E_\gamma k)$ and $\epsilon(E_\gamma i)$ and the angular distributions $w_k(\Theta)$ and $w_i(\Theta)$ of the γ-radiation.

The equation 4.10 determines an independent lifetime for each value of the flight time t. This result should be constant due to the fact that the level lifetime is a constant and the deviations denote the presence of a systematic error. This method has some advantages in comparison with some type of systematic errors can be identified.

4.4.2.2 Coincidence analysis

One of the known issues in lifetime measurements with the present technique is associated with the indirect feeding. In fusion-evaporation reactions, the feeding to low lying states could happen through unobserved transitions that de-excite unknown states with unknown lifetimes. The effect of the feeders in the lifetime measurement can be avoided by using γ-γ coincidences and setting the coincidence condition in a transition above the state of interest.

There are two ways to use the γ-coincidence in the lifetime analysis, by gating on a depopulating transition of the level of interest or by gating in a feeding transition. The first method is used to clean the spectra but the feeding pattern does not change. The second method allows to limit the population to the experimentally observed feeding. In this section the coincidence analysis is explained for the
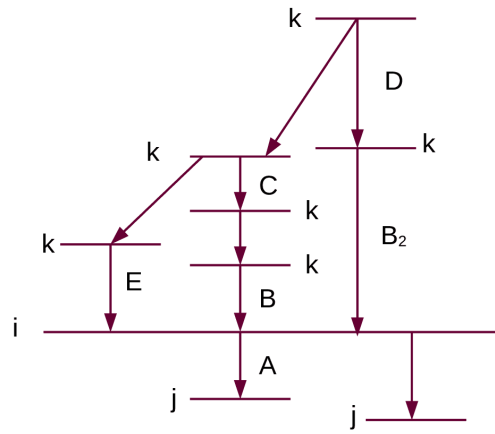
FIGURE 4.17: Level decay scheme. Figure adopted from [56].

case where the coincidence condition selects only one cascade, for instance the path (C,A) or (E,A) in Fig. 4.17. The equation which describes it would be the equation 4.12 [56].

$$\frac{d}{dt}n_i^{CA}(t) = -\lambda_i n_i^{CA}(t) + \lambda_k n_k^{CA}(t) \tag{4.12}$$

being $n_i^{CA}(t)$ the number of nuclei in the state i at the time t which were populated via the cascade defined by the condition (C,A) via transition B only. In this case the lifetime can be determined as the singles case described above, with the equation 4.13.

$$\tau_i = \frac{-N_i^{CA}(t) + N_k^{CA}(t)}{\frac{d}{dt}N_i^{CA}(t)} \tag{4.13}$$

being $N_i^{CA}(t) = \lambda_i \int_t^\infty n_i^{CA}(t)\mathrm{d}t$ the numbers of decays of i in the time interval $[t, \infty]$. It is necessary to use the observational coincidence intensities, taking into account the efficiencies for detecting them and their angular correlation, obtaining the equation 4.14 for the lifetime determination.

$$\tau_i = \frac{-\{C, A_u\} + \{C, B_u\}}{\frac{d}{dt}\{C, A_u\}} \tag{4.14}$$

where are $\{C, A_u\}$ and $\{C, B_u\}$ the coincidence intensities for the unshifted component of the transition A and B respectively.

The γ-γ coincidence technique is exemplified in Fig. 4.18 [56].

It is possible to avoid the side-feeding shown in Fig. 4.18(a), limiting the feeding, to the state of interest depicted, to the one only coming from transition B, can be
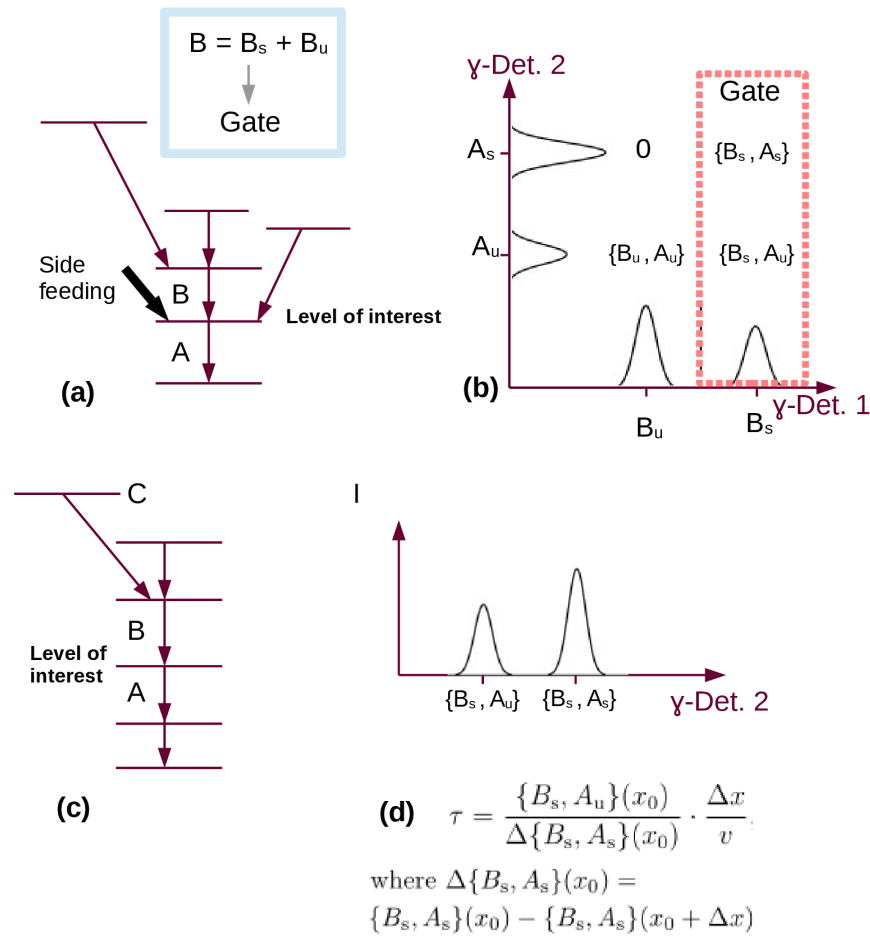
FIGURE 4.18: (a) Level scheme; (b) Gate on shifted component of B transition in the γ-γ coincidence matrix belonging to (a) at x_0 target-to-stopper separation; (c) level scheme with the selected feeding on B; (d) Lifetime calculated via gated spectrum. Figure adopted from [56].

achieved gating on the shifted component B_s, as it can be seen in Fig. 4.18(b), in the γ-γ coincidence matrix. Doing this gate, the resulting area $\{Bs, As\}(x)$, $\{Bs, Au\}(x)$ (where the first index corresponds to the coincidence transition B_s, the second to the evaluated area A_s or A_u and x is the variable distance target degrader) illustrated in Fig. 4.18(d) determine the lifetime according the shown formula which is derived in the framework of the Differential Decay-Curve Method (DDCM) explained below.

The coincidence analysis must be done if possible on shifted components of feeding transitions only. The lifetime measurements does not improve gating on both components due to the fact that unshifted feeding transitions do not contain lifetime information, it would only increase the uncertainties [56].

In the case of an indirect feeding, (C_s), the lifetime is determined by the equation 4.15.

$$\tau(x) = \frac{\{C_s, A_u\}(x) - \alpha\{C_s, B_u\}(x)}{\frac{d}{dx}\{C_s, A_s\}(x)} \cdot \frac{1}{v}, \tag{4.15}$$

$$\text{being} \quad \alpha(x) = \frac{\{C_s, A_u\}(x) + \{C_s, A_s\}(x)}{\{C_s, B_u\}(x) + \{C_s, B_s\}(x)} \tag{4.16}$$

Being x the target-degrader separation and v as the mean recoil velocity of the nuclei.

Specifically for a gate on a direct feeding transition of the level of interest, i.e. a gate on the transition B in the level scheme of the Fig. 4.17, using the observational transition intensities represented as $\{A, B\}$, the lifetime can be determined by the equation 4.17.

$$\tau(x) = \frac{\{B_s, A_u\}(x)}{\frac{d}{dx}\{B_s, A_s\}(x)} \cdot \frac{1}{v} \tag{4.17}$$

This lifetime can be determined with a gate on the shifted component of the transition B (B_s), and the determination of the peak areas of the shifted, (A_s) and unshifted (A_u) components of the transition A. Therefore to determine the lifetime of the level of interest only two numbers per distance are needed. The quantities obtained for different distance have to be normalized, for example in our case we did it to the total intensity of the $2^+ \rightarrow 0^+$ transition in the projection of the coincidence matrix.

In conclusion, the lifetime determination via DDCM needs only the two equations 4.15 and 4.17 [56], for indirect or direct feeding respectively, with precise and reliable result according to the DDCM using coincidence plunger measurements.

The equations of each method were implemented in Root, partially by R. Pérez [57]. The fit method was introduced with the object-oriented implementation of the MINUIT minimization package with the options M, E and R, i.e., improving fit results by using the IMPROVE algorithm of Tminuit, performing the errors estimation using the Minos technique and using the range spectified in the function range, respectively [58].

4.4.3   Verifying the lifetime determination method: lifetime of the $7^- \rightarrow 7^-$ transition in ^{112}I.

In order to validate the experimental conditions and the lifetime determination methods chosen, a transition with well known lifetime in ^{112}I has been used.

The lifetime of this state is known to be 130(25) ps [59].

The nucleus ^{112}I is populated in our reaction as the 1 neutron and 3 protons evaporation channel. In Fig. 4.19 the Doppler corrected spectra for few distances and with the 1n3p particle condition is shown for the region of energy corresponding to the 643 keV transition.

For the lifetime analysis, in order to increase the number of counts, we have added the spectra with the 1n2p and 1n3p conditions (after checking that no contamination was added). The measured lifetime is $\tau=$ 102 (3) ps as shown in Fig. 4.20 for both, the fit of the decay curve and the differential decay curve methods, explained in this section. This result is in agreement with the previous measument, $\tau=$ 130 (25) ps [59].
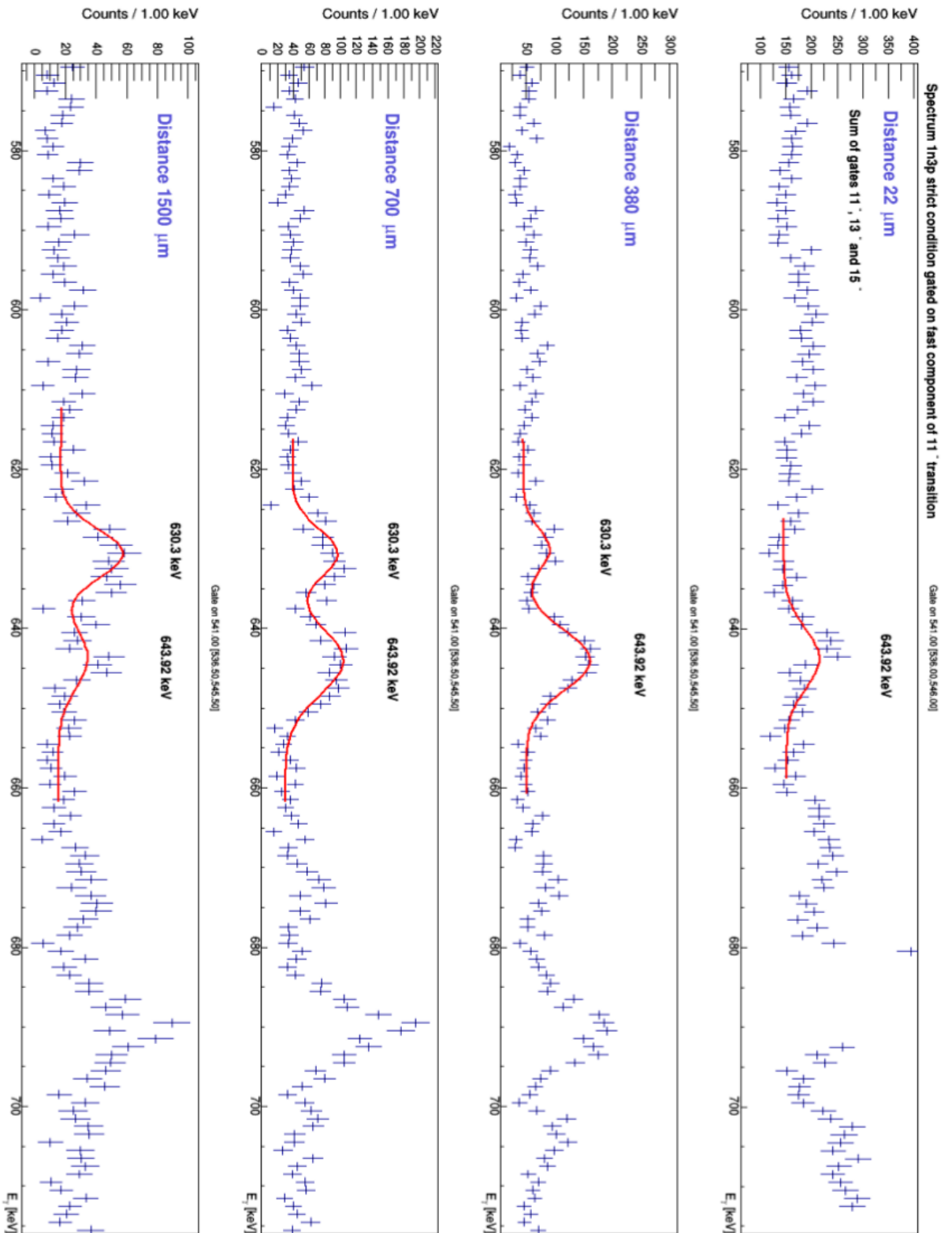
FIGURE 4.19: γ-ray spectrum dopper corrected with the 1n3p condition for the $7^- \rightarrow 7^-$ transition of ^{112}I for the different plunger distances.
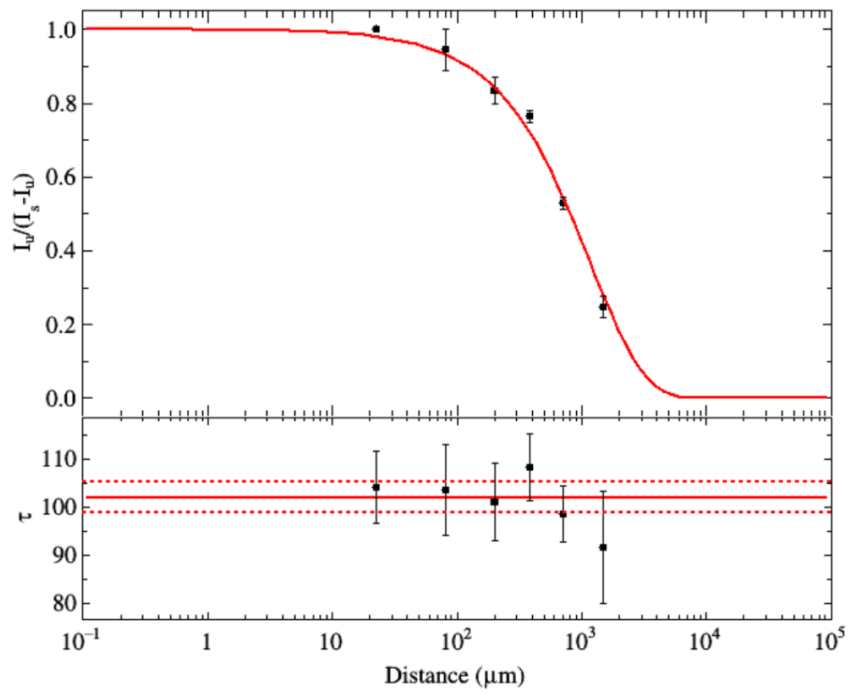
FIGURE 4.20: DCM and DDCM methods applied on the top and the bottom respectively for the lifetime determination for $7^- \rightarrow 7^-$ transition of ^{112}I. The solid and dashed red lines in the DDCM show the result and experimental uncertainty respectively.

Chapter 5

Experimental results

As I have mentioned before, this work aims at contributing to the study of the evolution of the quadrupole and octupole collectivity, in the Xe isotopes, with the lifetime determinations in low-lying states in ^{112}Xe. The level scheme with the transitions known in this nucleus is shown in Fig. 5.1 [1].
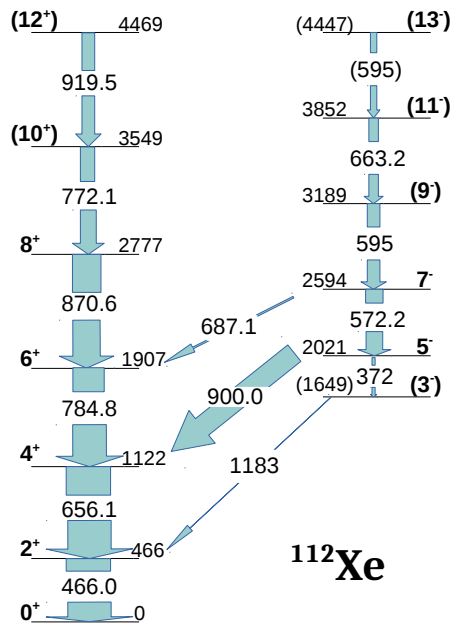
FIGURE 5.1: Level scheme of ^{112}Xe. γ-ray intensities are proportional to the widths of the arrows.

The nucleus of interest, the ^{112}Xe is difficult to populate experimentally, with production cross section of the order of hundreds of microbarn. We have to consider as well the efficiency of the complementary instruments (NEDA and DIAMANT)

used for the selection of the reaction channels. Even if the reaction leading to ^{112}Xe corresponds to the evaporation of 2 protons and 2 neutrons (2p2n), the spectra with conditions in the detection of 2 neutrons with 0, 1 and 2 protons were summed (2n2p + 2n1p + 2n0p). The one neutron particle condition spectra were excluded because the large amount of ^{112}I transitions (the 1n3p channel). ^{112}I is populated with cross-section about 2 orders of magnitude larger than our nucleus of interest and will be present in the 1 neutron condition spectra.

The projections of the symmetric γ-γ matrices, with the aforementioned 2n2p coincidence conditions, used in the data analysis, are shown in Fig. 5.2. The shifted and unshifted components of the most intense transitions in ^{112}Xe are indicated, while other undesirable transitions, mainly from ^{112}I are also visible in the projections. As it can be seen in Fig. 5.2, the spectrum corresponding to the 67 um distance has much less number of events than the rest and therefore, it was necessary to discard this distance in some cases during the analysis.
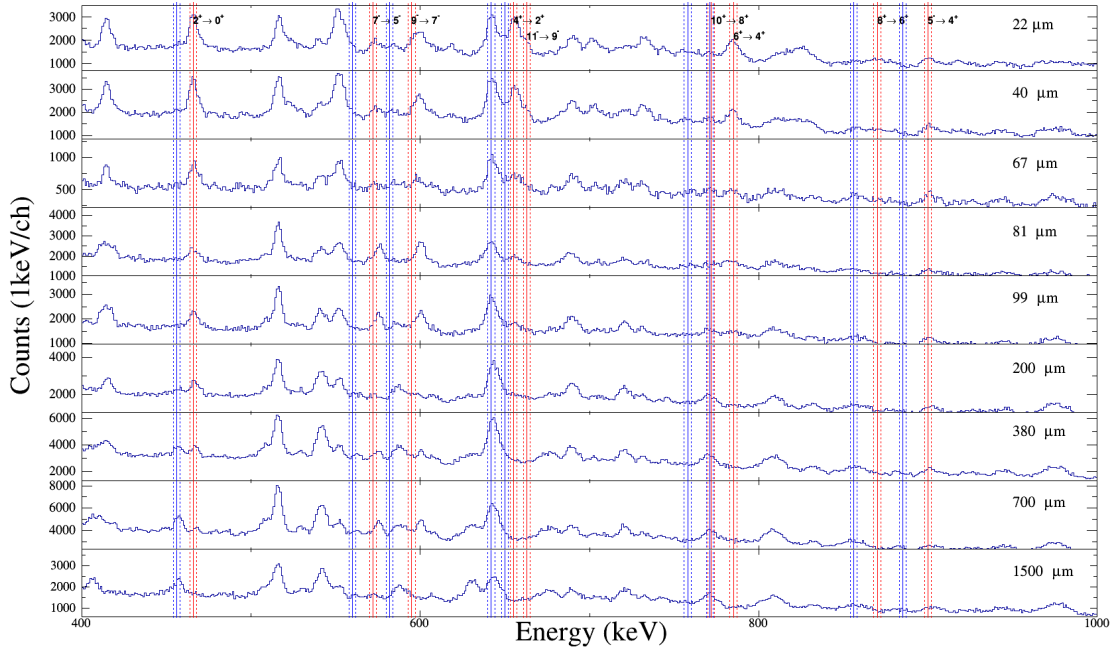
FIGURE 5.2: Main transitions of ^{112}Xe nucleus from the projection of the matrices with 2n2p condition. Shifted components are represented as red lines while the shifted components are represented as blue lines. Dashed lines indicates the FWHM of the transition peaks.

5.1 Measurements related to the quadrupole collectivity

Regarding the quadrupole collectivity, in this work we aim to determine the reduced transition probabilities of the $4^+ \to 2^+$ and $2^+ \to 0^+$ transitions via the lifetime measurements of the 4^+ and 2^+ states.

I will describe the process of the analysis starting from the 4^+. As it is show in Fig. 5.1, the 4^+ state is feed by the 785 keV transition de-exciting the yrast 6^+ state and by the 900 keV transition de-exciting the 5^- state. As it will be discuss in this chapter both feeder states have lifetimes differing about 1 order of magnitude. We will perform the lifetime analysis using the 6^+ feeder branch for the coincidence condition.

The first step in the lifetime analysis has been to check if the decay curve of the feeding $6^+ \to 4^+$ transition can be fit with a single effective lifetime, and to determine this effective lifetime.

In order to do that, we have used coincidence condition in the γ-γ matrix (described in the introduction of this chapter) including both shifted and unshifted components of the $2^+ \to 0^+$ 466 keV transition, resulting the spectra shown in Fig. 5.3. The reason to do that is that this transition is very clean regarding contaminants and it provides the best selection to determine effective lifetimes.

TABLE 5.1: Areas of the shifted and unshifted components of the 785 keV transition de-exciting the 6^+ state. The areas have been determined using the γ-γ matrix with a coincidence condition in both the shifted and unshifted components of the $2^+ \to 0^+$ 466 keV transition.

Distance (μm)	I_s (counts)	I_u (counts)
1500 (15)	34 (23)	0 (23)
700 (15)	264 (57)	16 (40)
380 (15)	250 (61)	45 (33)
200 (15)	142 (38)	5 (17)
99 (6)	104 (36)	24 (15)
81 (3)	56 (31)	11 (30)
39.7 (9)	147 (40)	110 (34)
22.4 (9)	36 (36)	181 (36)

The two methods described in section 4.5, namely the DCM and DDCM were providing values for the 6^+ effective lifetime of $\tau = 5.0$ (1.0) ps and 5.0 (8) ps
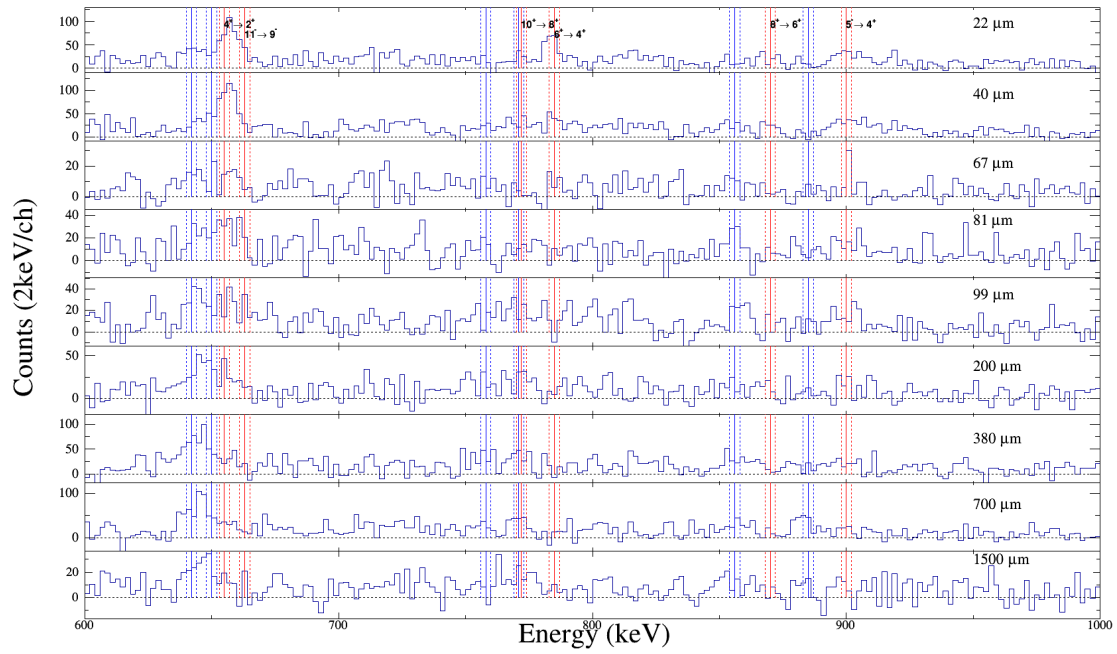
FIGURE 5.3: γ spectra with a coincidence condition in both the shifted and unshifted components of the $2^+ \rightarrow 0^+$ 466 keV transition for all measured plunger distances.
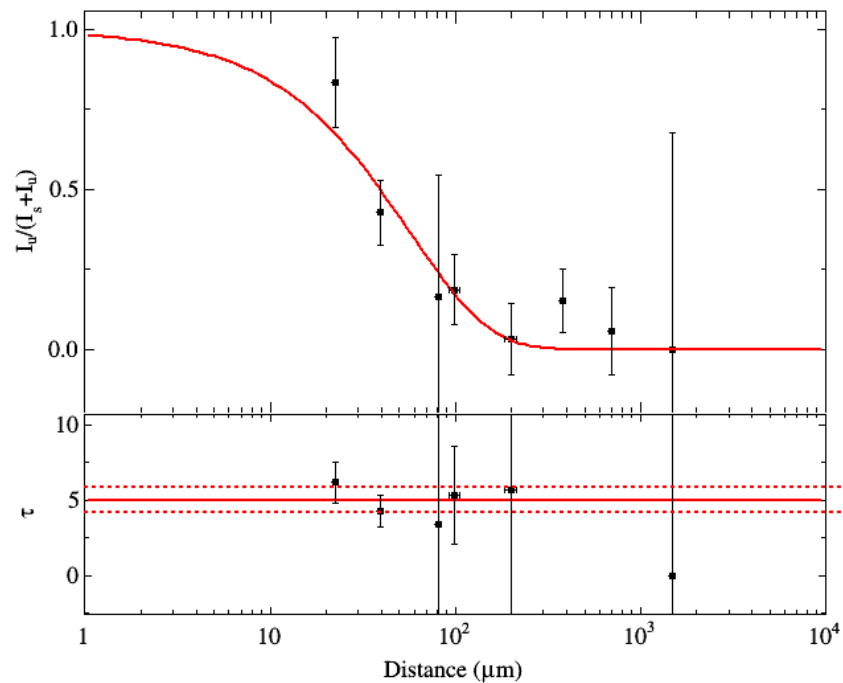
FIGURE 5.4: Effective lifetime of 6^+ state in ^{112}Xe determined with DCM (above) and DDCM in the sensitivity region (bottom). The fit is shown as a red line and the uncertainties in the DDCM method as dashed red lines.

respectively. We have adopted the DDCM result since in general is less sensitive to systematic uncertainties. The fit of the experimental ratios (Iu/Is+Iu) using the decay curve (upper panel and the results of the DDCM (lower panel) are shown in Fig. 5.4.

Once the effective lifetime of the 6^+ state is known, it is possible to proceed with the determination of the 4^+ lifetime. This requires the evaluation of the shifted and unshifted components of the $4^+ \to 2^+$ 656 keV transition. Unfortunately the shifted component of the 656 keV transition in ^{112}Xe is almost always contaminated by the unshifted component of the 643 keV $7^- \to 5^-$ transition in ^{112}I and the unshifted component is contaminated by the $11^- \to 9^-$ 663 keV transition in our nucleus of interest ^{112}Xe. Using a γ-coincidence in both components of the $6^+ \to 4^+$ transition makes negligible the contribution of the $11^- \to 7^-$ shifted component since it is only in coincidence through the $7^- \to 6^+$ E1 transition.

The intensities of this gate are represented in table 5.2 normalized to the areas of the both components of $2^+ \to 0^+$ transition, determined in the projection of the γ-γ matrix, shown in Fig. 5.5 that are listed in table 5.4. The 99 um distance was removed from the analysis.
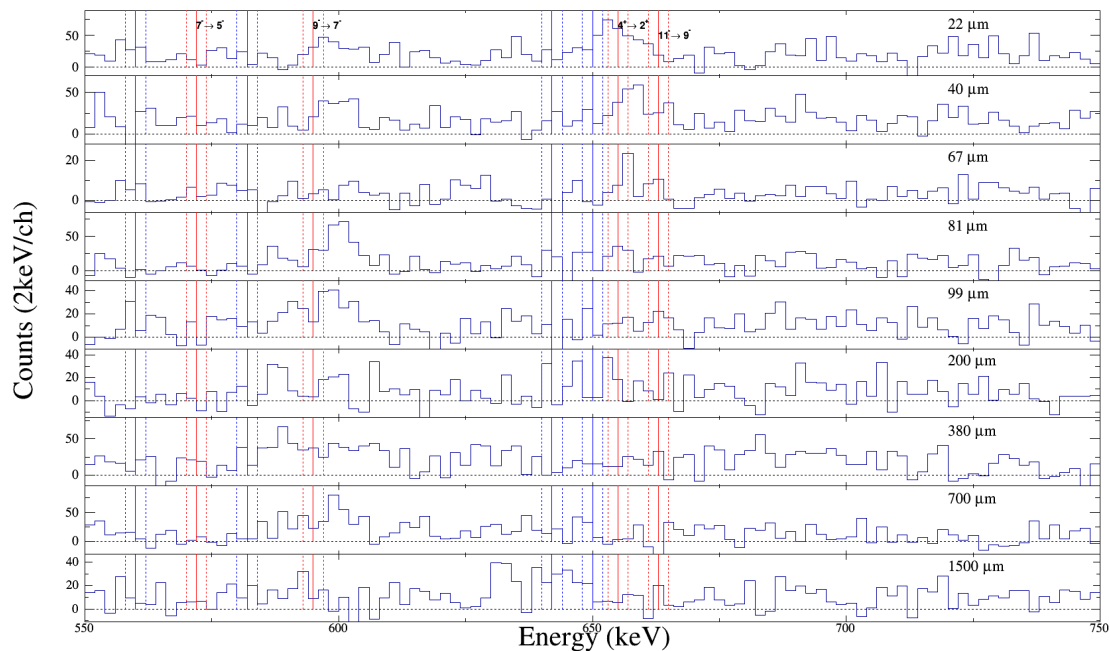
FIGURE 5.5: γ spectra with a coincidence condition in both the shifted and unshifted components of the $6^+ \to 4^+$ 785 keV transition for all measured plunger distances.

TABLE 5.2: Normalized intensities of the unshifted component of the 656 keV $4^+ \to 2^+$ transition, determined with a γ-coincidence condition in both components of the 685 keV $6^+ \to 4^+$.

Distance (μm)	I_u normalized (counts)
1500 (15)	0.07 (15)
700 (15)	0.01 (14)
380 (15)	0.24 (15)
200 (15)	0.46 (5)
81 (3)	0.71 (6)
39.7 (9)	0.83 (3)
22.4 (9)	1.00 (15)
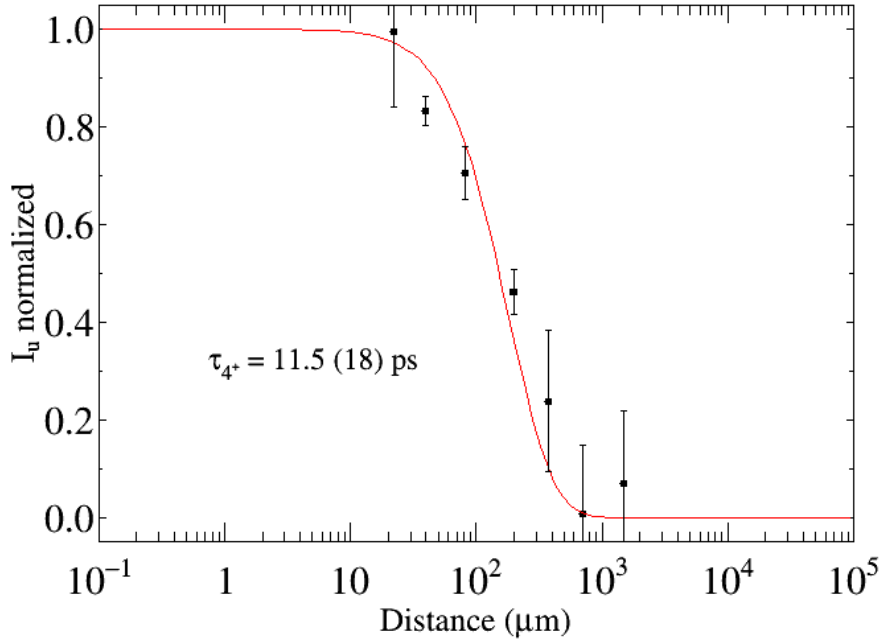
FIGURE 5.6: Determination of the 4^+ lifetime in ^{112}Xe by fitting the experimental intensities of the unshifted component of the $4^+ \to 2^+$ transition (in the spectrum with coincidence conditions in both components of the $6^+ \to 4^+$ transition) normalized to the sum of the areas of both components of the $2^+ \to 0^+$ transition. The fit has been done considering a cascade of 2 transitions $6^+ \to 4^+ \to 2^+$ and fixing the effective lifetime of the 6^+ state.

Using the above mentioned DCM, the lifetime determined for the 4^+ state is $\tau = 11.5$ (18) ps.

Once the lifetime of the 4^+ state has been determined, we can proceed with the analysis of the 2^+ lifetime.

Since both components of the $2^+ \rightarrow 0^+$ transition are clean from contaminations coming from the ^{112}I transitions, it is possible to apply the differential decay curve method gating from above. In this case we have to apply the coincidence condition in the shifted component of the $4^+ \rightarrow 2^+$ transition, generating the spectra of Fig. 5.7.

The areas of both components of the $2^+ \rightarrow 0^+$ transition determined with the aforementioned conditions are listed in table 5.3.
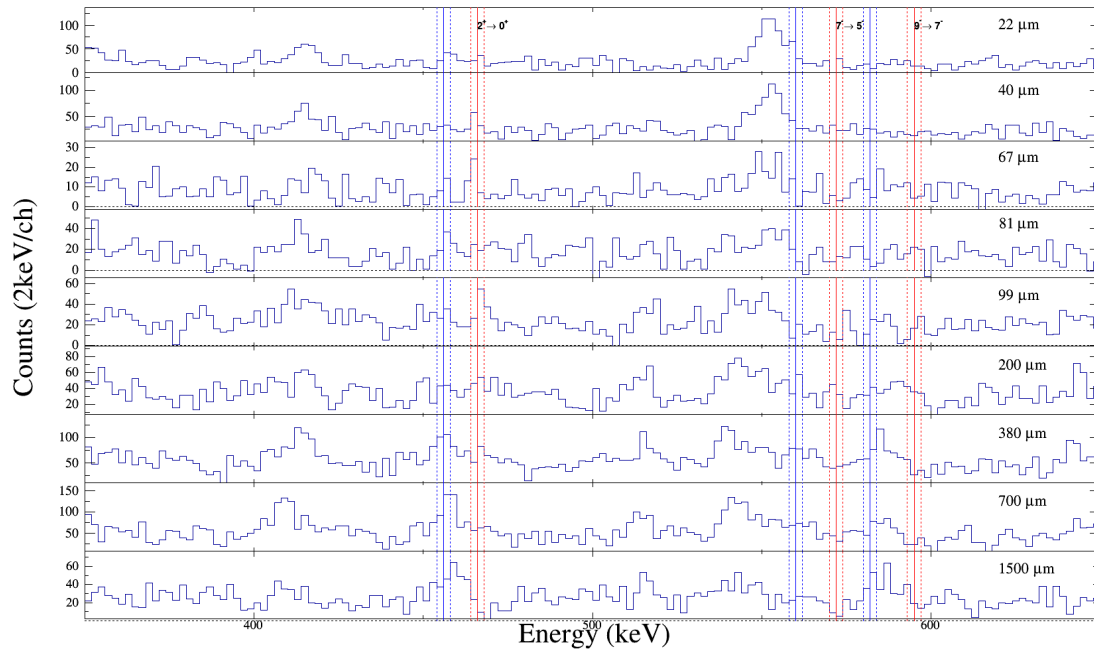
FIGURE 5.7: γ spectra with a coincidence condition in the shifted component of the $4^+ \rightarrow 2^+$ 656 keV transition for all measured plunger distances.

TABLE 5.3: Areas of both shifted and unshifted components of the $2^+ \rightarrow 0^+$ transition, determined in the spectra with coincidence condition in the shifted component of the $4^+ \rightarrow 2^+$ transition, for all the plunger distance measurements.

Distance (μm)	I_s (counts)	I_u (counts)
1500 (15)	170 (40)	4 (40)
700 (15)	442 (51)	103 (40)
380 (15)	283 (44)	171 (41)
200 (15)	105 (29)	129 (30)
99 (6)	77 (27)	106 (31)
81 (3)	82 (77)	104 (29)
67 (5)	40 (18)	44 (21)
39.7 (9)	50 (36)	110 (45)
22.4 (9)	104 (33)	51 (50)

In order to determine the lifetime is necessary to renormalize the areas listed in table 5.3 by factors that take into account the differences between the production of our nucleus of interest in the different plunger distance measurements. In our case we have use the sum of both, shifted and unshifted, components of the $2^+ \to 0^+$ transition in the projection of the γ-γ matrix dicussed at the beginning of this chapter. The normalization areas are listed in table 5.4.

TABLE 5.4: Added areas of both components of $2^+ \to 0^+$ transition in the γ-γ matrix total projection spectra for each plunger distance.

Distance (μm)	I_{s+u} (counts)
1500 (15)	8000 (700)
700 (15)	13300 (500)
380 (15)	12400 (400)
200 (15)	7900 (300)
99 (6)	7000 (300)
81 (3)	6600 (300)
67 (5)	3200 (400)
39.7 (9)	12000 (1000)
22.4 (9)	11400 (500)

Applying the Differential Decay Curve Method with gate in the shifted component of the transition above, described in section 4.4.2.2, to the normalized shifted and unshifted components of the $2^+ \to 0^+$ transition, the lifetime obtained for the 2^+ state is $\tau = 22$ (3) ps. The analysis steps are shown in Fig. 5.8. In the upper and central panels are represented the experimental points and fits of the shifted and unshifted components respectively, as a function of the plunger distance. In the lower panel is plotted the ratio of the unshifted experimental values and the derivatives of the shifted component fit for the corresponding distances.

5.1.1   Determination of the reduced transition probabilities for the $4^+ \to 2^+$ and $2^+ \to 0^+$ transitions

In the previous section, the determination of the lifetimes in the 4^+ and 2^+ yrast states in ^{112}Xe is described. This information is essential to calculate the reduced transitions probabilities. The other fundamental ingredients are the branching ratios that allow to calculate the partial lifetimes that correspond to the transitions.
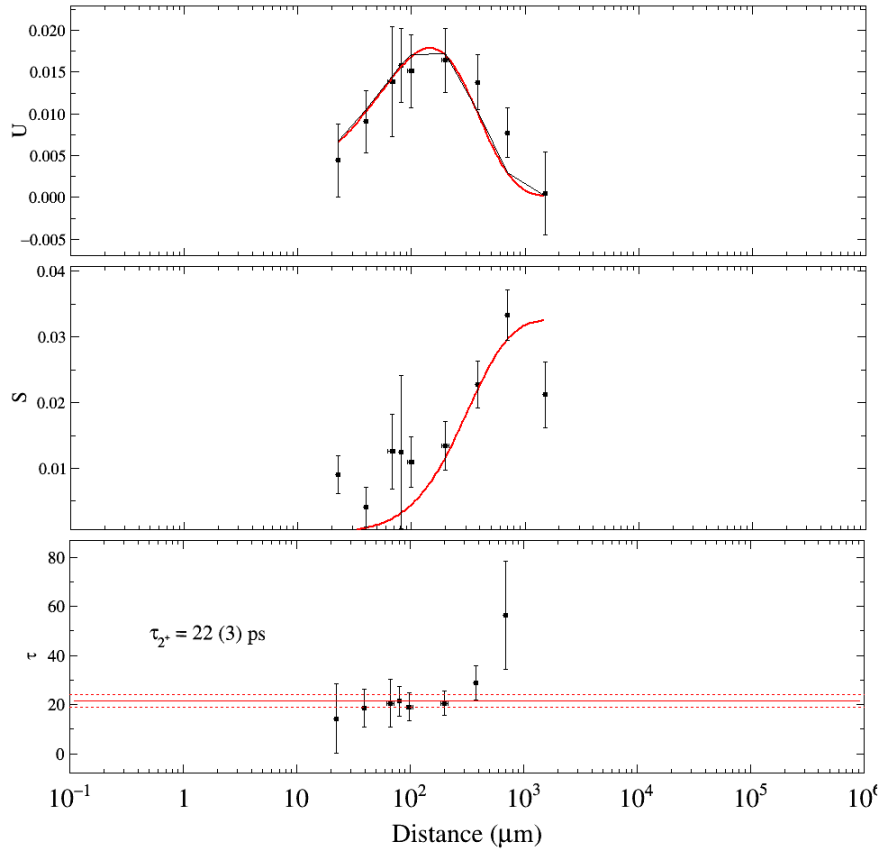
FIGURE 5.8: The experimental points and fits of the unshifted and shifted component of $2^+ \to 0^+$ transition are represented in the upper and central panels. The red lines show the fits. At the bottom is represented, for corresponding distances, the ratio of the unshifted experimental values and the derivatives of the shifted component fit.

The equation 5.1 gives the reduced transition probability from an initial state to a final one.

$$B(\lambda, j_i \to j_f) = \frac{1}{2j_i + 1} |\langle j_f | M(\lambda) | | j_i \rangle|^2 \tag{5.1}$$

$$T(E2) = 1.22 \times 10^9 E^5 B(E2) \tag{5.2}$$

Being the transition probability the inverse of the lifetime, the reduced transition probability is calculated via the relation shown in equation 5.2. T(E2) is in sec^{-1}, B(E2) in $e^2 fm^4$ and the energy in MeV.

The reduced transition probability does not depend on energy and provides a better insight of the magnitude of the correlations. The lifetimes determined in

this chapter are used to calculate the reduced transition probabilities listed in table 6.1.

TABLE 5.5: Reduced transitions probabilities determined for the $4^+ \rightarrow 2^+$ and $2^+ \rightarrow 0^+$ transitions.

$B(E2, 4^+ \rightarrow 2^+)(e^2 fm^4)$	$B(E2, 2^+ \rightarrow 0^+)(e^2 fm^4)$
584 (91)	1688 (230)

5.2   Measurements related to the study of the Octupole collectivity

The octupolar band in ^{112}Xe was identify by J.F. Smith and coworkers [1], firmly from the $I^\pi=5^-$ state lying at 2021 keV excitation energy and tentatively also the $I^\pi=3^-$ state at (1649) keV excitation energy.

In general (see Fig. 5.1), for octupole vibrations as well as for octupolar deformations, the low lying states of the octupolar band de-excite mainly via E1 transitions to the yrast positive parity states [60]. Nevertheless, is the E3 reduced transition probability the one related to the octupolar moment of the nucleus and thus, to the octupole deformation parameter β_3 [60].

As it was mentioned in Chapter 1, the determination of the octupole collectivity through the determination of the octupole deformation parameter, requires both the determination of the lifetime of the low lying states of the octupole band as well as the determination of the E3 branching ratio, in general from the de-excitations $3^- \rightarrow 0^+$ or $5^- \rightarrow 2^-$. This fact makes quite challenging this part of the analysis.

The first step is the determination of the lifetime of the 5^- state. We will do that using the de-exciting dipole transition $5^- \rightarrow 4^+$ with 900 keV, since it is the most intense transition. It has been checked that, within the error of the intensities there is not direct population to the 5^-, since the intensity of the 572 keV $7^- \rightarrow 5^-$ transition is the same as the sum of intensities de-exciting the 5^- state, within the errors.

In order to determine the lifetime of the 5^- state, is necessary to calculate before the effective lifetime of the 7^- state.

Since the tentative (3^-) state is only populated through a low intensity 372 keV transition de-exciting the 5^-, thus it is insufficiently populated to be able to determine the lifetime of the (5^-) state and the $3^- \to 0^+$ branching ratio, I have decided to put the efforts on the much more populated 5^- state.

In order to determine the effective lifetime of 7^- state, I have used the spectra obtained from the matrix, described in section 1 of this chapter, summing the one with coincidence condition in the two components of the $2^+ \to 0^+$ transition plus the one with coincidence condition in the two components of the $4^+ \to 2^+$ transition, shown in Fig 5.9. The intensities determined for the shifted and unshifted components of $7^- \to 5^-$ transitions are listed in table 5.6.
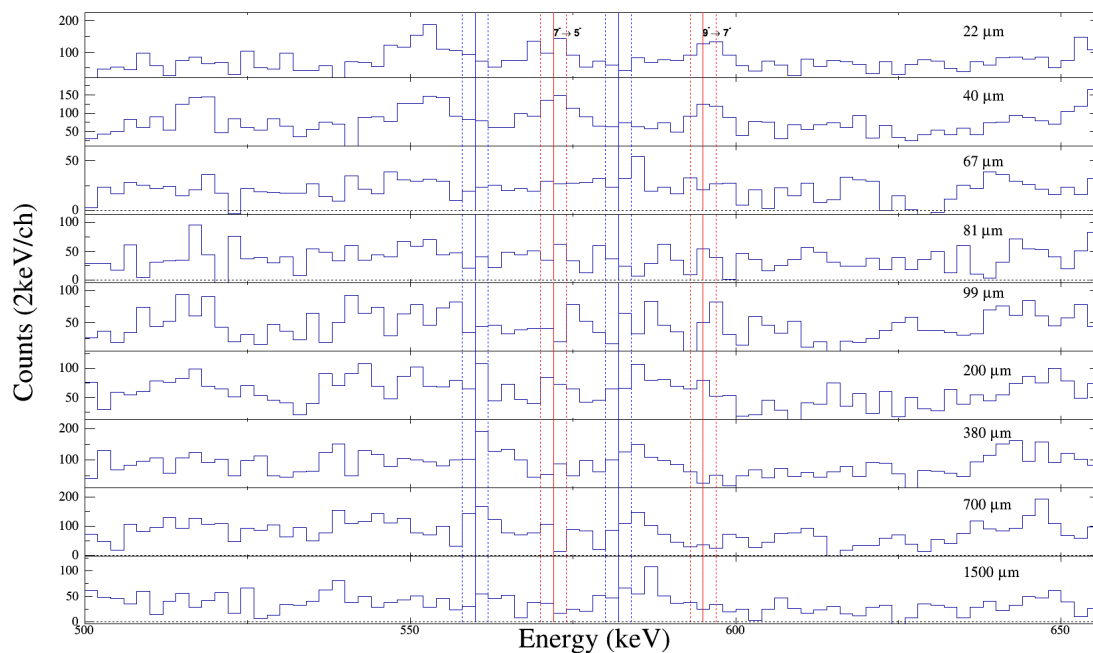
FIGURE 5.9: γ spectra with a coincidence condition in both the shifted and unshifted components of the $4^+ \to 2^+$ 656 keV and the $2^+ \to 0^+$ 466 keV transitions for all measured plunger distances.

The fits obtained with the minimization procedure, for both the DCM and DDCM methods, are shown in 5.10, with results $\tau = 24\ (2)$ ps and $\tau = 23.1\ (14)$ ps respectively.

Once the effective lifetime of the 7^- state has been determined, I proceed to determine the lifetime of the 5^- state using the $5^- \to 4^+$ 900 keV transition, with a coincidence condition in the shifted component of the $7^- \to 5^-$ transition, resulting the spectra shown in 5.11 and using the DDCM described in section 4.5.2.2.

TABLE 5.6: Intensities of both components of the $7^- \to 5^-$ transition, for the various plunger distances, determined from the added spectra with conditions in both components of the the $2^+ \to 0^+$ transition plus the ones with the condition in both components of the $4^+ \to 2^+$ transition.

Distance (μm)	I_s (counts)	I_u (counts)
1500 (15)	105 (15)	15 (20)
700 (15)	361 (26)	65 (18)
380 (15)	402 (27)	104 (22)
200 (15)	105 (19)	92 (18)
99 (6)	47 (17)	107 (17)
81 (3)	20 (13)	59 (14)
39.7 (9)	58 (23)	317 (24)
22.4 (9)	30 (21)	211 (22)
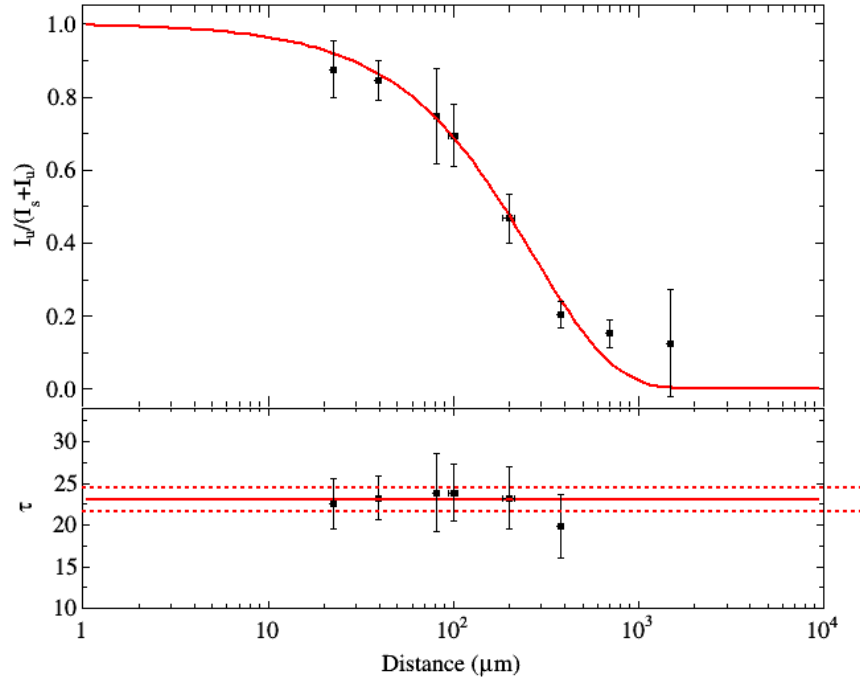
FIGURE 5.10: Effective lifetime of 7^- state in ^{112}Xe determined with DCM (above) and DDCM in the sensitivity region (bottom). The fit is shown as a red line and the uncertainties as dashed red lines.

The areas of the shifted and unshifted components on the $5^- \to 4^+$ transition, with the aforementioned coincidence condition and for the different plunger distances, are listed in table 5.7.

As we have mentioned in previous sections, before applying the DDCM with gated from above in the shifted component, is necessary to apply the normalization
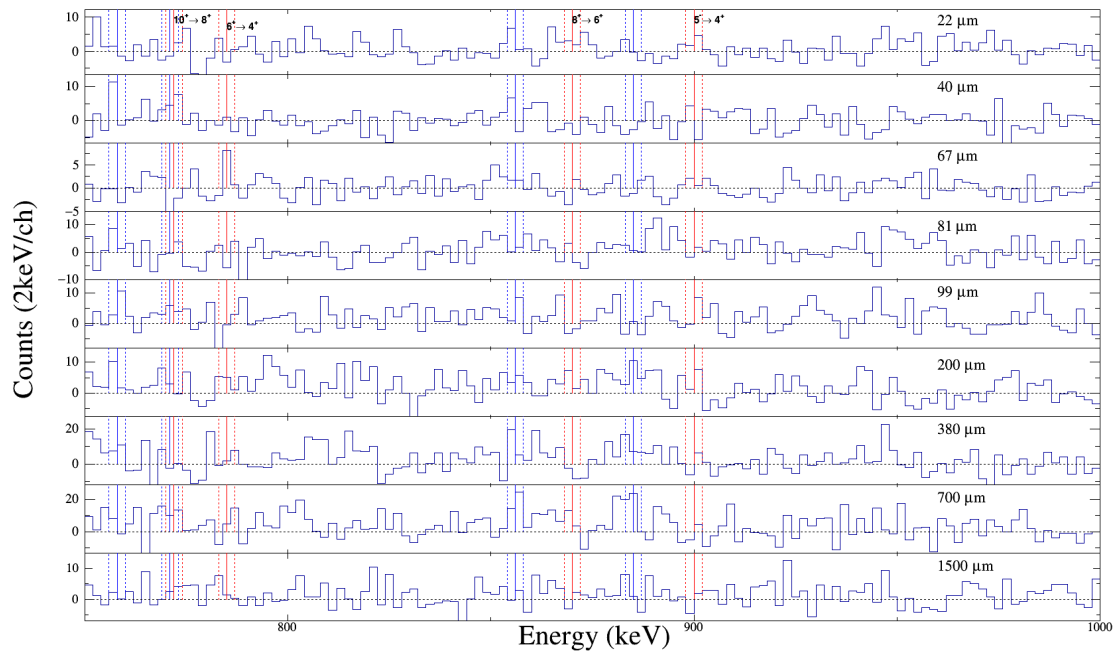
FIGURE 5.11: γ spectra with a coincidence condition in the shifted component of the $7^- \to 5^-$ 656 keV transition for all measured plunger distances.

TABLE 5.7: Areas of the shifted and unshifted components on the $5^- \to 4^+$ transition, with a γ-ray coincidence condition in the shifted component of the $7^- \to 5^-$ transition, for the different plunger distances.

Distance (μm)	I_s (counts)	I_u (counts)
1500 (15)	22 (14)	0 (11)
700 (15)	70 (22)	0 (17)
380 (15)	32 (18)	12 (16)
200 (15)	33 (16)	30 (14)
81 (3)	0 (11)	4 (12)
39.7 (9)	1 (13)	10 (12)
22.4 (9)	18 (14)	19 (12)

factors listed in table 5.4.

In Fig. 5.12 the results of the minimization fit as well as the results of the DDCM procedure is shown. The lifetime obtained with this method for the 5^- state is $\tau = 17(7)$ ps.

The lifetime of the 5^- state has been verified using the DCM with the Bateman equations for two sequential decays, the effective $7^- \to 5^-$ and the $5^- \to 4^+$. The spectra has been obtained from the γ-γ matrix with a coincidence condition in
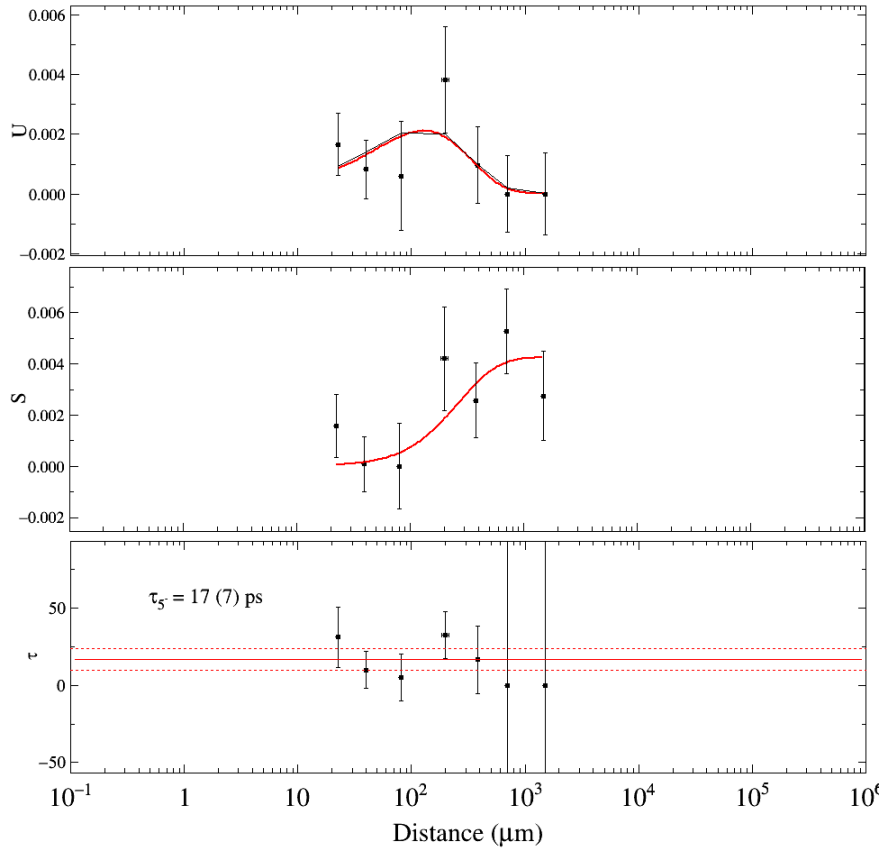
FIGURE 5.12: Above the unshifted and shifted component of $5^- \to 4^+$ transition are represented. The red lines show the fits. At the bottom the lifetime determination of 5^- state in the sensitive region is measured using the DDCM with coincidence condition in the shifted components of the $7^- \to 5^-$ transition.

both components of the $2^+ \to 0^+$ transition, i.e. gated from below, as it is shown in Fig. 5.3 mentioned above.

Since we are determining the lifetime of the 5^- state using the $5^- \to 4^+$ transition, in principle it could be possible to use, the coincidence condition in the two components of the $4^+ \to 2^+$ as well. Nevertheless, due to the fact that the shifted component of the $4^+ \to 2^+$ transition is largely contaminated by the 643 keV transition in ^{112}I, we have decided to exclude the $4^+ \to 2^+$ coincidence condition in the analysis.

Since the coincidence condition in the $2^+ \to 0^+$ in ^{112}Xe is as well in coincidence with the $12^+ \to 10^+$ 919.5 keV transition, between states of the yrast cascade, during the determination of the areas of the unshifted component of our 900 keV transition of interest, in the process of evaluation of the areas, it was necessary to pay attention to avoid unwanted contribution of the 919.5 keV shifted component.

The areas obtained for the shifted and unshifted components of the $5^- \rightarrow 4^+$ transition with the aforementioned conditions are listed in table 5.8. Two distances 99 and 1500 μm were excluded from the analysis.

TABLE 5.8: Areas obtained for the shifted and unshifted components of the $5^- \rightarrow 4^+$ transition from the different plunger distance spectra obtained with γ-ray coincidence condition in both components of the $2^+ \rightarrow 0^+$ transition in ^{112}Xe. Two distances 99 and 1500 μm were excluded from the analysis due to unidentified contaminant.

Distance (μm)	I_s (counts)	I_u (counts)
700 (15)	185 (39)	71 (35)
380 (15)	37 (31)	41 (26)
200 (15)	38 (24)	88 (23)
81 (3)	21 (22)	68 (28)
67 (5)	0 (15)	36(15)
39.7 (9)	0 (25)	125 (28)
22.4 (9)	13 (27)	151 (30)
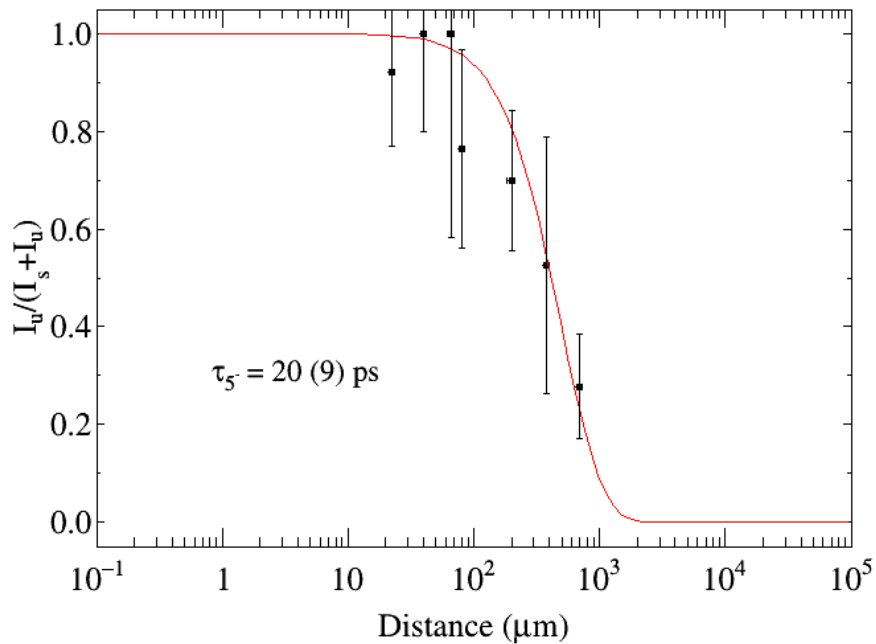
FIGURE 5.13: Lifetime of 5^- state in ^{112}Xe determined with DCM using the Bateman equations for the sequential decay $7^- \rightarrow 5^- \rightarrow 4^+$ fixing the effective lifetime of the 7^- state to 23 ps. The fit is shown as a red line.

The result of the minimization procedure with the fit and the experimental points for the DCM is shown in Fig. 5.13 The result of 20 (9) ps is in agreement with the one obtained with the DDCM technique with gate from above.

We adopted the gated DDCM value $\tau = 17$ (7) ps for the 5^- state.

5.2.1   Determination of the reduced transition probabilities for the $5^- \rightarrow 4^+$ and $5^- \rightarrow 2^+$ transitions

The determination of the lifetime of the 5^- state in ^{112}Xe was reported in the previous section. The reduced transition probability, in this case for the E1 transition, as defined in equation 5.1, can be obtained from the experimental lifetimes or better from the transition probabilities defined as $T = 1/\tau$. The relation between the transition probability and the reduced transition probability for an Electric dipole transition (E1) is shown in equation 5.3. T(E1) is in sec^{-1}, B(E1) in e^{2}fm^2 and the energy in MeV. The B(E1) calculated assuming that the transition $5^- \rightarrow 4^+$ is a pure electric dipole, the lifetime 17(7) ps, obtained for the 5^- state and the branching ratio of the $5^- \rightarrow 4^+$ 900 keV transition $b_{ratio} = 0.82$ is presented in table 5.9.

$$T(E1) = 1.59 \times 10^{15} E^3 B(E1) \tag{5.3}$$

TABLE 5.9: Reduced transitions probability determined for the $5^- \rightarrow 4^+$ transition.

$B(E1, 5^- \rightarrow 4^+)(e^2 fm^2)$
4.1 (18) x 10^{-5}

When a state decay with two or more transition to different final states, it is necessary to obtain the partial lifetimes corresponding to a transition or directly obtain the corresponding transition probability as $T = 1/\tau \times b_{ratio}$ where b_{ratio} is the branching ratio corresponding to the transition of interest.

In order to investigate the octupole collectivity, in the nucleus studied in this work, we need first the lifetime of the 5^- state, already determined and reported in the previous section, and we need as well the branching ratio of the E3 transition de-exciting the 5^- state into the yrast 2^+ state that should have a transition energy of 1556 keV. An E3 transition with this energy will de-excite mainly by γ-ray emission. The 5^- state can de-excite mainly by three transitions the known intense 900 keV $5^- \rightarrow 4^+$ and the lower intensity 372 keV $5^- \rightarrow 3^-$, moreover, the 1556 keV E3 $5^- \rightarrow 2^+$ should be also possible.

The relative intensities of the three γ-rays are necessary to determine the transition probability and be able to establish the reduced transition probability.

Unfortunately, a Plunger experiment is not ideal to determine transition intensities, specially the small ones, since the intensity of a transition is divided between the shifted and unshifted components. Additionally, we have to use coincidence conditions to get a clean spectra. The best combination we have found for the determination of the relative intensities is the sum of the spectra corresponding to the smaller plunger distances, i.e. 22 and 40 μm with a coincidence condition set in the unshifted component of the 466 keV $2^+ \rightarrow 0^+$ transition. The relative intensities (branching ratios) for the three aforementioned transitions have been determined as 82 (12)% for the 900 keV transition, 17(5)% for the 372 keV transition and 1(2)% for the 1556 keV transition.

Unfortunately, the relative intensity of the E3 1556 keV transition seems to be below the sensitivity limit with an error that makes its intensity compatible with 0 to 3% with 68% confidence level.

While the partial lifetime for a 1556 keV transition with 1% would be about $\tau(5^- \rightarrow 2^+) = 1696$ ps to be compared with $\tau (5^- \rightarrow 2^+) = 1600$ (300) ps for the equivalent transition in ^{114}Xe, with similar transition energy, the associated error does not allowed to establish a value.

The only firm result we could establish in the present work is an upper limit for the B(E3, $5^- \rightarrow 2^+$) < 141000 e^{2}fm^6 that corresponds to a B(E3, $5^- \rightarrow 2^+$) < 189 W.u.

Chapter 6

Discussion of the experimental results

6.1 Introduction

The aim of this thesis is to study the evolution of the quadrupole and octupole collectivity in light Xe isotopes when approaching the N=Z line through the lifetime measurement of the excited states of ^{112}Xe (the analysis was reported in the previous chapter) where the reduced transitions probabilities were determined.

6.2 Theoretical Interpretation

Two of the most successful models which describe the structure of the atomic nucleus, the Shell Model and Mean-Field, will be used to discuss the experimental results of this work. While the theoretical calculations are not my personal work, for completeness I will devote a section of this chapter to introduce the two models used in the interpretation. A section of this chapter will describe both methods. Collective deformation in the light Xenon isotopes will be discussed. Finally, at the end of the chapter it will discuss the Large Scale Shell Model (LSSM) results for ^{112}Xe already published [61] and the Self-Consistent Mean-Field (SCMF) calculations. Being the latter, a calculation using the Beyond-Mean-Field (BMF) technique, Symmetry-Conserving Configuration Mixing (SCCM) calculation was

performed with the Gogny D1S energy density functional by the theoretical group from Madrid at CIAFF-UAM in charge of T. R. Rodrguez and L.M. Robledo.

6.3 Deformation of light Xenon isotopes

In the region of the doubly magic ^{100}Sn, where the N=Z and a double shell closure exists, the collectivity grows up with the number of particles in the valence orbitals. Additionally, in the description of nuclei in the vicinity of N=Z, it is necessary to take into account the major neutron-proton correlations take place when the valence neutrons and protons occupy identical orbital.

An early theoretical work and revision of experimental results by S. Raman and collaborators [62] attempted to shed light on the collective behavior of the light Xe isotopes. The authors established the maximum of collectivity towards the mid shell at N=66, as one would expect, and described a decreasing trend for both heavier Xe isotopes towards the N=82 shell closure and for the lighter ones towards N=50.

They also deduced that one should expect a prolate deformation for the full isotopic chain. For the lighter Xe isotopes, the work made use of the existing systematics and modeling of quadrupole deformations in nuclei to draw a complete picture of what experiments should be expecting when performed. The empirical model (based on systematics), shell model and algebraical models were successful with the heavier Xe isotopes but could not reproduce the B(E2) values at N=66 [62]. On the other hand several collective models, including Wood-Saxon, Relativistic Mean-Field or Hartree-Fock, were able to predict the B(E2) around mid shell but had mostly limited success with the heavier Xe isotopes [62].

The relevant results for our discussion is that most of the collective models, discussed in the work, predict a persistence of the deformation for ^{112}Xe with B(E2; $0^+ \rightarrow 2^+$) between 0.8 and 1 e^{2}b^2.

In the experimental work by M. Sandzelius and collaborators [4] the excitation energies of the low lying states of the neutron-deficient N=Z+2 ^{110}Xe nucleus have been investigated. The experimental findings indicate a breaking of the normal trend of increasing first excited 2^+ and 4^+ state energies when the neutron number decreases. Suggesting a breaking of the normal trend of decreasing collectivity as

the neutron number approaches the N=50 shell closure [4]. While the expectation
is the onset of a seniority coupling approaching the shell closure, the persistence
of collectivity is suggested to arise from a high isoscalar n-p interactions near
the N=Z line. However, we are dealing with a region of low deformation and a
more clear indication of the persistence of collectivity should come from the reduce
transition probability measurements.

While ideally one would prefer to study the ^{110}Xe, unfortunately this nucleus is
beyond reach for conventional measurements with stable beams to determine the
lifetime of the states and we have instead studied the neighboring ^{112}Xe, with
4 protons and 8 neutrons outside the N=Z=50 shell closure, where the reduced
transition probabilities are still unknown.

6.4 Systematics on Xe isotopes

In the already quoted work by M. Sandzelius and collaborators [4], in addition to
their findings in ^{110}Xe, the authors also presented the systematics of the 2^+ and
4^+ excitation energies of the Xe isotopes. I have collected in Fig. 6.1 the ratio of
2^+ and 4^+ state energies, R_{42}, but for completeness I also included the systematic
of 2^+ and 4^+ states energy ratio for the corresponding isotones in Te and and Sn.
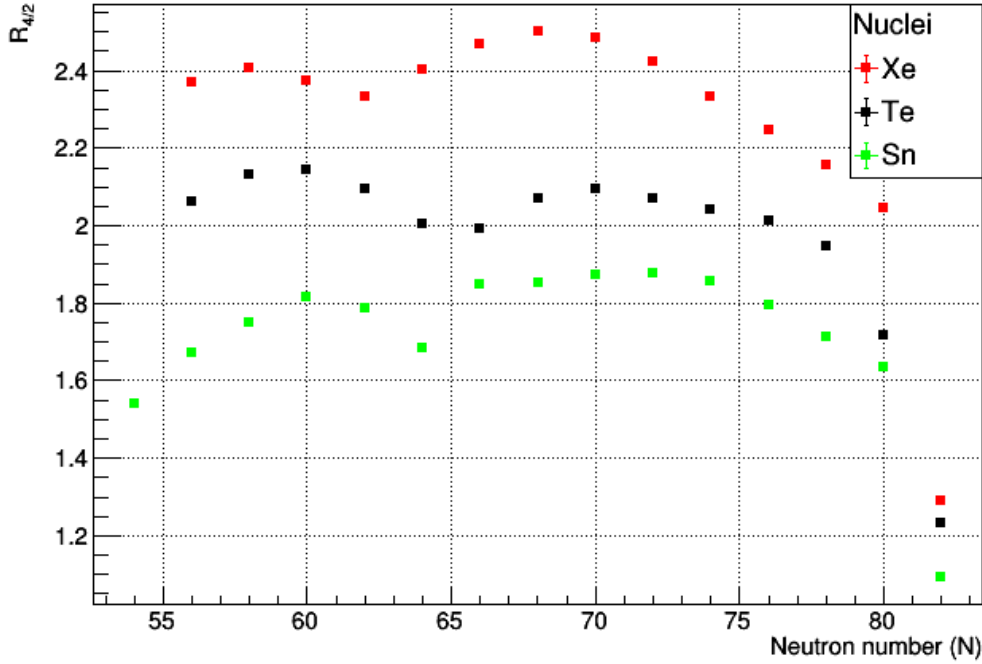
FIGURE 6.1: Ratio of 2^+ and 4^+ state energies as a function of the neutron number of the Xe, Te and Sn isotopic chains nuclei.

The reduced transition probabilities for the $0^+ \to 2^+$ and $2^+ \to 4^+$ transitions in the nucleus ^{112}Xe under study are collected in table 6.1.

TABLE 6.1: Experimental reduced transition probabilities of 2^+ and 4^+ states in the nucleus ^{112}Xe.

$B(E2, 0^+ \to 2^+)$ (e^2b^2)	$B(E2, 2^+ \to 4^+)$ (e^2b^2)
0.84 (12)	0.105 (16)

In Fig. 6.2 and 6.3 are shown the reduced transition probabilities for the $0^+ \to 2^+$ and $2^+ \to 4^+$ transitions known for the Xe isotopes respectively, the figures include the results of the present work. The corresponding reduced transition probabilities for the isotones in Te and Sn are as well shown for comparison. In both figures is clearly visible a maximum of collectivity for Xe compared with the isotones in Te and Sn, specially towards mid shell at N=66. The trend of reducing collectivity when moving from mid shell (N=66) towards both neutron magic numbers N=50 and N=82 is visible in the B(E2, $0^+ \to 2^+$).

The particularity of a very low B(E2, $2^+ \to 4^+$) observed in ^{114}Xe (N=60) is even more pronounced in our measurement for ^{112}Xe (N=58).
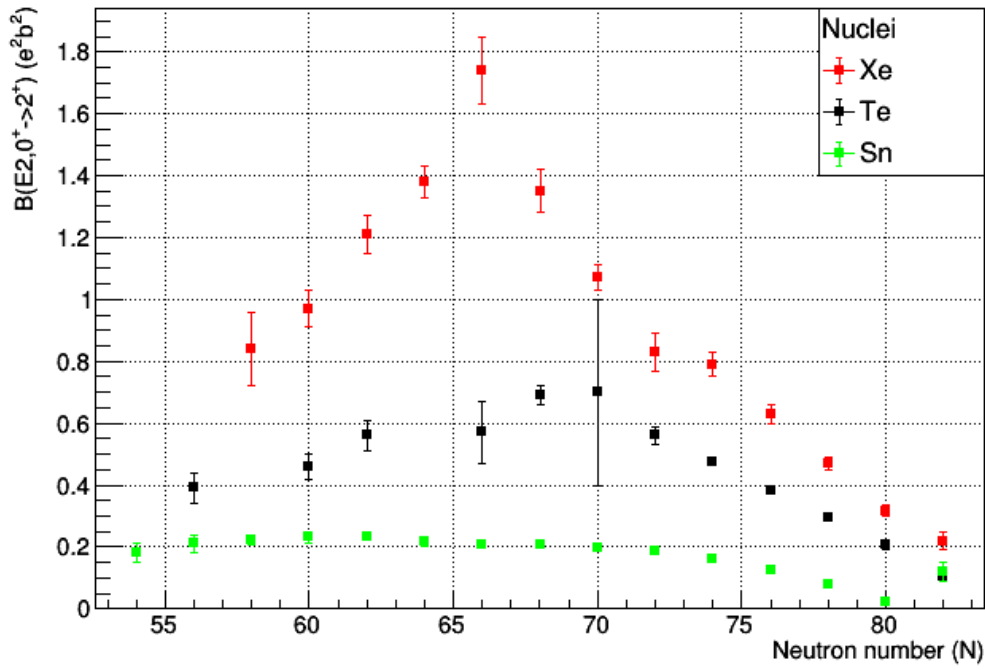
FIGURE 6.2: B(E2;$0^+ \to 2^+$) as a function of the neutron number of the Xe, Te and Sn isotopic chains nuclei.
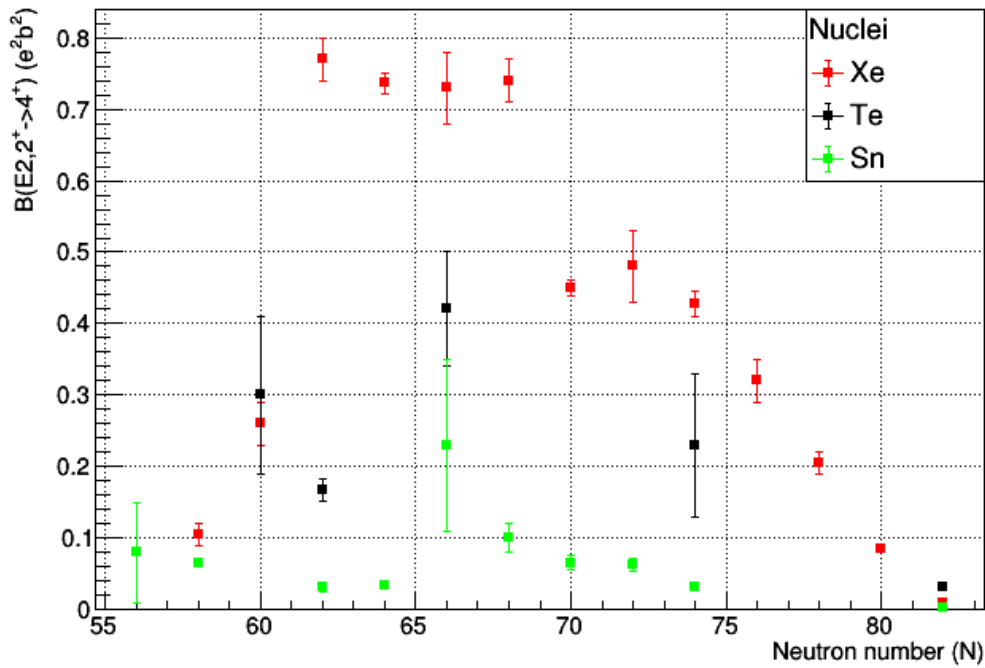
FIGURE 6.3: B(E2;$2^+ \to 4^+$) as a function of the neutron number of the Xe, Te and Sn isotopic chains nuclei.

The B(E2; $4^+ \rightarrow 2^+$)/ B(E2; $2^+ \rightarrow 0^+$) ratio in ^{112}Xe presents as well a anomalous low value for a quadrupole deformed nucleus, also following the trend established by the ratio in ^{114}Xe (see Fig. 6.4). In the figure is shown a value of B(E2; $4^+ \rightarrow 2^+$)/ B(E2; $2^+ \rightarrow 0^+$) = 1.43 as an ideal rotor (known as the Alaga rule), and 2 for a harmonic vibrator.
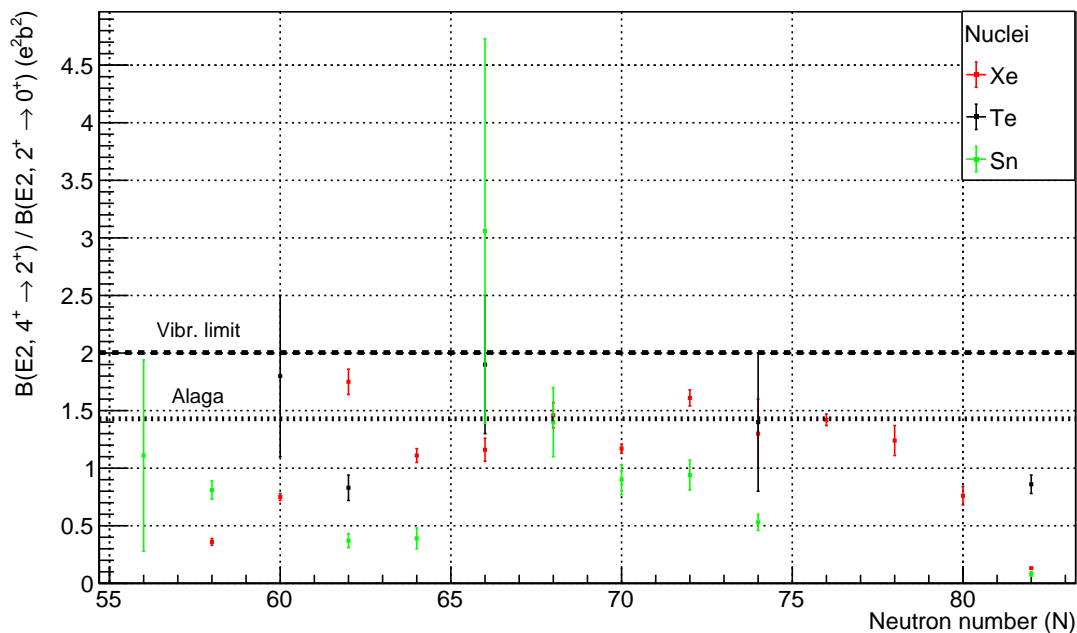
FIGURE 6.4: B(E2;$4^+ \rightarrow 2^+$)/ BE2($2^+ \rightarrow 0^+$) as a function of the neutron number of the Xe, Te and Sn isotopic chains nuclei.

6.5 Introduction to the Shell Model and Mean-Field methods

6.5.1 The Large Scale Shell Model calculations

Since the first nuclear model considering the nucleus as a charged liquid drop, a significant number of models have been used to describe properties of the atomic nucleus. The experimental binding energy in nuclei, increasing in precise numbers of protons and neutrons, called magic numbers, and the systematics of spins and parities lead to the onset of Shell Model (SM) theory.

Initially, the Shell Model was mainly successful describing doubly-magic nuclei and nuclei near them. However the nuclei far from the shell clousures which present deformations and, thus, collectivity, are more complicated to describe and, only with Large Scale Shell Model calculations, it was possible to achieve an accurate description of nuclei far from the magic numbers, where collectivity plays an important role.

The origin of the Shell Model is the Independent Particle Model (IPM) that describes the motion of the nucleons under a spherical mean-field, i.e. each nucleon is assumed to be moving in an external field created by the remaining A - 1 nucleons [63]. Under the IPM, strongly interacting nucleons become non-interacting particles under the influence of an external field. Early attempts to explain the nuclear magic numbers with harmonic oscillator mean-field potentials were successful only for the first three magic numbers (2, 8, 20). Only with the introduction of a spin-orbit term (see equation 6.1) in the mean-field potential by Maria Goppert Mayer and Hans Jensen [64, 65] was possible to reproduce all known magic numbers.

$$U(r) = \frac{1}{2}\hbar w r^2 D\vec{l}^2 + C\vec{l}\cdot\vec{s} \tag{6.1}$$

The IPM is a crude approximation for describing the atomic nucleus. This is because the nucleons are assumed not to interact with each other. The real potential is not a mean-field potential but it could contain two-body forces (see equation 6.2) and, in general also many-body terms.

$$H = \sum_i T_i + \sum_{i,j} V_{ij} \qquad (6.2)$$

The Shell Model provides an extension of the single-particle model to include the dynamics of several nucleons outside closed shells in terms of a residual interaction.

There are a number of factors that make possible the Shell Model but the most relevant are: first it is possible to solve the Schrodinger equation in by expanding the many-body state in terms of a complete set of basis states. In particular the oscillator orbits define a basis of Slater determinants and it is possible to solve the problem diagonalizing a matrix. The second, is that the basis can be taken small enough to be tractable. This factor has a physical nature related with the shell closures. The Hamiltonian of our many-body problem must be transformed into an "effective" one, adapted to the restricted basis, the so-called valence space. The effective interaction accounts for the effects of the external space projected into the valence space.

$$H = H_0 + W_{res} \qquad (6.3)$$

Where the H_0 is the mean-field Hamiltonian and W_{res} takes into account the residual interaction. The early shell model hardly to reconcile with the idea of rotational motion in nuclei. The microscopic origin of quadrupole deformation was first described by J.P. Elliott in 1958 with the introduction of the quadrupole force and the underlying SU(3) symmetry that are the foundations of rotational motion. However, even after the introduction of realistic matrix elements (that include the quadrupole and pairing interactions), the limit of tractable dimensionalities were insufficient to allow the shell model to describe rotational motion. The first successful Shell Model description of the rotational motion arrived with the Large Scale Shell Model (LSSM) in the fp-shell by E. Caurier and collaborators [61]. In this work the deformed collective behavior of the ^{48}Cr nucleus was described in both, the laboratory frame, by means of the spherical shell model and with a mean-field description in the intrinsic frame.

6.5.2   Beyond mean-field method

In this section we will introduce briefly the Beyond mean field method to describe deformed collective motion in nuclei. Theoretical results with this method will be used in the discussion of the experimental results. In particular self-consistent mean-field models, where the potential well for nucleons is computed from the nucleonic wave functions and it is generalized to include a pairing field, in the Hartree-Fock-Bogoliubov method.

Self-consistent mean-field (SCMF) methods, like Hartree-Fock-Bogoliubov (HFB), and their beyond-mean-field (BMF) extensions are very suitable tools to study the structure of atomic nuclei in the whole nuclear chart with interactions that are not fitted to any particular region [66, 67]. They use the variational method to find approximate energies and wave functions of the exact nuclear many-body problem. One of the most advanced BMF techniques is the so-called symmetry-conserving configuration mixing (SCCM) method with energy density functionals (EDF).

6.6   Theoretical results based in the LSSM calculations

In the shell model framework, specifically using Large-Scale Shell model (LSSM) calculations, lighter xenon isotopes have been studied in the valence space r4h, which contains a pseudo-SU(3) triplet plus the intruder orbit $0h_{11/2}$, including all the orbits between the magic closures N=Z=50 and N=Z=82 by Caurier and collaborators and the results have been published in Ref. [6]. The authors mention in the work that the shell model description of this isotope is a real challenge because the dimension of the basis in the full space calculation is close to 10^{10}. Experimental data is reproduced and the calculations show collective deformed structures of triaxial nature, using the effective interaction GCN50:82 in r4h. There is a competition between the quadrupole correlation enhanced by the pseudo-SU(3) structure of the positive parity orbits and the pairing correlations provided by the $0h_{11/2}$ orbit. According to the method, the triaxiality in ^{108}Xe is larger than in ^{110}Xe due to the neutron contribution.

Experimentally, it is seen that collectivity increases in mid-shell for light xenon isotopes reaching a maximum in ^{120}Xe with 16 valence neutron but the theoretical model cannot reproduce the predicted intrinsic quadrupole moments. It is necessary to expand the valence space to have more quadrupole collectivity or to include the $1f_{7/2}$ neutron orbit, i.e., the quasi-SU(3) partner of the $0h_{11/2}$. For isotopes heavier than ^{110}Xe, if some valence nucleons occupy the quasi-SU(3) orbits mentioned before, there will be an increase of the quadrupole moments up to ^{120}Xe as appears in the experimental data. The model has reproduced quite well the experimental results [6]. For ^{112}Xe the exploratory calculations show an increase of the B(E2, 2+ $\rightarrow$ 0+) from 1130 e^{2}fm^4 (0.113 e^{2}b^2) in the pseudo-SU(3) valence space to 1460 e^{2}fm^4 (0.146 e^{2}b^2) in the space corresponding to the pseudo + quasi-SU(3) schematic model. Therefore, to reproduce the experimental data for the B(E2, 2^+ $\rightarrow$ 0^+), the complete scenario with the pseudo and quasi-SU(3) will be necessary.

Regarding the B(E2, 4^+ $\rightarrow$ 2^+), the calculations published in Ref. [6] only quote the plain shell model results without including the quasi-SU(3), nevertheless, with a B(E2, 4^+ $\rightarrow$ 2^+) calculated to be 1560 e^{2}fm^4 (0.156 e^{2}b^2) and a Q_0 compatible with a deformation with β=0.17, the results do not agree with our experimental finding of B(E2, 4^+ $\rightarrow$ 2^+) = 584 e^{2}fm^4.

6.7 Theoretical results based in the Beyond mean-field method

^{112}Xe nucleus is described using a symmetry-conserving configuration mixing calculation performed with the Gogny D1S energy density functional by the theoretical group from Madrid at CIAFF-UAM in charge of T. R. Rodrguez and L.M. Robledo.

In the present work, the SCCM method is implemented with the well-tested Gogny D1S EDF as the underlying nucleon-nucleon interaction [67]. Once the interaction is chosen, the variational ansatz determines the quality of the approximation and the observables that can be obtained theoretically. Here, the nuclear wave functions with a given angular momentum (J) and parity (π) are defined as linear combinations of particle-number, parity and angular momentum projected HFB

states:

$$|J_\sigma^\pi\rangle = \sum_{(\beta_2,\beta_3)} f_\sigma^{J\pi}(\beta_2,\beta_3) P^\pi P^N P^Z P^J |\Phi(\beta_2,\beta_3)\rangle \tag{6.4}$$

where P^π, $P^{N(Z)}$ and P^J are the parity, neutron (proton) number and angular momentum projection operators, respectively. The intrinsic HFB states, $|\Phi(\beta_2,\beta_3)\rangle$, are obtained by solving the HFB variational equations with constraints to enforce the HFB wave function to have a given axial quadrupole (β_2) and octupole (β_3) deformations. Finally, the coefficients of the linear combination, $f_\sigma^{J\pi}(\beta_2,\beta_3)$, are found by solving the so-called Hill-Wheeler-Griffin (HWG) variational equations following the generator coordinate method framework ($\sigma = 1, 2, ...$ is labelling the states for a given parity and angular momentum). The solutions of the HWG equations provide: a) the ground state (g.s.) and excited state energies ($E_\sigma^{J\pi}$); b) the wave functions that can be used to evaluate electromagnetic properties; and, c) the collective wave functions (c.w.f.) that give the probability of having a given deformation in a given specific state. The reader is referred to Refs. [67],[68] for a more detailed description of the SCCM method and its implementation in the present work.

The first insight about the collective structure of a given nucleus can be inferred from the total energy surface (TES) that corresponds to the evaluation of the HFB energy as a function of the collective degrees of freedom, i.e., axial quadrupole and octupole deformations in this case. In Fig. 6.5(a) we observe that the nucleus ^{112}Xe shows two minima at $\beta_3 = 0$ and $\beta_2 \approx +0.25$ and $\beta_2 \approx -0.2$.

The absolute minimum corresponds to the prolate configuration and, in this case, the degeneration along the β_3 is larger than in the secondary minimum. Nevertheless, the nucleus at the mean-field level does not present a permanent octupole deformation despite the ^{112}Xe has only two neutrons more than the octupole magic number $N = 56$. Hence, we can extract from the TES that the most relevant degree of freedom will be the quadrupole deformation in this calculation.

The next step is the symmetry restoration (parity, particle number and angular momentum) and mixing of the HFB states. After solving the HWG equations we obtain the c.w.f.'s and the energies. In the low-energy part, we obtain two $\Delta J = 2$ bands for ^{112}Xe, namely, the positive parity g.s. band built on top of the 0_1^+ state and a first excited negative parity band with a 1_1^- state as the band-head. In Fig. 6.5(b)-(c) the c.w.f.'s for the band members 2_1^+ and 3_1^- are represented. The

rest of the c.w.f.'s of the states belonging to the same band shows a very similar structure, proving the band character of such sets of states.

For the positive parity band, the c.w.f. is distributed around the prolate minimum observed in the TES with its maximum at $\beta_2 \approx +0.25, \beta_3 = 0$ while for the negative parity band the larger contributions are obtained at the same quadrupole deformation but at $\beta_3 \approx \pm 0.2$ (these c.w.f.'s are symmetric about $\beta_3 = 0$ since the nuclear interaction does not break the parity symmetry). The correlation between the c.w.f.'s of the two bands indicates a strong quadrupole-octupole coupling in this nucleus.

Finally, the predicted energies are shown in Fig. 6.5(d). Here we see that the spectrum is systematically stretched with respect to the experimental results although the qualitative behavior is well-reproduced. This is a well-known effect of the present SCCM implementation with axially symmetric intrinsic HFB states. In this case, the ground state is variationally favored with respect to the excited state energies and causes the stretching observed in the theoretical spectrum. A natural way to improve the variational method is the inclusion of degrees of freedom missing in the present SCCM calculations, namely, triaxiality and cranking (intrinsic rotations). These two additional degrees of freedom help to explore better the variational space of $J \neq 0$ states and tend to compress the spectrum provided by the theoretical prediction. Unfortunately, the prohibitively large computational cost prevents their inclusion with Gogny EDFs at present.

In the work of M. Sandzelius at al., Ref. [4], the authors discuss as well the total Routhian surface (TRS) calculations based on the cranked Strutinsky formalism, using a hamiltonian of a rotational nucleus, make known the minimum energy as a function of the deformation parameters β_2, β_4, and γ at moderately deformed prolate shapes with the elongation parameter β_2 gradually decreasing as a function of decreasing neutron number, from $\beta_2 \approx 0.23$ for ^{116}Xe to $\beta_2 \approx 0.17$ for ^{110}Xe. This would correspond to a $\beta_2 \approx 0.19$ for ^{112}Xe, the TRS calculations predict a continuous decrease in B(E2) as a function of decreasing neutron number N [4].

6.8 Discussion and conclusions

In order to examine the character of the excitation spectrum a very good indicator is R_{42} defined as a relationship of the lowest 4^+ and 2^+ excitation energies, depicted
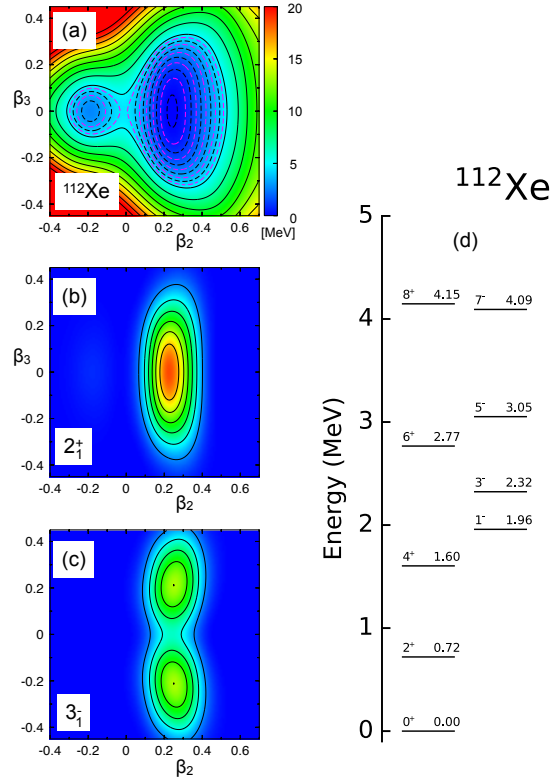
FIGURE 6.5: (a) HFB total energy energy surface, (b)-(c) collective wave functions for the 2_1^+ and 3_1^- state, and, d) SCCM energy spectrum computed with the Gogny D1S interaction.

in equation 6.5.

$$R_{42} = \frac{E(4_1^+)}{E(2_1^+)} = E4/E2 \tag{6.5}$$

The values of the R_{42} indicator show the character of the spectrum; 10/3 as an axial rotor, 2 as a vibrator and 5/2 as a γ-unstable rotor. In reference [69], the good agreement between the R_{42} indicator with the intrinsic shape properties of the CHFB+5DCH wave function is studied.

For most nuclei the R 42 values in both measurements and calculations fall between R 42 = 2 and R 42 = 10/3 limits of the vibrational and rotational models, respectively.

In the limit of the vibrational ($R_{42} = 2$) and rotational ($R_{42} = 10/3$) models the measurements and calculations fall. When the two-quasiparticle excitations dominates the ratio is less than 1, generally near magic numbers. Using the reduced

transition probababilities the B_{42}, represented in the equation 6.6, indicates the axial rotor model for which $B_{42} = 10/7$, and the harmonic vibrator model for which $B_{42} = 2$.

$$B_{42} = \frac{B(E2; 4_1^+ \rightarrow 2_1^+)}{B(E2; 2_1^+ \rightarrow 0_1^+)} = B4/B2 \tag{6.6}$$

In the framework of the mean field model, specifically the CHFB+5DCH approximation with the Gogny force [69], it is represented in Fig. 6.6 the ratio of the two indicators B_{42} and R_{42} with all calculated nuclei including ^{112}Xe, purpose of this study.
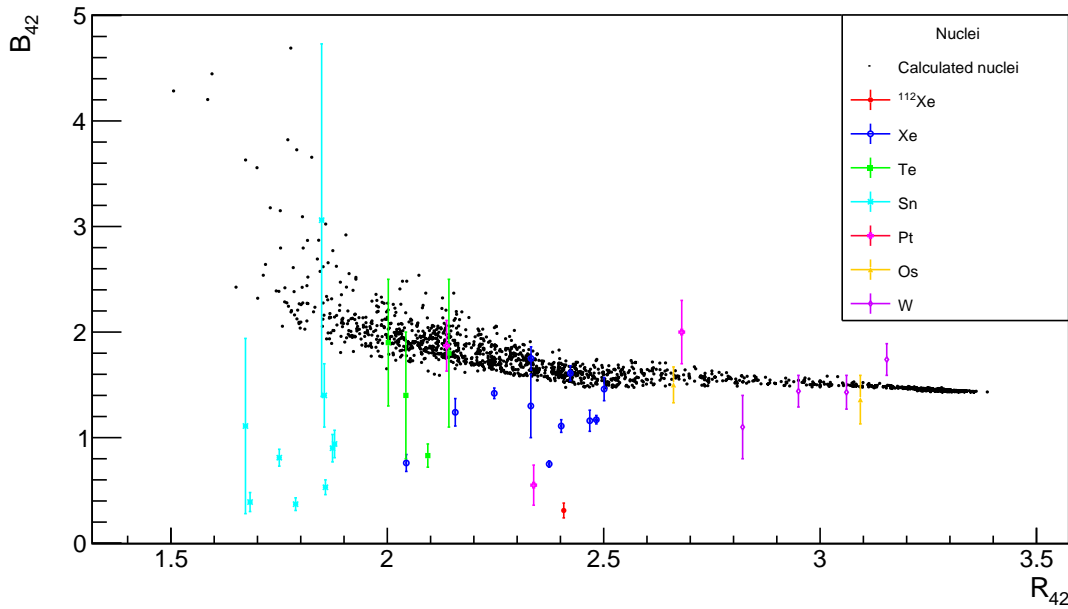
FIGURE 6.6: B_{42} ratio, as a function of the R_{42} one, for all calculated even-even nuclei using a collective Hamiltonian [69] and the cases that deviate from these calculations in the Xe, Te, Sn, Pt, Os and W isotopes. The ratio corresponding to ^{112}Xe, measured in this thesis work, is also included.

The results of the calculations mentioned above are shown in Fig. 6.6, for all calculated even-even nuclei, according to their collective properties. Several experimental results for the Xe, Te, Sn, Pt, Os and W isotopes, including the ^{112}Xe nucleus, that is the object of this study, have been also represented. The figure shows that several of them, in particular the ^{112}Xe nucleus, deviate from the expected theoretical calculations. It can be seen the neutron deficient nuclei out of trend. It can be concluded that the evolution in a standard collective motion with angular momentum is not appropiate for the analysis of the ^{112}Xe nucleus. The

different behaviour of B(E2; $4_1^+ \to 2_1^+$) and B(E2; $2_1^+ \to 0_1^+$) is also studied for the ^{108}Sn in [70], where the B(E2; $4_1^+ \to 2_1^+$) shows that pairing is quite significant, in contrast with the quadrupole dominance indicated by the theoretical calculations. The clue is the balance between pairing and quadrupole correlations in nuclear interaction.

The B(E2; $4_1^+ \to 2_1^+$) is not well reproduced by the theoretical calculations, and the ratio of the reduced transition probabilities, mentioned above, makes it clear. The same situation happened in ^{114}Xe where the calculated quadrupole deformation was determined to be in the 2^+ and 4^+ states, 0.23 (2) and 0.16 (2) respectively [71]. The possible explanation exposed in the reference [71] would be the position of the $h_{11/2}$ orbit which is related to the interplay between rotation and octupole deformation.

In conclusion, while the 2^+ state seems to be well described by all the models (LSSM, BMF and TRS), the 4^+ state remains unexplained. The most logical explanation for the differences between the 2^+ and 4^+ states is a change on deformation between the 2^+ and 4^+ and, therefore, the $4^+ \to 2^+$ decay will not be in this case a transition between states of a rotational band but a transition connecting states belonging to bands of different nature, where the reduce transition probability has to take into account the structural changes in the nucleus.

Chapter 7

Instrumentation: Contribution to the construction of the NEDA detectors

7.1 Introduction

The NEDA neutron detector array has been designed to have high neutron detection efficiency and high performance figures for neutron to γ-ray discrimination, using PSA and ToF techniques. NEDA has been designed to be a complementary detector for large γ-ray detector arrays as AGATA, providing on-line neutron trigger information and high selectivity of the channels in the off-line analysis [32].

The first usage was in the AGATA-NEDA campaign in 2018 in which the experiment described in this thesis took place. This fact links my contribution to the construction of NEDA detectors with their use in the set-up of the experiment carried-out and the data analysis performed in this thesis.

In chapter 2, section 4, I have described the main characteristics and the timing and pulse shape analysis of the NEDA detectors. In this section, the production of the NEDA detectors will be described in detail. The building of the detectors has been done in the facilities of the Laboratori Nazionali di Legnaro (LNL), belonging to the National Institute for Nuclear Physics (INFN) of Italy.

Once the mechanical parts, the photomultiplier (PM) tube, the voltage divider and the liquid scintillator are provided, the production of the NEDA detector requires work to be performed in the laboratory of chemistry and in the NEDA radio-protected bunker.

The leakage test, glass checking, bubbling, shaking and the final closing process are made in the quemical laboratory. Otherwise, the assembly and characterization of the NEDA detectors are realized in the bunker. These procedures, required for the production of the NEDA detectors, are described in the following sections.

7.2   NEDA detector

High γ-neutron discrimination, efficiency, time resolution and low cross-talk between detectors were the goal in the design of a NEDA neutron detector, self produced by the collaboration. Maximizing the detection efficiency, requires the full coverage of the surface occupied by the detectors and this is achieved by searching for a solution for its tiling. Specifically a hexagonal tiling allows to avoid gaps in the surface and helps as well to cover most of the section of the detector. To get the best neutron-γ-ray discrimination, the ELJEN EJ301 (BC501A) liquid scintillator was chosen by the collaboration, albeit its difficulties in handling the scintillator [72] [73].

The optimal depth of the active volume of the detector was choosed by Monte Carlo simulations [74] and also the smallest possible transversal dimension in order to avoid possible losses of efficiency due to scattering cross-talk.

Taking into account the characteristics described above, the final design NEDA detector is shown in Fig. 7.1. It is a hexagonal detector cell of 6060 aluminium alloy with 146 mm side to side distance, 3 mm thick walls and 205 mm length with an active volume of ~ 3.15 litres of EJ301 liquid organic scintillator.

The different parts of the NEDA neutron detector are shown in Fig. 7.2. In the figure it can be seen the active volume (1) of the detector connecting with a pipe to the expansion chamber (4) placed at the top of the PM tube casing (2). The inner surface is covered with TiO_2 based reflective paint EJ520. At the top of the active volume (1) is located a 5″ N-BK7 5 mm thick glass window, that reaches 92% transmittance for the wavelength of interest. Upon completed, the light yield of
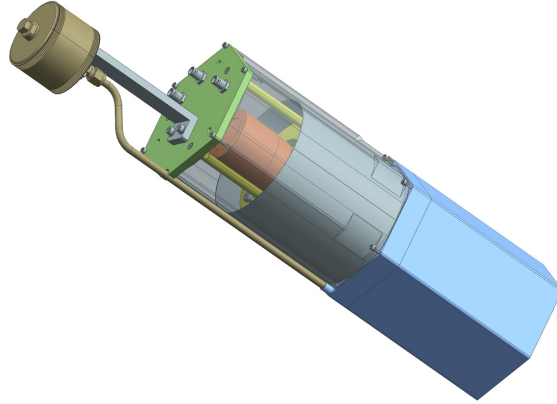
FIGURE 7.1: Design of a NEDA neutron detector. In blue is represented the hexagonal cell where it is the liquid scintillator EJ301. The cell is connected to the expansion bellow, shown in brown, with a pipe. A hexagonal light tight casing contains the photo multiplier tube and voltage divider (orange) as well as a mu-metal shielding (grey). The spring pusher for the PM tube is shown in yellow.

the detector is 2400 (100) photoelectrons/MeV. In order to best cover the section of the detector a 5″ PM tube is necessary (6). It was selected the Hamamatsu R11833-100 PM tube due to the good characteristics for n-γ discrimination [75] and to the good timing properties [76]. As expansion chamber, to compensate pressure variation, we used a welded bellow (4) with a diameter of 3″. The bellow expands to a volume of 153 cm^3 in 4.8 cm stroke, having a range of 5°C and 45°C in temperature without differences in the active volume pressure.

7.3 Sealing the detector with the glass window for the photomultiplier.

Before testing the possible leakages in NEDA neutron detector, the 5″ N-BK7 5 mm thick glass window and the aluminium of the detector have to be well glued. For this purpose, a mix of bottle A and B of TorrSeal was done with the following equation 7.1.

$$A + B = 1.44 \times A \qquad (7.1)$$

First, the desired quantity of bottle A is placed in the weighing scales and then, TorrSeal of bottle B is added until it reaches $(A + B)$ quantity.
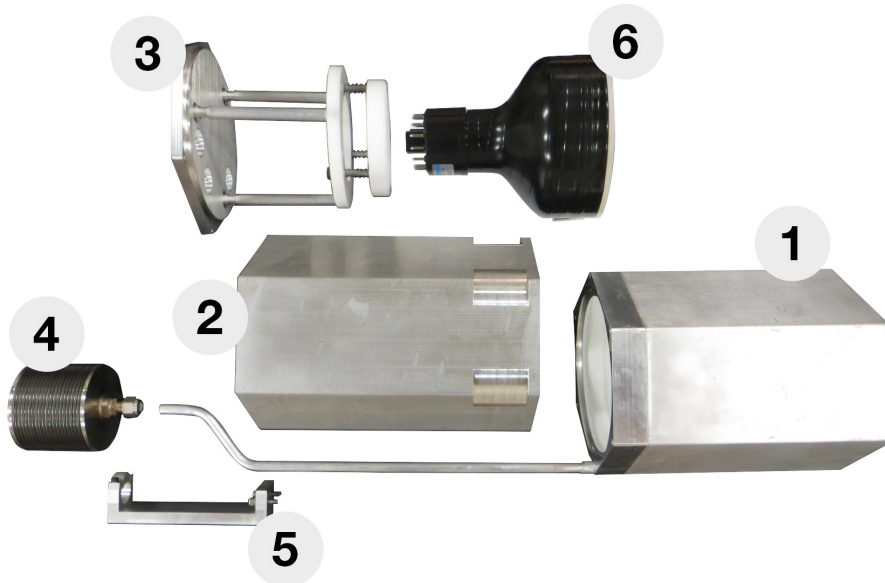
FIGURE 7.2: Parts of a NEDA detector plot. The detector cell with expansion pipe (1), the PM tube casing (2), the PM tube casing lid with a spring pusher for the PM tube (3), the expansion bellow with the swagelock pipe fitting (4), the mechanical support for the bellow (5) and the Hamamatsu R11833-100 PM tube are represented.

7.4 Leakage test

As mentioned before, our neutron detectors are based in the liquid scintillator EJ301 (BC501A). On one hand, this liquid scintillator is based on Xylene that is considered a hazardous compound for being both flammable and toxic. On the other hand, the contact of the liquid scintillator with oxygen degrades the PSA properties. Thus, a very relevant step in the construction of NEDA detectors has to be preparing the detector and making sure that no leakage will occur during the experiment or manipulation of the detector.

In order to check leakages in the detector, the vacuum system is used. This vacuum system works with a scroll pump and a leak tester. Specifically, using the scroll pump the active volume of the detector is pumped up to 2×10^{-2} mbar. Afterwards, applying the leak tester, it reaches up to 10^{-3} mbar using the set-up shown in Fig. 7.3.

The leakage test can be done as soon as the vacuum has been achieved. It is made using helium due to his capability to get through small sealing failures. The detector is checked by the vacuum system and generally, if the glueing process is well done, there will be not leakages. The glass and the swagelock fitting have to
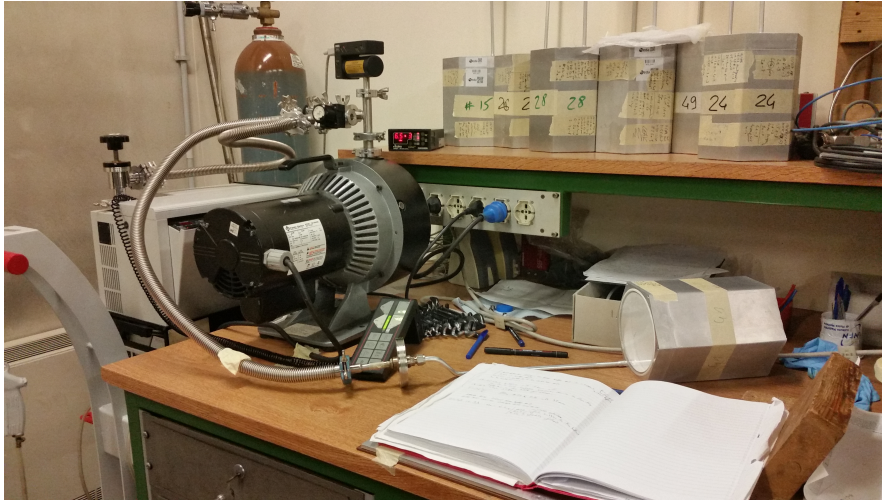
FIGURE 7.3: The vacuum system used for the leakage test in NEDA detectors.

be checked, specially the swagelock fitting has to be strongly screwed to not have leakages. Both should have vacuum performance at the level of 10^{-3} mbar.

In case of leakages, the gluing process and the leakage test must be repeated until the desired vacuum is reached. At the beginning, the vacuum system consisted of a leakage tester but it was needed to add the scroll pump to do a pre-vacuum. The reason is that all the internal surface of the detector, except the glass window, is painted with the reflective paint EJ520. Under vacuum the paint degas organic molecules. After a while, the filters of the leakage tester are blocked and it is needed a system more complicated using the scroll pump that reaches at 10^{-4} mbar. The detector is, therefore, vacuum pumped at least for an hour in the scroll pump first and after, when it reaches the proper vacuum, 2.10^{-2} mbar, then the test process continues using the leak tester.

7.5   Glass checking

After the leakage test, the glass cleanliness is checked in order to discover the possible spots of glue remained in the glueing process. It is done with ethanol, moving this liquid with another glass. A perfect situation would be to move the glass easily, without interferences due to glue blocks. The technique can be seen in Fig. 7.4.

FIGURE 7.4: Checking the crystals of the NEDA detectors.

7.6   Partial filling

At this moment of the building process, the detector is prepared to be filled with the EJ301 liquid scintillator.

Connecting the bottle that contains the liquid scintillator to the bellow of the detector. The filling starts by applying little pressure, using the pressure system, in the liquid scintillator bottle. The filling of the detector is then completed gravitacionally with two liters of E7301 liquid scintillator. Each NEDA detector has a volume of about 3.15 l. This partial filling process is made with a detector in the floor and the liquid bottle in the work bench.

In order to do the next process in a effectively way, the detectors are to be filled with two liters of scintillator liquid and not with the total volume of 3.15 l.

7.7   Bubbling

The aim of the bubbling process is to remove the oxygen of the liquid scintillator since, as mentioned before, oxygen interfere with the liquid scintillator properties. The bubbling has to be done as soon as possible in the mounting process such that bubbles do not appear inside the detector when it is full an ready to be used.

Bubbling must be done for 40 minutes. In the same time two detectors and one bottle (which contains the liquid scintillator) are bubbled since there are three valves and three pipes for this process, as it is shown in Fig. 7.5.

Each detector, which capacity is about 3.15 l, was filled with two litres in order provide space for the bubbling process. In parallel a bottle, whose capacity is 4 l, is bubbled with a maximum of about 3 l.

Then, the necessary bubbled liquid of the bottle goes to the detectors in order to fill to the top in the process of final filling. Before the bubbling of the liquid, the pipes should be very well cleaned with acetone. The pipes connect the valves, which inject the gas pressure to the detectors. This step is done with acetone instead of alcohol because it does not contaminate the liquid scintillator. Before openning the screw of the detector's bellow, this should be perfectly cleaned. As the pipe is getting into the detector, it should be cleaned again and it is necessary to press the bellow in order to insert the pipe properly.

FIGURE 7.5: Bubbling process using NEDA detectors and liquid scintillator bottle.

Afterwards, the main valve and the valves 1, 2 and 3 of the pressure system, that goes directly to the bottle and the detectors, are opened. The set-up can be seen in Fig. 7.6. In order to have the correct pressure, the pressure reducing valve has to be set to 1 atm.

It is appropiate to keep attention to leakages in pipes or valves which could be giving less nitrogen's pressure in the detector. After bubbling, detectors are filled to the top (about 3.15 liters) and they are prepared for the next step of the building process, the shaking. In the process of bubbling N_2, into the liquid scintillator, we

have created small or micro bubbles inside the liquid and the only way to get rid of them in short time is shaking the detector.

When the filling ends, the expansion bellow is just closed with an estimate of the volume needed such that the N_2 bubbles generated in the shaking have enough space.

FIGURE 7.6: The pressure system of the NEDA detectors bubbling process.

7.8   Shaking

NEDA detectors are shaked for a long time in order to remove the nitrogen, introduced the bubbling process, inside the shaker at 110 rpm. To avoid a possible damage, the detectors are tied and protected with polyethylene foam, as it is shown in Fig. 7.7.

If there is a bubble after shaking, example shown in Fig. 7.8, it is extracted from the detector and the shaking process has to be repeated, until there is no more bubble production. After shaking it is necessary to do the overpressure test. This is performed by applying pressure on the expansion bellow and look for
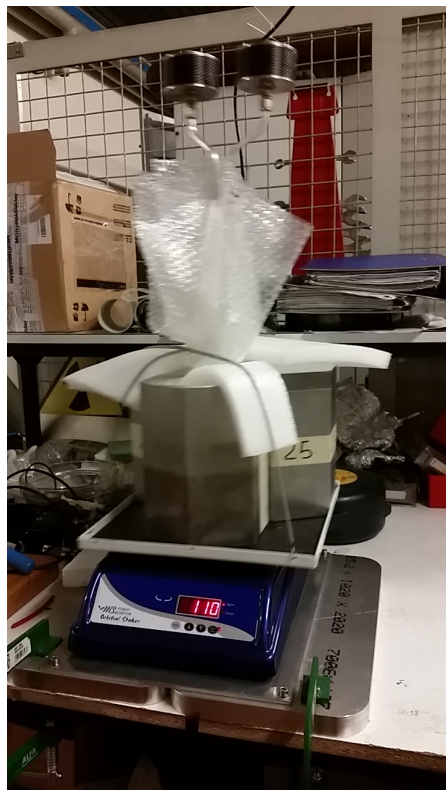
FIGURE 7.7: Shaking process for NEDA detectors.

leakages between the glass window and the TorrSeal or between the TorrSeal and the aluminium. Then, the next step is the final closing.

FIGURE 7.8: Bubble generation after shaking process.

7.9 Final Closing

The final closing is the last step in the process of building detectors in the chemical laboratory. It is performed only when the process of releasing N_2 from the

scintillator (also known as shaking) is finished.

The steps for the final closing of detectors are:

1. Have the materials prepared like the dynamometrical key (showed in Fig. 7.9) with a strength fixed on 50 N.m, the mechanical spider (a frame which has radianting members connected by crosspieces) cleaned with acetone and air, acetone, paper (cut into small pieces), smooth paper, needles (to remove the excess of the liquid scintillator) and a recipient (to collect the excess of the liquid scintillator). The support of the spider, presented in Fig. 7.10, is also used.
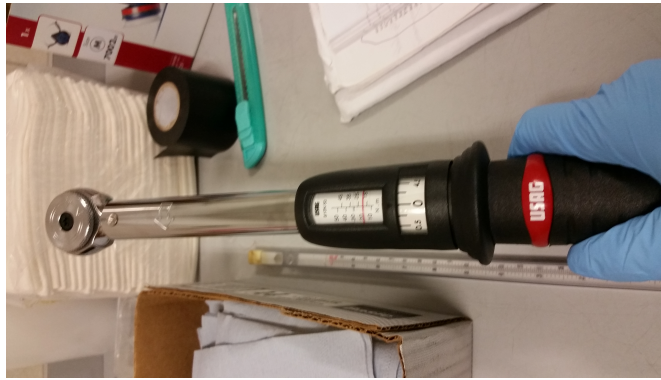
FIGURE 7.9: Dynamometrical key.

2. The bellow that is the expansion chamber of the detector (serves to compensate the pressure changes within sensible limits), has to be adjusted. The temperature of the room has to be measured and the desired lenght of the bellow can be calculated with the equation 7.2.

$$H_d = H_m + 0.9\frac{mm}{K}(T_{room} - T_m)K, \tag{7.2}$$

$$\text{and being } T_b = [5 - 50]°C \tag{7.3}$$

where T_b is the temperature range of the bellow, $H_m = 15$ mm is the squired minimal lengh of the bellow, H_d is the desired heigh of the bellow, T_{room} is the temperature of the room and T_m is the minimal temperature by our expansion chamber (bellow), which is 5°C.

3. The bellow has to be cleaned with ethanol. After that, the detector has to be protected from possible damage during manipulation. For this purpose, on the

FIGURE 7.10: Mechanical spider and spider's support.

top of the glass a small pillow is set. Now it is feasible to put the spider on the detectors bellow. After that, the detector has to be placed in the spiders support with the stable screws.

4. With the dynamometrical key, the screw of the bellow is taken off and clean it with ethanol and air.

5. Unscrewing a little, the bellow has to have the desired lenght with the help of the ruler and taking care with the liquid scintillator, setting in the spider.

6. Shaking manually is necessary to release the remained N_2.

7. The remaining liquid scintillator is removed with the needles and it is put in the recipient. The contaminated part of the screw has to be cleaned with a smooth paper. The screw is fixed with the dynamometrical key with a strength of 50 N·m. Using a small pillow on the top of the glass, the spider is removed. In that moment great care must be taken when unscrewing the spider to do not damage the down side of the bellow.

8. Quickly the liquid scintillator is cleaned from the top of the bellow.

9. The last step is impregnate the detector with ethanol and clean it with paper and air. The detectors are ready now to continue the building process at the facility in the bunker.

7.10   Assembly

Assembly procedure starts with the detector completely filled and closed. To characterize properly the detector, it is necessary to assemble first the active volume case with a PM tube of reference, since not all PM tubes have the same performance figures. In a second step the PM tube of reference is returned to the active volume of reference, to have again a complete reference detector and finally the new active volume is mounted with his PM tube, shown in Fig. 7.11.

The assembly stage is essential to obtaining the best possible efficiency of the detector during the experiment.

The mounting procedure starts with a thorough cleaning of the glass that separates the active volume of the detector from the PM tube.

The next step is the assembly of the PM tube with the detector. To do that, a small drop of optical grease is placed in the center of the detectors glass. Is important to avoid air bubbles in the grease. Then, it is possible to let the time pass until the drop gets more uniform if it is needed. The optical grease is neccesary to join the PM tube with the glass and the most important characteristic of the grease is the usefulness for the light transmission. The optical grease is selected such that the light pass from one medium (the glass window) to another (the PM tube) with the minimum change in the diffraction coefficient.

Afterwards, the PM tube with the grease is gently put on the detector, rotating until the grease is uniformly distributed on the glass. As the PM tube is very sensitive, is essential to take care in this step.

The NEDA detectors are expected to work in configurations that involve intense magnetic fields. Being the PM tubes performance sensitive to such environment, the PM tube housing incorporates a μ metal foil. For the placement of the housing, the μ metal is pushed a little bit outside the housing, therfore it will be in the lowest position after screwing. Moreover, when the housing is being screwed, is

FIGURE 7.11: Photo Multiplier (PM) tube to be coupled to the detector active volume to get the complete NEDA detector assembly.

important to screw in a sequence jumping to the opposite side in diagonal in order to do not built mechanical stress.

Then, the Voltage Divider (VD) and pusher are set with care to do not cause damage to the cables. Finally, the pusher is fixed and the bellow's support is installed such that is as inside as possible of the housing mechanics boundaries using gaskets. Meanwhile, it is necessary to be sure that the pipe is not out of the housing guide. At this stage the detector is completely built, as it is shown the Fig. 7.12.
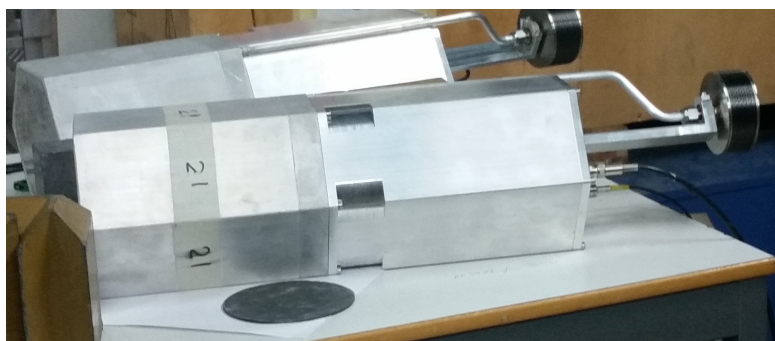
FIGURE 7.12: NEDA detector completed.

7.11   Characterization

As mentioned before the characterization of the detectors is done in two steps. Characterizing first the active volume with a reference PM tube and only after that the detector mounting is completed with its own PM tube for the final characterization.

After cabling, the first functional test is addressed to check if the PM tube and VD mounting is correct by applying slowly high voltage and checking the current provided by the power supply. The detector is covered with a black cloth and some high voltage (HV) is applied. It is essential to observe the current all the time because it should not exceed 800 μA before 1.4 kV.

Secondly, the Single Photoelectron Peak (SPE) is checked. If the SPE spectrum changes after removing the cloth, there is a light leakage and the housing or the mounting process requires further checking. If the spectrum does not change, in the normal course of events, the process has to continue calculating the Number of produced Photo-Electrons (NPE) with ^{137}Cs, ^{60}Co, ^{22}Na and ^{241}Am sources. Thirdly, the ^{60}Co amplitude is checked on the oscilloscope at a HV of 1.4 kV.

The last step in the characterization is the evaluation of the Neutron Gamma Discrimination capabilities. The corresponding performance figure is calculated using an analogue set-up with the NDE202 Bartek NIM electronics module, that performs the Zero Cross Over PSA. On one hand, checking the ^{60}Co on the scope at 1.71 V (adjusting the HV) and on the other hand, taking data for ^{252}Cf and ^{60}Co with the Bartek module. All construction information and performance figures are stored in the NEDA detector construction data base.

The NEDA detectors I contributed to build in my stay at INFN-LNL, were moved to GANIL, France, to be used in a campaign for measurements, including the experiment described in the previous chapters of this thesis.

Chapter 8

Resumen en castellano

8.1 Introducción

La existencia de núcleos con formas deformadas estables se constató experimentalmente temprano en la historia de la física nuclear. La observación de grandes momentos cuadrupolares llevó a sugerir que algunos núcleos podrían tener formas esferoidales, lo que fue confirmado por la observación de las estructuras de bandas rotacionales y, puesto que tal forma es simétrica bajo inversión espacial, todos los miembros de la banda rotacional tendrán la misma paridad.

La región de la tabla de nucleidos que se encuentra justo por encima de la capa cerrada Z=50 en la vecindad de ^{100}Sn exhibe comportamientos colectivos particulares. Además del desarrollo de la deformación al añadir protones en la capa $g_{7/2}$, surgen estructuras de coexistencia de formas, fuertes correlaciones octupolares y acoplamientos de los protones y neutrones ocupando los mismos orbitales.

Este trabajo tiene como objetivo estudiar la estructura del ^{112}Xe, uno de los isótopos ligeros del Xenón con cuatro protones y 8 neutrones por encima del cierre de la capa N=Z=50, a través de la medida de las vidas medias de sus principales estados excitados.

8.2   Resumen

Resumen del capítulo 1.

El objetivo principal de este trabajo es la investigación de la colectividad cuadru-
polar en los isótopos ligeros del Xe, midiendo las vidas medias de los estados de
baja energía en el ^{112}Xe. Al acercarse a las líneas "drip" de neutrones y protones,
es probable que aparezcan nuevos fenómenos y, en particular, las configuraciones
microscópicas pueden ser especialmente pronunciadas en las proximidades de la
línea N=Z debido a la fuerte correlación entre protones y neutrones que ocupan
orbitales idénticos.

La región en la vecindad del ^{100}Sn parece ser de particular importancia en la
investigación del papel de la correlación protón-neutrón en la estructura de las
excitaciones de baja energía. Por encima del ^{100}Sn, los núcleos N=Z no están
ligados, sin embargo, en las proximidades de N=50, la estructura de baja energía
de los isótopos Xe deficientes en neutrones también podría estar influenciada por
el emparejamiento protón-neutrón y por una posible rotura del cierre de capa
correspondiente al ^{100}Sn.

La energía de los estados 2^+ y 4^+ está relacionada con las propiedades colectivas
del núcleo. Dentro de la cadena de isótopos del Xe, el núcleo semimágico ^{136}Xe
presenta la mayor energía de excitación para el estado yrast 2^+ y la menor pro-
babilidad de transición reducida. A medida que se vacía la capa de neutrones, la
colectividad de los isótopos del Xe aumenta hasta el centro de la capa para los
neutrones ($g_{7/2}$, $d_{5/2}$, $d_{3/2}$, $s_{1/2}$, $h_{11/2}$) alrededor de N=66. Si se continúa vaciando
la capa de neutrones, la colectividad parece disminuir, como se esperaba, hasta
N=58 donde hay un cambio inesperado en la tendencia y la colectividad en los
isótopos más ligeros del Xe, parece persistir [3]. En el isótopo más ligero estudiado,
esto está apoyado por un esquema de niveles provisional obtenido experimental-
mente para el ^{110}Xe [4].

Los modelos nucleares han intentado explicar la persistencia de la deformación
examinando la posibilidad de que el aumento del "pairing" protón-neutrón pueda
ser responsable del comportamiento de la sistemática de energía de excitación de
los estados 2^+ y 4^+ en los isótopos ligeros del Xe que se encuentran próximos a
N=Z. Basándose en el esquema del niveles del ^{110}Xe, se propuso que el "pairing"
incluye pares isoescalares tipo deuterón $J = 1$ en los cálculos QRPA realizados por

D.S. Delion et al., siendo éste el ingrediente esencial para describir el comportamiento observado en el ^{110}Xe [5]. Las probabilidades de transición reducidas B(E2) también se predijeron y los cálculos muestran que la tendencia de la B(E2; $2^+ \rightarrow 0^+$) cerca de N=50 es muy sensible a los cambios en los parámetros de "pairing". Sin embargo, las conclusiones de estos cálculos QRPA no coinciden con los resultados de los cálculos del modelo de capa a gran escala (LSSM) utilizando como "core" para el espacio de valencia el núcleo ^{100}Sn [6].

Los cálculos del shell model muestran que el comportamiento tipo rotacional del Xe deficiente en neutrones puede explicarse sin una fuerte contribución de "pairing" isoescalar np y sin reducción del "gap" o separación energética que caracteriza la capa del núcleo doblemente mágico ^{100}Sn. Los cálculos del shell model realizados para estos núcleos colectivos son un desafío para el LSSM por la dimensión del espacio de valencia pero, aun así, el acuerdo entre las energías de excitación calculadas y el esquema de niveles medido es notable. En este escenario, hemos realizado la primera medición de las B(E2)s de los estados yrast de baja energía en el ^{112}Xe a través de la medición de su vida media utilizando la técnica del plunger.

La segunda parte se centra en la colectividad octupolar que genera formas de reflexión asimétrica en los núcleos. En un núcleo par-par con colectividad octupolar desarrollan estados de paridad negativa de baja energía. La deformación octupolar no suelen ser deformaciones estáticas ni tan estables como las cuadrupolares, por ello el término correlación nos parece más adecuado. Las correlaciones octupolares ocurren en presencia de orbitales de paridad opuesta cerca de la superficie de Fermi que difieren en tres unidades de momento angular. En las proximidades del ^{100}Sn, las correlaciones octupolares más fuertes se esperan en el N=Z=56 ^{112}Ba [7]. En los isótopos ligeros de Ba, como en los de Xe, la superficie de Fermi se encuentra entre los orbitales $d_{5/2}$ y $h_{11/2}$ para protones y neutrones. Dado que nos encontramos en la vecindad de N=Z las correlaciones octupolares ocurren para protones y neutrones a la vez.

Experimentalmente, se ha medido una de las correlaciones octupolares más fuertes en el ^{114}Xe [8] que los modelos no pueden reproducir. Para los cálculos en el ^{114}Xe se utilizó el método Generator-Coordinate (GCM) de la teoría de campo medio autoconsistente de Hartree-Fock-Bogoliubov (HFB) con la fuerza de Gogny [9] con éxito en la energía de excitación del estado 3^-. Sin embargo, el cálculo para la probabilidad de transición reducida dio un factor de casi 4 veces menor que el experimental, lo que implica que pueden faltar ingredientes en el modelo.

Otros cálculos tratando de obtener un mejor resultado, por ejemplo utilizando el acoplamiento cuadrupolar y octupolar, producen un resultado similar [10]. Para núcleos ligeros con deformación reducida, como es el caso de los isótopos ligeros del Xe, se ha cuestionado la validez de las fórmulas rotacionales sencillas que ligan las probabilidades reducidas de transición con los parámetros de deformación [11].

En la actualidad, para los isótopos del Xe, no hay mediciones de la colectividad octupolar con las probabilidades de transición reducidas más allá de ^{114}Xe. En este trabajo también se ha medido la vida media del estado 5^- para intentar investigar la correlación octupolar en el ^{112}Xe. Las mediciones de las probabilidades de transición reducidas para las transiciones E3 son en general complejas porque, mientras que la vida media del estado inicial puede determinarse con cualquier transición de alta intensidad que desexcite el nivel, la determinación de la B(E3) requiere la intensidad relativa ("branching ratio") de la transición E3 que, frecuentemente, es muy débil en los espectros experimentales.

Resumen del capítulo 2.

El experimento que forma parte de esta tesis tuvo lugar en GANIL, Francia, con el acelerador de haces estables de iones pesados. Los detectores usados en este experimento son AGATA, NEDA-NW y DIAMANT acoplado al plunger OUPS.

El multidetector AGATA [14], compuesto de detectores de germanio semiconductores, se usa para la espectroscopía de rayos γ de alta resolución. AGATA está construido de detectores segmentados con una electrónica digital que se basa en el análisis de pulso de forma (PSA) para extraer la posición de los puntos de interacción de los rayos γ. Con esta información, junto a la energía extraída con el filtro trapezoidal "Moving Window Deconvolution" (MWD) y el tiempo con el discriminador digital de fracción constante (DCFD), es posible reconstruir la trayectoria de los rayos γ a través del detector. Durante el experimento que forma parte de este trabajo, AGATA se encontraba en la posición nominal y estaba compuesto por 35 cristales, de los cuales 34 estaban operativos.

Los detectores AGATA están construidos en grupos de tres detectores coaxiales de alta pureza (HPGe) de tipo n, asimétricos, encapsulados, segmentados eléctricamente y de forma hexagonal.

La electrónica de AGATA tiene unos preamplificadores que leen las señales de los cristales y están divididos por dos partes separadas, una fría y otra caliente. La

parte fría optimiza el rendimiento del ruido y la parte caliente, fuera del criostato, contiene un amplificador de transimpedancia de bajo ruido, una electrónica de polo cero, un buffer de salida diferencial y un circuito de reinicialización ("reset") rápida. Las señales de cada cristal son digitalizadas con placas ADC de muestreo. La electrónica de preprocesamiento recibe los datos digitales que son filtrados con un segundo nivel de "trigger" a través del Sistema GTS [18]. Por último, la información se envía al flujo de datos de procesamiento a nivel local.

El sistema GTS se encarga de la validación de la petición por parte del procesador de trigger siguiendo una ecuación lógica basada en las condiciones de coincidencia y multiplicidad. En este trabajo se utiliza una condición de coincidencia de 2 detectores de AGATA con señal y un neutrón en NEDA.

El flujo de datos de AGATA contiene una parte de procesado local (LLP) que trata individualmente cada cristal y una parte de procesado global (GLP) que reúne y procesa todos los cristales de AGATA junto con los detectores auxiliares NEDA-NW y DIAMANT.

La determinación de la posición tridimensional de cada punto de interacción, del rayo γ incidente, se realiza en AGATA analizando la forma de la señal de carga y de las seales inducidas de los electrodos del detector. Para ello se usa el llamado análisis de la forma del pulso (PSA) [14], que en nuestro caso utiliza el algoritmo llamado "Adaptative Grid Search". Las posiciones de las interacciones de los rayos γ pueden ser reconstruidas [17] con un FWHM final de aproximadamente 4 mm [24]. La reconstrucción del rayo γ la realiza con el algoritmo del tracking, que reconstruye la trayectoria de los rayos γ dentro del detector. Este algoritmo tiene en consideración las distintas interacciones de los rayos γ con la materia, como el efecto fotoeléctrico, la dispersión Compton y la producción de pares. En este trabajo se usa el algoritmo Orsay Forward Tracking (OFT).

Para la detección de neutrones se usó el multidetector NEDA que tiene una excelente capacidad de discrimación entre γs y neutrones, una eficiencia de detección alta y buenas capacidades de tasa de conteo. También se utilizó el multidetector de neutrones precedente, Neutron Wall, para cubrir ángulos cercanos a 90°. NEDA está diseñado para la experimentación con AGATA y sus configuraciones están optimizadas para ello. La cobertura angular de cada detector individual es de aproximadamente 7.5° [32]. En el experimento de esta tesis se usaron 54 detectores NEDA.

NEDA es un detector de neutrones basado en un centelleador líquido que proporciona una discriminación entre neutrones y γ con un análisis de la forma del pulso y de la información de tiempo de vuelo con una alta capacidad de discriminación entre neutrones y rayos γ. NEDA maximiza la eficiencia de la detección de neutrones y minimiza el "cross-talk" o el doble impacto de un neutrón. Utiliza electrónica digital, el procesamiento digital de señales y, para la discriminación de los neutrones, el análisis digital de la forma del pulso. La electrónica de NEDA usa los digitalizadores NUMEXO2 que adquieren y preprocesan los datos. La placa base de NUMEXO2 cuenta con dos grandes FPGAs para realizar la generación de disparos, el proceso de la señal digital, la sincronización, el empaquetado de datos y la lectura de los datos a los servidores en 16 canales independientes. Los 6 digitalizadores de NUMEXO2 adquieren datos de los 96 detectores de neutrones, 54 de NEDA y 42 de la Neutron-Wall. El sistema NARVAL se encarga de realizar el flujo de datos para NEDA e incluye desde el actor que lee los datos hasta la fusión de los eventos AGATA, DIAMANT y NEDA realizada offline.

La aplicación del Análisis digital de Forma de Pulso (PSA) para discriminar entre neutrones y rayos γ es un progreso de NEDA. El PSA está implementado en el "firmware" de NUMEXO2 para el "trigger" y en el sistema de adquisición de datos online. La decisión del "trigger" se toma después del procesamiento del Discriminador γ de Neutrones (NGD), el tiempo asociado a la detección del neutrón se calcula utilizando un discriminador digital de fracción constante (CFD) que envía la señal de inicio a un convertidor digital de tiempo (TDC) utilizado para obtener el tiempo de vuelo de los neutrones.

Otro detector acoplado a AGATA y necesario para la realización del experimento es DIAMANT, encargado de la detección de partículas cargadas ligeras. Está compuesto de 60 detectores de CsI, construidos con una pieza de cristal centelleador de 3 mm de grosor acoplada a un fotodiodo por una guía de luz de plexiglas de 5mm, para unir el cristal centelleador al fotodiodo. En el experimento desarrollado en este trabajo, para el detector DIAMANT se usó sólo la mitad del ángulo sólido hacia adelante para permitir su acoplamiento con el instrumento plunger. De cada detector, después del preprocesado, se obtienen tres datos, uno es la energía, otro es el tipo de partícula y otro es la referencia temporal relacionada con el momento de la coincidencia entre la partícula y el γ. Estos datos se generan en los digitalizadores NUMEXO2, igual que en NEDA. También tiene la misma adquisición de

datos NEDA. DIAMANT tiene una capacidad intrínseca de discriminación causada por como distintas partículas excitan las componentes de la luz de centelleo que tienen distinta vida media. Esto viene evaluado en el PSA a través de dos filtros trapezoidales. DIAMANT se adquiere sin condición de "trigger".

Acoplado a DIAMANT, el plunger de Orsay OUPS [48], es un dispositivo construido en el CSNSM en colaboración con el IPN Orsay para hacer mediciones de desplazamiento Doppler de distancia de retroceso (RDDS). El plunger consiste en un blanco (target) y una lámina delgada de parada (stopper) o degradador que se montan paralelos entre sí a una distancia variable. Una serie de medidas a distintas distancias nos permite medir los tiempos de vida de los estados nucleares excitados a centenares de picosegundos, mediante el método de desplazamiento Doppler de distancia de retroceso [49]. La reacción nuclear tiene lugar en el target del plunger. Después, los rayos γ emitidos, debido a la desexcitación de los núcleos, se emiten antes o después del stopper o degradador, por lo que son emitidos a velocidades distintas. Usando el desplazamiento Doppler de las energías de los rayos γ se pueden separar estas dos componentes, la desplazada antes del degradador y la no desplazada después del degradador. El desplazamiento es respecto a la energía nominal del rayo-γ y se obtiene esta situación cuando se realiza la corrección Doppler con la velocidad del producto de reacción después del degradador. En el experimento de esta tesis el dispositivo plunger se usó en modo diferencial, es decir, después del blanco se puso un degradador para maximizar la relación entre la resolución del pico y la separación entre las componentes desplazada y no desplazada. Las intensidades de estas dos componentes son necesarias para extraer el tiempo de vida del estado nuclear. Un sistema de retroalimentación, feedback, logra la estabilidad en la distancia entre el objetivo y el degradador. Se encarga de corregir los cambios en las láminas del blanco y el degradador debido a la interacción entre el blanco y el haz.

Resumen del capítulo 3.

El experimento se realizó utilizando una reacción de fusión-evaporación en la que se produjo el núcleo ^{112}Xe, con el haz de ^{58}Ni, suministrado por el acelerador de GANIL con una energía de 250MeV. El haz impactó en el blanco de ^{58}Ni con un espesor de 1mg/cm^2 seguido por la lámina del degradador ^{197}Au con un grosor de 5 mg/cm^2 del plunger. Los rayos γ se midieron con AGATA [14] en coincidencia con el conjunto de detectores de neutrones NEDA-Neutron Wall (NW) [32],[35] y

el detector de partículas cargadas DIAMANT [46] acoplado al dispositivo plunger OUPS [48].

El experimento se realizó con una condición en el trigger de un neutrón identificado en el multidetector NEDA-NW en coincidencia con dos detectores de AGATA con señal. La corriente media del haz fue 4 pnA, es decir, 32 nAe con un estado de carga de 8 en el ^{58}Ni. Este trigger permite evitar el 90% de la detección de canales de reacción no deseados. Las estimaciones de las secciones transversales de fusión-evaporación se calculan con la teoría estadística de Hauser-Feshbach. En esta tesis se usó el software PACE4 [51] e HIVAP [52], encontrando mejores resultados en éste último. Los canales de reacción poblados por la reacción se detallan en la Fig. 3.3 y la tabla 3.1. Los canales de reacción más poblados son el ^{112}I (3p1n) y el ^{112}Te (4p). La estimación de experimentos anteriores, en los que se determinó el esquema de niveles de energía del ^{112}Xe, fue de alrededor de 100 μb, que se encuentran en razonable acuerdo con el cálculo HIVAP.

La eficiencia absoluta de AGATA, usando el tracking, calculada con una fuente de ^{152}Eu calibrada ha sido determinada como parte del análisis y se puede ver en la Fig. 3.5. También se determina la eficiencia de detección de neutrones, sin usar la condición del trigger de un neutrón. Para el análisis se utilizó el canal de reacción 3p1n, el ^{112}I, obteniendo una eficiencia de n = 30(6) %. Para la detección de neutrones, es importante también el factor de discriminación neutrón-γ. Se determinó comparando los espectros sin condición de trigger de neutrones utilizando las condiciones de partículas 0n4p y 1n4p. La transición $2^+ \rightarrow 0^+$ 689 keV del canal de reacción de 4p, el ^{112}Te, fue usada para calcularlo y se obtuvo un factor de discriminación neutrón-γ de 4(2) por mil (es decir, aproximadamente 1/250).

Además, la eficiencia de detección de protones fue calculada con el canal de reacción 3p1n, ^{112}I, usando la relación de las áreas de la transición 210 keV entre las condiciones estrictas de 2 y 3 protones. Un 31(4) % de eficiencia fue obtenida. Es menor que la eficiencia nominal de DIAMANT ($\approx$60% debido a que DIAMANT tenía una configuración reducida para su acoplamiento con el plunger).

Respecto a las medidas realizadas con las distintas distancias entre el blanco y el degradador en el plunger, hay que destacar que debido a la alta corriente del haz y algunos problemas con el feedback se hizo una calibración de las distancias durante

el proceso de análisis de los datos ("off-line"). Es muy importante saber las distancias reales en el plunger para medir el rango de vidas medias de las transiciones de interés en nuestro núcleo. La calibración de cada distancia, nominalmente de 20, 40, 70, 100 y 200-1500 μm se hizo con una referencia de reloj estándar. Las 9 distancias finales fueron 22.4, 39.7, 67, 81, 99, 200, 380, 700 y 1500 μm.

Resumen del capítulo 4.

En la Fig. 4.1 se puede ver esquematicamente el procesado de los datos de AGATA. Para AGATA, el análisis de datos tiene una parte local y una global. En el nivel local hay un análisis online desarrollado durante el experimento y otro offline a partir del filtro Post-PSA en AGATA. A nivel local, el análisis de forma de pulso (PSA), determina los puntos de interacción de los rayos γ en los segmentos del detector. La precisión del PSA requiere que las calibraciones de energía y tiempo, así como las correcciones de "cross-talk", se realicen adecuadamente online.

Para la calibración de energía de cada segmento del detector AGATA (36 segmentos) y las dos señales con diferentes ganancias salidas del preamplificador del núcleo central, se emplearon fuentes de ^{60}Co y ^{152}Eu delante de AGATA.

El "cross-talk" se debe, en parte, a la proximidad de los circuitos del detector y la electrónica analógica, pero también está relacionada con el uso de preamplificadores AC acoplados. Se realizan dos correcciones del "cross-talk" en las señales, el "proporcional" y el "derivado" o "diferencial" [29].

En esta etapa del análisis también se recuperan los segmentos que estén rotos, perdidos o inestables. En este experimento se recupera la información el segmento E6 del detector 00A y el B3 del detector 01B, que estaban rotos, y el segmento C1 del detector 11A que estaba perdido. Asimismo, se tiene que hacer una corrección precisa de la alineación del tiempo obteniéndose los coeficientes de alineamiento. Aunque esta parte se desarrolla en el PSA, luego tendrá que repetirse en el Post-PSA.

Para determinar la posición de interacción de los rayos γ en el PSA, se usa el Adaptive Grid Search algorithm [26]. El algoritmo compara las señales experimentales con las calculadas usando un proceso de minimización con una rejilla "GRID" variable, lo que nos permite optimizar el tiempo del procesamiento.

La etapa fuera de haz "off-line" del análisis de datos empieza con el Post-PSA. Durante el análisis en haz ("on-line") se realiza una corrección de la energía degradada por el daño por neutrones, pero se tiene que mejorar en el Post-PSA.

La corrección de daño por neutrones se tiene que hacer debido a los defectos de la red critalina que aparecen cuando los neutrones rápidos, es decir, los neutrones con energía del orden de MeV, interactúan con el cristal de germanio de AGATA y producen defectos que aparecen como trampas de electrones o huecos. El atrapamiento de cargas (electrones o huecos), provoca una recogida incompleta de la carga y se muestra en el espectro γ con una cola en el lado de baja energía de los picos. La corrección del daño por neutrones reconstruye la energía de la cola del pico mediante una estimación del camino libre medio de los electrones y agujeros considerando la forma de las señales utilizando el programa SortPsaHits [54]. Para este trabajo se corrigieron todos los detectores menos el 1A, 3A, 3B y 3C.

Las recalibraciones de energía también se hacen en esta etapa del análisis así como un alineamiento del tiempo. Para comprobar la alineación del tiempo se construye una matriz de 35 x 35 con los tiempos alineados al centroide nominal TZero de todas las posibles combinaciones de los detectores.

Respecto al llamado nivel global del análisis de datos, El primer paso es la recostrución con el "event builder" de los sucesos de detectores individuales de AGATA que se encuentran dentro de la ventana de coincidencias de tiempo (utilizando el "timestamp" del evento), dichos eventos contienen la información de energías y posiciones de las interacciones. Sucesivamente se añaden los detectores complementarios en el "event merger". La ventana de tiempo de los eventos construidos de AGATA fue de 200 ns y para la construcción de NEDA-NW y de DIAMANT, así como para la unión de los detectores, fue de 300 ns. Especial atención merece el tracking en este capítulo, encargado de reconstruir la secuencia de las interacciones γ dentro de los detectores de AGATA, como ya se mencionó, usando el algoritmo OFT [31]. Los cuatro parámetros del algoritmo OFT fueron optimizados, llegando a los valores óptimos de $\sigma_\theta = 0.95$, $P_{track} = 0.03$ y $P_{sing} = 0$ y un factor de reducción del cluster de 2.

También se hace el alineamiento de tiempo entre los detectores de NEDA y NW. Durante esta fase del análisis, y una vez que ya han sido alineados los tiempos de los detectores de neutrones de NEDA y la NW, la discriminación entre neutrones

y γs se mejora con el PSA off-line de los detectores NEDA y NW usando el algoritmo de la comparación de la carga y el tiempo de vuelo. El algoritmo de la comparación de carga hace dos integraciones, una corta y otra larga y a través de la relación de ambas determina si se ha detectado neutrones o γs, ya que la intensidad relativa de las dos componentes depende de la naturaleza de la partícula detectada. Los parámetros del algoritmo de comparación de carga se optimizaron utilizando una "Figure of Merit"(FoM) que representa la calidad de la discriminación entre neutrón y rayo γ. Para mejorar la discriminación se utiliza también el tiempo de vuelo. Finalmente las condiciones utilizadas en el análisis se definen en la matriz bidimensional donde un eje tiene el resultado de la comparación de carga y en el otro el tiempo de vuelo. Adicionalmente, La dispersión en los tiempos de vuelo de los neutrones es analizada para determinar si un evento con señal en varios detectores de NEDA corresponde a un sólo neutrón o son realmente varios neutrones. El método evalúa cada par de señales en coincidencia de neutrones y si el tiempo de vuelo es suficientemente largo para cubrir la distancia entre los centroides de los detectores, las dos señales procederán del "cross-talk" y se considera como un único neutrón detectado. En cambio si no es suficientemente largo, se considera como la interacción dos neutrones reales.

La detección de partículas ligeras cargadas se hace en DIAMANT y se analiza mediante PSA. Se realiza poniendo condiciones bedimensionales sobre la matriz que tiene en un eje el PID y en el otro la energía. El preprocesado de las señales digitalizadas se realiza, como en el caso de los detectores de neutrones, en la FPGA de NUMEXO2, obteniendo el tiempo, el tipo de partícula y la energía. El tiempo obtenido con el DCFD en DIAMANT se alinea para el posterior análisis de los datos.

Para medir las vidas medias de los estados de interés se usa el método de desplazamiento Doppler de distancia de retroceso (RDDS) usando el instrumento plunger en el experimento. Específicamente se usarán el método de la curva de decaimiento, DCM, y su diferencial, DDCM. En un experimento con un plunger se pueden medir las dos componentes, que se encuentra a distinta energía, de la transición γ, correspondientes a las emisiones, antes y después del degradador, de los productos de la reacción. La vida media se obtiene de la relación entre las intensidades de las componentes γ que muestra la ecuación 4.1 [56]. La velocidad de retroceso de los núcleos $\beta = v/c$ antes y después del degradador, se puede determinar con la ecuación que corrige la energía del efecto Doppler. La velocidad determinada fue

0.038 y 0.013 antes y después del degradador respectivamente, usando la corrección Doppler del pico 552 keV de la transición $9^- \rightarrow 7^-$ del ^{112}I.

El método de la curva de decaimiento (DCM) determina la vida media de los estados excitados en el núcleo mediante la solución de Bateman para las ecuaciones diferenciales de la desintegración (ecuación 4.6) para ajustarlas a los datos experimentales con la relación de intensidades expuesta en la ecuación 4.1 [56].

El método de la curva de decaimiento diferencial (DDCM) mejora al método anterior eliminando errores sitemáticos determinando la vida media de los estados excitados para cada distancia con la ecuación 4.10 [56].

También se ha utilizado una variante del DDCM desarrollada para el análisis del las coincidencias γ-γ. Poniendo una condición de coincidencia en la componente γ desplazada en la matriz γ-γ es posible restringir el modo como se puebla el estado "feeding". Utilizando dicha condición de coincidencia, la vida media se obtiene a través de la ecuación 4.17 [56] para la alimentación directa.

La verificación de la determinación de la vida media con los métodos descritos se ha realizado usando la transición de 643 keV del ^{112}I, obteniendo $\tau = 102$ (3) ps. Esta vida media es conocida, teniendo un valor de 130(25) ps, valores que se encuentran dentro de los errores.

Resumen del capítulo 5.

La medida de vidas medias en el núcleo ^{112}Xe es un reto por la dificultad de poblarlo experimentalmente ya que tiene una sección eficaz de solo unos cientros de microbarn. Es difícil poblar este núcleo experimentalmente, teniendo una sección eficaz del orden de cientos de microbarn. En la Fig. 5.2 se muestran los espectros de las proyecciones de las matrices γ-γ con la condición de partículas 2n2p, para las distintas distancias blanco-degradador medidas, donde se pueden ver las transiciones principales del núcleo ^{112}Xe.

Para realizar el estudio de la colectividad cuadrupolar en nuestro nucleo de interés, es necesario determinar las probabilidades de transición reducidas y para ello se determinan las vidas medias de los estados 4^+ y 2^+. El estado 4^+ está poblado por los estados 6^+ y 5^-. Se usa exclusivamente la alimentación proveniente de la rama del estado 6^+, siendo el primer paso la determinación de su vida media efectiva. Esto se lleva a cabo con una coincidencia γ en las dos componentes de la transición de 466 keV, $2^+ \rightarrow 0^+$, desplazada y no desplazada, en la matriz γ-γ. Usando los

métodos descritos anteriormente, el DCM y el DDCM, obtenemos para la vida media efectiva del estado 6^+ $\tau = 5.0$ (10) ps y 5.0 (8) ps respectivamente. Usamos el resultado del DDCM porque en general es menos sensible a las incertidumbres sistemáticas.

La componente desplazada de la transición de 656 keV, $4^+ \to 2^+$, está casi siempre contaminada por la componente de 643 keV $7^- \to 5^-$ del núcleo ^{112}I y la componente no desplazada por la transición de 663 keV $11^- \to 9^-$ de nuestro núcleo ^{112}Xe.

La determinación de la vida media del estado 4^+ se realiza con una coincidencia γ en ambas componentes de la transición $6^+ \to 4^+$ para evitar la contaminación procedente del ^{112}Xe.

La vida media del estado 4^+ se determina entonces usando la componente no desplazada de la transición $4^+ \to 2^+$, normalizada a la suma de las áreas de ambas componentes de la transición $2^+ \to 0^+$ en el espectro generado con la condición γ de ambas componentes de la transición $6^+ \to 4^+$. El ajuste se hace con el método DCM, considerando una cascada de dos transiciones, $6^+ \to 4^+ \to 2^+$ y fijando la vida media efectiva del estado 6^+, obteniendo una vida media de $\tau = 11.5$ (18) ps (ver Fig. 5.6).

El análisis de la vida media del estado 2^+, teniendo en cuenta que la transición $2^+ \to 0^+$ no tiene contaminantes, se hace usando el método descrito anteriormente del DDCM una gate en la componente desplazada de la transición $4^+ \to 2^+$. Las áreas obtenidas se normalizan a ambas componentes de la transición $2^+ \to 0^+$ en la proyección de la matriz γ-γ. La vida media obtenida es $\tau = 22$ (3) ps (ver Fig. 5.8).

Con las vidas medias determinadas se pueden calcular las probabilidades de transición reducidas que no dependen de la energía y nos proporcionan información sobre el elemento de matriz de la transición cuadrupolar. Usando la vida media del estado 4^+ tenemos una probabilidad de transición reducida B(E2, $4^+ \to 2^+$) = 584 (91) e^2fm^4 y con la vida media del estado 2^+, B(E2, $2^+ \to 0^+$) = 1688 (230) e^2fm^4.

La colectividad octupolar se estudia mediante la determinación de la vida media de los estados de baja energía de la banda octupolar y con la determinación de la intensidad relativa ("branching ratio") de las transiciones E3. En este trabajo se determina la vida media del estado 5^-. Lo hacemos usando la transición más

intensa, la $5^- \rightarrow 4^+$, con energía de 900 keV. La única población que llega al estado 5^- es del estado 7^- ya que se comprobó que la intensidad de la transición de 572 keV $7^- \rightarrow 5^-$ es la misma que la suma de las intensidades de desexcitación del estado 5^-. Por tanto, calculamos la vida media efectiva del estado 7^- para determinar la vida media del estado 5^-.

Usando los espectros con coincidencia γ en ambas componentes de la transición $4^+ \rightarrow 2^+$ y en la transición $2^+ \rightarrow 0^+$ se determina la vida media del 7^- con ambos métodos, DCM y DDCM, obteniendo $\tau = 24$ (2) ps y $\tau = 23.1$ (14) ps respectivamente (ver Fig. 5.10).

La vida media del estado 5^- se determina con la transición $5^- \rightarrow 4^+$, teniendo ya determinada la vida media del estado 7^-, usando el método DDCM con una condición γ en la componente desplazada de la transición $7^- \rightarrow 5^-$. Como anteriormente usando este método, las áreas de la transición de interés se normalizan al área de la suma de ambas componentes de la transición $2^+ \rightarrow 0^+$ en la proyección de la matriz γ-γ. La vida media obtenida es de $\tau = 17(7)$ ps (ver Fig. 5.12).

El valor obtenido para la vida media del estado 5^- se ha verificado usando el método DCM con una condición γ en ambas componentes de la transición $2^+ \rightarrow 0^+$, con una cascada de dos transiciones, $7^- \rightarrow 5^-$ y $5^- \rightarrow 4^+$. Se podría haber usado también la condición γ en la transición $4^+ \rightarrow 2^+$ pero al tener la componente desplazada contaminada por la transición de 643 keV del ^{112}I se descartó su uso.

Para la evaluación de las áreas de la transición $5^- \rightarrow 4^+$ se evitó la contribución de la transición de 919.5 keV $12^+ \rightarrow 10^+$, en coincidencia con la coincidencia γ hecha en la transición $2^+ \rightarrow 0^+$. La vida media determinada fue 20 (9) ps (ver Fig. 5.13), en buen acuerdo con la obtenida previamente de 17(7) ps.

La probabilidad de transición reducida para la transición $5^- \rightarrow 4^+$ es calculada asumiendo que es un dipolo eléctrico puro, teniendo en cuenta una proporción de ramificación de $b_{ratio} = 0.82$, con un valor de B(E1, $5^- \rightarrow 4^+$) = 6.2 x 10^{-5} (4) e^2fm^2.

Para estudiar la colectividad octupolar en el núcleo ^{112}Xe, necesitamos tanto la vida media del 5^- como la intensidad relativa ("branching ratio") de la transición E3 que desexcita el estado 5^- hacia el 2^+ que debería tener una energía de 1556 keV. Son conocidas las otras dos transiciones que desexcitan el estado 5^-, de 900 y 372 keV. Es necesario determinar las intensidades relativas de las tres transiciones

para determinar la probabilidad de la transición $5^- \rightarrow 2^+$ y así poder obtener su vida media parcial y la probabilidad de transición reducida. Las intensidades relativas obtenidas son 82 (12)% para la transición de 900 keV, 17(5)% para la transición de 372 keV y 1(2)% para la transición de 1556 keV. Para determinarlas, se utilizó la suma de los espectros de distancias más pequeñas, 22 y 40 μm, teniendo la mejor combinación para calcular las intensidades. En este experimento es muy difícil determinar intensidades muy pequeñas ya que al ser un experimento de plunger, la intensidad se divide en dos, la desplazada y la no desplazada, además de la necesidad de hacer coincidencias γ para obtener espectros limpios.

La intensidad relativa de la transición E3 de 1556 keV parece estar debajo del límite de sensibilidad de nuestro experimento, con un error que hace su intensidad compatible de 0 a 3% con un nivel de confianza del 68%.

La vida media parcial de la transición de 1556 keV sería de $\tau(5^- \rightarrow 2^+) = 1696$ ps, para ser comparada con la vida media de la transición equivalente en el ^{114}Xe $\tau (5^- \rightarrow 2^+) = 1600$ (300) ps teniendo una energía de transición similar, sin embargo el error asociado no nos permite establecer un valor. Lo único que podemos establecer es un límite superior para la probabilidad de transición reducida de B(E3, $5^- \rightarrow 2^+$) < 141000 e^2fm^6 que corresponde a B(E3, $5^- \rightarrow 2^+$) < 189 W.u.

Resumen del capítulo 6.

Un sumario de la sistemática de la deformación cuadrupolar en los isótopos del Xe se encuentra en el estudio de S. Raman y colaboradores [62] que establece un máximo de colectividad hacia la capa media en N=66 y describe una tendencia a reducir la deformación decreciente para los isótopos pesados del Xe hacia la capa cerrada N=82 y para los isótopos ligeros hacia N=50. En el mismo estudio se sugiere una deformación prolata para toda la cadena isotópica. Todos los modelos nucleares presentados en dicho trabajo tienen dificultad en reproducir la sistemática completa de B(E2).

Los resultados de nuestro trabajo son muy relevantes, ya que para la mayoría de modelos colectivos discutidos aquí se predice una persistencia de la deformación del ^{112}Xe con la probabilidad de transición reducida B(E2; $0^+ \rightarrow 2^+$) entre 0.8 y 1 e^2b^2.

En el trabajo de M. Sandzelius y colaboradores [4] se observa una ruptura en la tendencia del incremento de las energías de los primeros estados excitados 2^+ and

4^+ para el núcleo ^{110}Xe, sugiriendo una ruptura en la tendencia de una disminución de colectividad cuando el número de neutrones se acerca a la capa cerrada N=50. En dicho trabajo se sugiere que la razón podría ser una alta interacción isoscalar n-p cerca de la línea N=Z. Como el núcleo ^{110}Xe está fuera del alcance de las técnicas de medición existentes con haces estables, en este trabajo se estudian las transiciones de probabilidad reducida aún desconocidas para el ^{112}Xe.

La comparación de la sistemática, incluyendo los resultados de este trabajo, para los isótopos del Xe junto a los del Te y el Sn, se muestra en las Figs. 6.1 - 6.4. En esta sistemática se ve el inicio de la colectividad para el Xe hacia la capa media en N=66. Se muestra tendencia de la reducción de colectividad cuando se mueve de N=66 hacia los números mágicos de neutrones N=50 y N=82. Se observa también la particularidad de una B(E2, $2^+ \rightarrow 4^+$) muy baja para el ^{114}Xe (N=60) y aún más baja en nuestra medida para el ^{112}Xe (N=58). La proporción B(E2; $4^+ \rightarrow 2^+$)/ B(E2; $2^+ \rightarrow 0^+$) presenta al igual un valor bajo anómalo para un núcleo deformado cuadrupolar, también en correspondencia con la tendencia establecida en el ^{114}Xe.

Con el cálculo de shell model a gran escala (LSSM) [6], usando la interacción GCN50:82 en un espacio de valencia r4h incluyendo todas las órbitas entre N=Z=50 y N=Z=82, los cálculos muestran estructuras deformadas colectivas de naturaleza triaxial. Para el ^{112}Xe se muestra un incremento de la B(E2, 2+ $\rightarrow$ 0+) desde 1130 $e^2 fm^4$ (0.113 e^{2}b^2) en el espacio de valencia pseudo-SU(3) hasta 1460 e^{2}fm^4 (0.146 e^{2}b^2) en el espacio correspondiente al modelo esquemático pseudo + quasi-SU(3). Por lo tanto se necesitaría este espacio para reproducir los datos experimentales. Los cálculos de este estudio no incluyen el quasi-SU(3) pero con una B(E2, $4^+ \rightarrow 2^+$) calculada de 1560 e^{2}fm^4 (0.156 e^{2}b^2) y un Q$_0$ compatible con una deformación con β=0.17, los resultados no coinciden con nuestros resultados experimentales.

Los cálculos basados en el método BMF describen al núcleo ^{112}Xe usando el funcional de densidad de energía de Gogny D1S, desarrollado por el grupo teórico de Madrid en el CIAFF-UAM a cargo de T. R. Rodrguez and L.M.Robledo. La estructura colectiva se puede deducir de la superficie de energía total (TES) que corresponde a la evaluación de la energía del método HFB en función de los grados de libertad colectivos (las deformaciones cuadrupolares y octupolares). En el ^{112}Xe se muestran dos mínimos a $\beta_3 = 0$ y $\beta_2 \approx +0.25$ y $\beta_2 \approx -0.2$. El mínimo absoluto corresponde a la configuración prolata y, en este caso, la degeneración a lo largo de la β_3 es mayor que en el mínimo secundario. Sin embargo, el ^{112}Xe al nivel

del mean-field no presenta una deformación octupolar permanente aunque tiene solo dos neutrones más que el número mágico octupolar N=56. Por tanto, del cálculo TES se extrae que el grado de libertad más relevante será la deformación cuadrupolar. También se concluye, con el estudio de la restauración de simetría (paridad, número de partículas y momento angular) que existe un acoplamiento cuadrupolar-octupolar fuerte en el ^{112}Xe. Se muestra también que el comportamiento cualitativo se reproduce bien en los datos experimentales aunque el espectro se estira sistemáticamente respecto a ellos como suele ocurrir en la implementación del SCCM con estados intrínsecos de HFB axialmente simétricos.

Por otra parte, M. Sandzelius y colaboradores incluyeron en su trabajo un cálculo de "Total Ruthian Surface" (TRS) basado en el formalismo "cranked" Strutinsky, usando un hamiltoniano de un núcleo rotacional la energía mínima en función de los parámetros de deformación β_2, β_4 y γ en formas prolatas moderadamente deformadas con el parámetro de alargamiento β_2 que disminuye gradualmente en función de la disminución del número de neutrores. Resultando una $\beta_2 \approx 0.19$ para el ^{112}Xe. La dependencia de la probabilidades de transición reducidas B(E2) del parámetro de deformación cuadrupolar β_2 implican igualmente una disminución continua de la B(E2) en función de la reducción del número de neutrones [4].

Resumen del capítulo 7.

En este capítulo se describe mi contribución de la construcción de los detectores de neutrones de alta eficiencia NEDA, utilizados posteriormente en el "set-up" del experimento de esta tesis.

La construcción tiene lugar en las instalaciones del Laboratorio Nacional de Legnaro (LNL), perteneciente al Instituto Nacional de Física Nuclear (INFN) de Italia. Una vez construida la mecánica de los contenedores del centelleador líquido, los detectores NEDA pasan por un proceso, explicado en este capítulo, de test de fugas, comprobación de cristales, agitación de los detectores para eliminar gases y el cierre completo de los detectores para su posterior montaje y caracterización.

Para lograr la máxima eficiencia de detección de los detectores NEDA, la superficie tiene que estar totalmente cubierta y la forma hexagonal nos permite optimizar la teselación del plano evitando huecos. La utilización del centelleador líquido ELJN EJ301 (BC501A) se elije para obtener la mejor discriminación entre γ y neutrones, a pesar de las dificultades que presenta la manipulación del líquido centelleador [72] [73]. Con estas características, el diseño final de los detectores NEDA es una

célula hexagonal de aleación de aluminio 6060 con una distancia de 146 mm de lado a lado, paredes de 3 mm de espesor y 205 mm de longitud y con un volumen de 3,15 litros de líquido orgánico centelleador.

En la Fig. 7.2 se muestran las distintas partes del detector NEDA. Contiene un volumen activo conectado con un tubo a la cámara de expansión que se sitúa en la parte superior de la carcasa del tubo fotomultiplicador. La superficie interior está cubierta con pintura reflectante EJ520 que incluye en su composición TiO_2. En la parte superior del volumen activo hay un cristal $5''$ N-BK7 de 5 mm de espesor con una transmitancia del 92% para la longitud de onda de emitida por el centelleador. El rendimiento lumínico del detector es de 2400 (100) fotoelectrones/MeV. Se seleccionó el tubo PM Hamamatsu R11833-100 debido a las buenas características para la discriminación entre neutrones y γ [75] y a las buenas propiedades de temporización [76].

Para comenzar la construcción, el cristal se sella y se realiza un test de fugas. Este proceso se hace con un sistema de vacío, llegando a 10^{-3} mbar. Una vez se alcanza esta presión, el test de fugas se hace con Helio, debido a su capacidad para introducirse por los pequeños fallos que pueda haber en el sellado. El detector se llena posteriormente con el líquido centelleador EJ301, al principio aplicando una leve presión, gravitacionalmente hasta alcanzar un volumen de 2 litros.

Para eliminar el oxígeno del líquido centelleador los detectores se exponen a un proceso de pasode burbujas de N_2 durante 40 minutos y se llenan hasta el volumen máximo de 3.15 litros con un líquido centelleador al que se le haya quitado el oxígeno previamente. En este proceso es posible que se cree nitrógeno y salgan burbujas que serán eliminadas en el siguiente paso, agitando los detectores a 110 rpm.

En la clausura final del detector se ajusta el volumen deseado de la cámara de expansión, en función de la temperatura mínima y la ambiental. Con ayuda del soporte mecánico llamado spider, se atornilla la cámara de expansión limpiando bien todo el líquido centelleador que salga.

Para el montaje del detector, se usan fotomultiplicadores y volúmenes activos de referencia para comprobar que todo funciona correctamente. El fotomultiplicador se monta con el detector usando grasa óptica situada en el centro del cristal. Esta grasa tiene la característica de transmitir la luz de un medio a otro con el mínimo coeficiente de difracción. La carcasa usada para el fotomultiplicador incluye una

capa de metal μ para protegerlo de intensos campos magnéticos. Después se montan el divisor de voltaje y el "pusher" y el detector queda completamente construido.

Una vez realizado todo el montaje del detector NEDA es caracterizado con las fuentes ^{137}Cs, ^{60}Co, ^{22}Na y ^{241}Am , comprobando que el pico de fotoelectrón simple (SPE) no cambie en el detector y calculando el número de fotoelectrones producidos. Después, se comprueba la amplitud del ^{60}Co con el osciloscopio a un alto voltaje de 1.4 kV. Por último, para la función discriminatoria de neutrones y γ, se usa el módulo NDE202 Bartek NIM con la fuente ^{60}Co a 1.71 V.

Los detectores NEDA que contribuí a construir en el INFN-LNL se trasladaron a GANIL, Francia, para utilizarlos en una campaña experimental que incluyó el experimento descrito en esta tesis.

8.3   Conclusiones

El objetivo de esta tesis es estudiar la evolución de la colectividad cuadrupolar y octupolar en los isótopos ligeros del Xe cuando se aproximan a la línea N=Z a través de la medición de la vida media de los estados excitados del ^{112}Xe, determinando las probabilidades de transición reducidas. Los resultados experimentales obtenidos se han comparado con cálculos de campo medio. Los indicadores R_{42} (definido como la relación entre las energías de excitación de los estados 4^+ y 2^+) y el indicador $R_{42}(B)$ que incluye la relación entre las probabilidades de transición reducidas B(E2; $4_1^+ \to 2_1^+$) y B(E2; $2_1^+ \to 0_1^+$). Nuestro núcleo está fuera de la sistemática. Se puede concluir que la descripción de la evolución de la colectividad en función del momento angular con un modelo rotacional cuadrupolar estándar no es apropiada para el análisis del núcleo ^{112}Xe.

Para el ^{108}Sn también se estudió la diferencia de comportamiento entre B(E2; $4_1^+ \to 2_1^+$) y B(E2; $2_1^+ \to 0_1^+$) donde la B(E2; $4_1^+ \to 2_1^+$) indica que el "pairing" es importante en vez de los cálculos que indican la predominación de la colectividad cuadrupolar. La clave estaría en el balance entre "pairing" y colectividad cuadrupolar. La B(E2;$4_1^+ \to 2_1^+$) no está bien reproducida por los cálculos teóricos, al igual que ocurre en el ^{114}Xe [71]. La explicación propuesta en la referencia [71] sería la posición de la órbita $h_{11/2}$ que se relaciona con la interacción entre la rotación y la deformación octupolar.

En conclusión, mientras el estado 2^+ parece estar bien descrito por todos nuestros modelos (LSSM, BMF y TRS), el estado 4^+ sigue sin explicación. La explicación más lógica para las diferencias entre los estados 2^+ y 4^+ es un cambio de deformación entre el estado 2^+ y el 4^+ y, entonces, la des-excitación $4^+ \rightarrow 2^+$ no será una transición intrabanda, sino que se asemejará más a una transición des-excitación fuera de la banda "decay-out", donde la probabilidad de transición reducida tiene que tener en cuenta los cambios estructurales en el núcleo.

Chapter 9

Riassunto in Italiano

9.1   Introduzione

L'esistenza di nuclei con forme deformate stabili è stata stabilita sperimental-mente all'inizio della storia della fisica nucleare. L'osservazione di elevati momenti di quadrupolo ha portato alla idea di che alcuni nuclei potrebbero avere forme sferoidali, il che è stato confermato dall'osservazione delle strutture delle bande rotazionali e, poiché una tale forma è simmetrica sotto inversione nello spazio, tutti i membri della banda rotazionale avranno la stessa parità.

La regione della tavola dei nuclidi che si trova appena sopra la shell chiusa Z=50 nelle vicinanze di ^{100}Sn ha particolari comportamenti collettivi. Oltre allo sviluppo della deformazione con l'aggiunta di protoni nellorbitale $g_{7/2}$, si osservano strut-ture corrispondenti alla coesistenza di forme nucleari, emergono forti correlazioni ottupolari es strutture caratterizzate da forti accoppiamenti di protoni e neutroni che occupano gli stessi orbitali.

Questo lavoro mira a studiare la struttura del ^{112}Xe, uno degli isotopi leggeri del dello xeno, con quattro protoni e 8 neutroni sopra la doppia chiusura di shell N=Z=50, misurando le vite medie dei suoi stati eccitati a basa energia.

9.2   Riassunto de la tesi di dottorato di ricerca

Riassunto del capitolo 1.

L'obiettivo principale di questo lavoro è l'indagine della collettività di quadrupolo negli isotopi leggeri di Xe misurando le vite medie degli stati a bassa energia nel ^{112}Xe. Nelle vicinanze delle "drip-line" di neutroni e protoni, è probabile che emergano nuovi fenomeni e, particolari configurazioni microscopiche possono essere particolarmente rilevanti in prossimità di N=Z dovuto alla forte correlazione tra protoni e neutroni che occupano orbitali identici.

La regione nelle vicinanze di ^{100}Sn sembra essere di particolare importanza nella indagine sul ruolo della correlazione protone-neutrone, in particolare il "pairing" isoscalare (T=0 pairing) nella struttura delle eccitazioni a bassa energia. Al di sopra di ^{100}Sn, i nuclei N=Z non sono legati, tuttavia, in prossimità di N=50, la struttura a bassa energia degli isotopi Xe poveri di neutroni possono anche essere influenzata da l'accoppiamento di "pairing" protone-neutrone isosvalare, cosi come da una possibile rottura della chiusura di shell dello ^{100}Sn.

Nel nucleo atomico, l'energia degli stati 2^+ e 4^+ è legata alle sue proprietà collettive. All'interno della catena isotopica dello Xe, il nucleo semi-magico ^{136}Xe ha la più alta energia di eccitazione per lo stato yrast 2^+ e la più bassa probabilità di transizione ridotta. Svuotando la shell di neutroni, la collettività degli isotopi Xe aumenta fino il centro della shell ($g_{7/2}$, $d_{5/2}$, $d_{3/2}$, $s_{1/2}$, $h_{11/2}$) intorno a N=66. Se si continua a svuotare la shell di neutroni, la collettività sembra diminuire, come previsto, fino a N=58 dove c'è un cambiamento inaspettato nella tendenza, e la collettività negli isotopi più leggeri del Xe sembra persistere [3]. Nell'isotopo più leggero studiato, questo è supportato da uno schema di livelli sperimentale provvisorio ottenuto per il ^{110}Xe [4].

I modelli nucleari hanno cercato di spiegare, la persistenza della deformazione, esaminando la possibilità di che un forte "pairing" isoscalare di protone-neutrone possa essere responsabile del comportamento della sistematica, dell'energia di eccitazione degli stati 2^+ e 4^+, negli isotopi leggeri di Xe che sono vicini a N=Z. Sulla base dello schema del livelli del ^{110}Xe, nei calcoli QRPA di D.S. Delion et al, è stato suggerito che la correlazione di "pairing" include coppie $J = 1$ isoscalari tipo deutone, essendo questo l'ingrediente essenziale per descrivere il comportamento osservato nel suddetto schema di livelli del ^{110}Xe [5].

Le probabilità di transizione ridotte B(E2) sono stati anche calcolati ed i risulatati mostrano che la tendenza delle B(E2; $2^+ \rightarrow 0^+$) nella vicinanza di N=50 è molto sensibile alle variazioni dei parametri della interazione di "pairing". Tuttavia, le conclusioni di questi calcoli QRPA non coincidono con i risultati dei calcoli del modello a shell Large-Scale Shell Model (LSSM) utilizzando come "core" per lo spazio di valenza del nucleo ^{100}Sn [6].

I calcoli del modello a shell mostrano che il comportamento rotazionale nei Xe leggeri poveri di neutroni può essere spiegato senza un forte contributo del "pairing" isoscalare di protone-neutrone e senza riduzione del gap della chiusura di shell del Sn doppiamente magico. I calcoli del modello a shell eseguiti per questi nuclei collettivi sono una sfida per il LSSM a causa delle dimensioni dello spazio di valenza, ma, anche così, l'accordo tra le energie di eccitazione calcolate e quelle dello schema dei livelli misurati è notevole. In questo lavoro è stata eseguita la prima determinazione delle probabilità di transizione ridotte B(E2)s degli steti yarast bassa energia nel nucleo ^{112}Xe, misurando la loro vita media usando la tecnica dello "RDDS" con lo strumento plunger.

La seconda parte del lavoro versa sulla collettività dell'ottupolo che genera forme asimmetriche per riflessione nei nuclei. In un nucleo pare-pare con collettività ottupolare si sviluppano stati di parità negativa a bassa energia. La deformazione ottupolare non è di solito statica e non sono così stabili come quelle del quadrupolo, quindi il termine correlazione sembra essere più appropriato. Le correlazioni ottupolari si verificano in presenza di orbitali di parità opposta vicino alla superficie di Fermi che hanno tra di loro una differenza di tre unità di momento angolare. Nelle vicinanze dello ^{100}Sn, le correlazioni di ottupolo più forti sono attese nel nucleo con N=Z=56 ^{112}Ba [7]. Negli isotopi leggeri del Ba, come nelli di Xe, la superficie di Fermi si trova tra gli orbitali $d_{5/2}$ e $h_{11/2}$ per protoni e neutroni. Dato che siamo nelle prossimità di N=Z le correlazioni di ottupolo si verificano per i protoni e neutroni allo stesso tempo.

Sperimentalmente, una delle più forti correlazioni di ottupolo è stata misurata nel nucleo ^{114}Xe [8], purtroppo questa correlazione non può essere spiegata con i modelli disponibili. Per i calcoli in ^{114}Xe è stato usato il metodo Generator-Coordinate (GCM) della teoria auto-consistente del campo medio di Hartree-Fock-Bogoliubov (HFB) con la forza di Gogny [9], con successo a riprodurre energia di eccitazione dello stato 3^-. Tuttavia, il calcolo per la probabilità di transizione ridotta ha dato un risultato che è un fattore quasi 4 volte inferiore rispetto a

quello sperimentale, il che potrebbe significare che ci sono ingredienti mancanti nel modello.

Altri calcoli che cercano di migliorare il risultato, per esempio usando l'accoppiamento tra quadrupolo e ottupolo, producono un risultati simile [10]. Per nuclei leggeri con deformazione ridotta, come nel caso degli isotopi leggeri dello Xe anche la validità delle semplici formule rotazionali che collegano le probabilità di transizione ridotte con i parametri di deformazione è stata messa in discussione [11].

Al momento non ci sono misure della collettività di ottupolo, con determinazioni delle probabilità di transizione ridotta, oltre il ^{114}Xe. In questo lavoro, la vita media dello stato 5^- è stata misurata anche per cercare di indagare sulla correlazione di ottupolo nel nucleo ^{112}Xe. Le misure delle probabilità di transizione ridotte per le transizioni E3 sono in generale complesse perché, mentre la vita media dello stato iniziale può essere determinata con qualsiasi transizione ad alta intensità de-eccitando lo stato, la determinazione di B(E3) richiede anche l'intensità relativa ("branching ratio") della transizione E3 che è spesso molto debole negli spettri sperimentali.

Riassunto del capitolo 2.

L'esperimento che costituisce la parte più rilevante di questa tesi è stato realizzato al laboratorio GANIL, in Francia, con il suo complesso di acceleratore di fasci stabili di ioni pesanti. I rivelatori utilizzati sono AGATA, NEDA-NW e DIAMANT accoppiati allo strumento "Plunger" OUPS.

Il sistema di rilevamento AGATA [14], composto da rivelatori a semiconduttore al germanio, è usato per la spettroscopia ad alta risoluzione di raggi gamma in misure sotto fascio. AGATA è costruito con rivelatori segmentati e con elettronica digitale. I suo funzionamento si basa nellanalisi della forma degli impulsi (PSA) per estrarre la posizione dei punti di interazione dei raggi gamma. Con questa informazioni, insieme all'energia estratta con il filtro trapezoidale "Moving Window Deconvolution" (MWD) e il tempo ottenuto applicando il discriminatore digitale a frazione costante (DCFD), è possibile ricostruire la traiettoria del raggio gamma attraverso il rilevatore. Durante l'esperimento che fa parte di questa tesi, AGATA era nella posizione nominale ed era composta da 35 cristalli, di cui 34 erano operativi.

I rivelatori compositi (Cluster) di AGATA sono costruiti in gruppi di tre rivelatori coassiali di Germanio di tipo n ad alta purezza (HPGe), con forme esagonali asimmetrica, incapsulati e segmentati elettricamente.

L'elettronica AGATA ha preamplificatori che leggono i segnali dai cristalli e che sono divisi in due parti separate, una dentro il criostato, chiamata fredda ed una allo sterno, chiamata calda. La parte fredda ottimizza le prestazioni di rumore e la parte calda, all'esterno del criostato, contiene un amplificatore a tras-impedenza a basso rumore, la elettronica di polo zero, un buffer di uscita differenziale ed un circuito di reset veloce. I segnali di ogni cristallo sono digitalizzati con schede di campionamento FADC. L'elettronica di pre-processamento riceve i dati digitalizzati, che vengono poi trasmessi soltanto dopo validazione per un secondo livello di trigger fornito attraverso il sistema GTS [18]. In seguito i dati validati sono inviate, tramite il sistema a carico dal flusso di dati, al processamento a livello locale.

Il sistema "Global Trigger and Synchronization" (GTS) è responsabile della validazione della richiesta tramite il "Trigger Processor" che, seguendo un'equazione logica basata sulle condizioni di coincidenza e molteplicità. Nellesperimento descritto in questa tesi usiamo una condizione di coincidenza di minimo 2 rivelatori di AGATA con segnale ed almeno 1 neutrone rivelato in NEDA.

Il flusso di dati AGATA contiene una parte di processamento locale (LLP) che tratta ogni cristallo individualmente e una parte di processamento globale (GLP) che mette assieme e processa i dati di tutti i cristalli AGATA cosi come quelli dei rivelatori ausiliari NEDA-NW e DIAMANT.

La determinazione del la posizione tridimensionale di ogni punto di interazione, del raggio gamma incidente, viene eseguita in AGATA analizzando la forma del segnale di carica ed i segnali indotti, raccolte negli elettrodi del rivelatore. Per questo scopo, si utilizza la cosiddetta analisi della forma dell'impulso (PSA) [14], che nel nostro caso utilizza lalgoritmo "Adaptive Grid Search". Il punto dinterazione può essere ricostruito [17] con un FWHM nominale di circa 4 mm [24]. La ricostruzione del raggio gamma viene eseguita con il algoritmo di tracciamento, che ricostruisce la traiettoria all'interno del all'interno del rilevatore tenendo in conto le diverse interazioni delle raggi gamma con la materia dei rivelatore, quale l'effetto fotoelettrico, lo scattering Compton e la produzione di coppie. In questo lavoro viene utilizzato l'algoritmo Orsay Forward Tracking (OFT).

Per la rilevazione dei neutroni, è stato utilizzato il multidetector NEDA, che ha una eccellente discriminazione tra raggi-gamma e neutroni, un'alta efficienza di rilevamento e buone capacità in termini di tasso di conteggio. Il precedente multidetector di neutroni, Neutron Wall, è stato utilizzato anche per coprire angoli vicini ai 90°. NEDA è progettato per la sperimentazione con AGATA e le sue configurazioni sono ottimizzate per il suo abbinamento con essa. La copertura angolare di ogni singolo rivelatore è circa 7,5° [32]. Nell'esperimento di questa tesi sono stati utilizzati 54 rivelatori di NEDA.

NEDA è un rivelatore di neutroni basato su un scintillatore liquido, che fornisce discriminazione tra neutroni e raggi-gamma con analisi della forma degli impulsi e così come con la misura del tempo di volo (time-of-flight ToF) con un'elevata capacità di discriminazione. NEDA massimizza l'efficienza del rilevamento dei neutroni e minimizza il "cross talk" o il doppio colpo di un neutrone.

NEDA utilizza elettronica digitale, processamento digitale dei segnali e, per la discriminazione dei neutroni, analisi digitale della forma degli impulsi. L'elettronica NEDA utilizza i digitalizzatori NUMEXO2 che acquisiscono e pre-processano i dati. La scheda madre NUMEXO2 ha due grandi FPGA per eseguire la generazione del trigger, il pre-processamento del segnale digitale, sincronizzazione, formattazione e la trasmisione dei dati verso i server, per ogni uno dei 16 canali indipendenti. Sei digitalizzatori di NUMEXO2 acquisiscono dati dai 96 rivelatori di neutroni, 54 dal NEDA e 42 dal Neutron-Wall. Il sistema NARVAL è incarico di eseguire il trasferimento dei dati di NEDA e comprende tutto, dall'attore che legge i dati alla fusione degli eventi AGATA, DIAMANT e NEDA realizzata indipendentemente dellacquisizione off-line.

L'applicazione della Pulse Shape Analysis (PSA) digitale per discriminare tra neutroni e raggi gamma è un progresso di NEDA. Il PSA è implementato nel "firmware" della NUMEXO2 per il trigger. La decisione di attivazione del trigger viene presa dopo processamento del Neutron-Gamma Discriminator (NGD). Il tempo associato al rilevamento dei neutroni viene calcolato utilizzando un discriminatore a frazione costante digitale (DCFD) che invia il segnale di avvio a un convertitore tempo-digitale (TDC) utilizzato per ottenere il tempo di volo dei neutroni.

Un altro rivelatore abbinato ad AGATA e necessario per questo esperimento sarebbe DIAMANT, che è incaricato di rilevare le particelle cariche leggere emesse

nella reazione. DIAMANT è composto da 60 rivelatori costruiti con cristallo scintillatore CsI, con un spessore di 3 mm, accoppiato a un fotodiodo tramite una guida di luce in plexiglass di 5 mm, usata per unire otticamente il cristallo scintillatore al fotodiodo. Nell'esperimento realizzato per questo lavoro, del rivelatore DIAMANT è stata utilizzata soltanto la metà dell'angolo solido in avanti per consentire l'accoppiamento con lo strumento Plunger. Da ogni rilevatore, dopo il pre-processamento, si ottengono tre dati, uno è l'energia, altro è il tipo di particella e finalmente è il riferimento temporale. Questi dati vengono costruiti dal digitalizzatore NUMEXO2, come nel caso del NEDA. DIAMANT utilizza lo stesso sistema di acquisizione di dati da NEDA. DIAMANT ha una capacità intrinseca di discriminazione in quanto le diverse particelle eccitano diversi componenti della luce di scintillazione che hanno diverse emivite. La discriminazione è valutata attraverso due filtri trapezoidali. DIAMANT è acquisito senza condizioni di "trigger".

Abbinado a DIAMANT, lo strumento Plunger di Orsay OUPS [48], è un dispositivo costruito al CSNSM in collaborazione con l'IPN di Orsay per effettuare misure di vite medie con la tecnica di spostamento Doppler a distanza rinculo (RDDS). Lo strumento Plunger è composto da un bersaglio ed un "stopper" o un "degrader" montati parallelamente l'uno all'altro ad una distanza variabile. Una serie di misure adiverse distanze bersaglio-degrader (nel nostro caso) ci permette di misurare le vite medie degli stati nucleari eccitati fino centinaia di picosecondi, utilizzando il metodo RDDS [49]. La reazione nucleare avviene nel bersaglio del Plunger, poi, i raggi gamma emessi, dovuti alla de-eccitazione dei nuclei, sono emessi prima o dopo il degrader, quindi sono emessi a diverse velocità. Utilizzando lo spostamento Doppler delle energie dei raggi gamma, è possibile separare queste due componenti, quella spostata prima del degrader e quella non spostata dopo il degradatore. Lo spostamento è rispetto all'energia nominale dei raggi gamma e questa situazione si ottiene quando la correzione Doppler viene eseguita con la velocità del prodotto di reazione dopo il degrader. Come già detto, nell'esperimento di questa tesi il dispositivo Plunger è stato utilizzato in modalità differenziale, vale a dire che un degrader è stato posto dopo ilm bersaglio con lo scopo di massimizzare il rapporto tra la risoluzione del picco e la separazione tra le componenti spostate e non spostate. Le intensità di queste due componenti sono necessarie per estrarre la durata di vita media dello stato nucleare. Un sistema di "feedback", è usato per raggiungere la stabilità nella distanza tra il bersaglio e il degrader. Esso corregge

i cambiamenti nei fogli del berdsaglio e del degrader causati dall'interazione con il fascio.

Riassunto del capitolo 3.

L'esperimento è stato eseguito utilizzando una reazione di fusione-evaporazione in cui il nucleo ^{112}Xe è stato prodotto con il fascio ^{58}Ni fornito dal complesso di acceleratori di GANIL con un'energia di 250MeV. Il fascio ha impattato su un bersaglio di ^{58}Ni di 1mg/cm^2 di spessore seguito dal foglio "degrader" del Plunger che è di ^{197}Au e ha uno spessore di 5 mg/cm^2. I raggi gamma sono stati rivelati con AGATA [14] in coincidenza con l'array di rivelatori di neutroni NEDA-Neutron Wall (NW)[32],[35] ed il rivelatore di particelle cariche leggere DIAMANT [46] abbinato allo strumento plunger OUPS [48].

L'esperimento è stato eseguito con una condizione di "trigger", per lacquisizione dei dati, di un neutrone identificato nel multidetettore NEDA-NW in coincidenza con due rivelatori AGATA con segnale. Questo trigger permette di evitare il 90% del rilevamento di canali di reazione indesiderati. La corrente media del fascio era di 4 pnA (particle nano Ampere), cioè 32 nA con uno stato di carica di 8 per il ^{58}Ni. Le stime delle sezioni d'urto di fusione-evaporazione sono calcolate con programmi che usano la teoria statistica di Hauser-Feshbach. In questa tesi, sono stati utilizzati i programmi PACE4 [51] e HIVAP [52], trovando migliori risultati in quest'ultimo. I canali di reazione popolati dalla reazione sono dettagliati nella 3.3 e nella tabella 3.1. I canali di reazione più popolati sono il ^{112}I (3p1n) e il ^{112}Te (4p). La stima da esperimenti precedenti, in cui è stato determinato lo schema dei livelli energetici del ^{112}Xe, era di circa 100 μbarn, che è in ragionevole accordo con il calcolo HIVAP.

L'efficienza assoluta di AGATA, usando tracciamento ("Tracking"), misurata con una sorgente calibrata di ^{152}Eu, è stata determinata come parte dell'analisi e si trova nella Fig. 3.5. è stata anche determinata l'efficienza di rilevamento dei neutroni, su un insieme di dati acquisiti senza utilizzare una condizione di trigger dei neutroni. Per questo l'analisi è stato utilizzato il canale di reazione 3p1n, che corrisponde al ^{112}I dando un'efficienza di 30(6)%. Per il rilevamento dei neutroni, il fattore di discriminazione neutrone-gamma è anche importante. Questo fattore è stato determinato confrontando gli spettri senza condizione di trigger del neutrone, usando le condizioni di particelle 0n4p e 1n4p e la transizione $2^+ \rightarrow 0^+$ 689 keV del canale di reazione 4p, ^{112}Te, è stato ottenuto un fattore di discriminazione

neutrone-gamma del 4(2) per mille (cioè, circa 1/250 degli eventi senza neutroni viene identificato come in coincidenza con 1 neutrone).

Inoltre, l'efficienza di rilevamento dei protoni è stata determinata con il canale di reazione 3p1n, cioè nel ^{112}I, utilizzando il rapporto delle aree della transizione di 210 keV tra le condizioni di protoni rigorosi 2 e 3. La efficienza ottenuta sarebbe del 31(4)%, inferiore all'efficienza nominale di DIAMANT ($\approx$60% perché DIAMANT aveva una configurazione ridotta $\approx 2\pi$ a causa de l'accoppiamento con il plunger).

Per quanto riguarda le misurazioni effettuate con le diverse distanze tra il bersaglio e il "degrader" nel plunger, va notato che a causa dell'alta corrente del fascio e di alcuni problemi con il feedback, una calibrazione delle distanze è stata necessaria durante il processo di analisi dei dati off-line. è fondamentale conoscere le distanze reali nel plunger per misurare la vita media degli stati dinteresse nel nostro nucleo. La calibrazione di ogni distanza, nominalmente 20, 40, 70, 100, 200, 400 e 1500 μm è stata fatta sulla base dei periodi di acquisizione con un riferimento di tempo reale, non con il orologio del GTS. Le 9 distanze finali sono state 22,4, 39,7, 67, 81, 99, 200, 380, 700 e 1500 μm.

Riassunto del capitolo 4.

Nella Fig. 4.1 il percorso del processamento dei dati AGATA può essere visto schematicamente. Per AGATA, l'analisi dei dati ha una parte chiamata livello "locale" ed unaltra livello "globale". Nell livello locale c'è una parte del analisi che viene fatta "on-line" realizzata durante l'esperimento e un'analisi "off-line", realizzato con posteriorità al esperimento, che sarebbe inclusa nel chiamato filtro "Post-PSA" di AGATA. Nell livello locale è incluso l'analisi della forma dell'impulso (PSA) che determina i punti di interazione dei raggi gamma nei segmenti del rivelatore. L'accuratezza del PSA richiede che le calibrazioni di energia e tempo, così come le correzioni di "cross-talk", siano correttamente eseguite "online".

Per la calibrazione energetica di ogni segmento del rivelatore AGATA (36 segmenti) e i due segnali del contatto centrale "core", che hanno due diversi guadagni in uscita dal preamplificatore, sono state utilizzate sorgenti radioattive di ^{60}Co e ^{152}Eu nella posizione del bersaglio di AGATA.

In AGATA, il "cross-talk" è in parte dovuta alla vicinanza dei circuiti del rivelatore e dell'elettronica analogica, ma è anche legata all'uso di preamplificatori AC

accoppiati. Due correzioni di "cross-talk" sono fatte ai segnali, la "proporzionale" e la "derivata" o "differenziale" [29].

I segmenti che sono rotti, mancanti o instabili sono anche recuperati in questa fase dell'analisi. In questo esperimento, l'informazione è recuperata per i segmenti rotti E6 del rivelatore 00A e B3 del rivelatore 01B, e per il segmento mancante C1 del rivelatore 11A. Inoltre, è necessario effettuare una correzione precisa dell'allineamento temporale ottenendo i coefficienti di allineamento. Anche se questa parte è fatta prima del PSA, dovrà poi essere ripetuta nel Post-PSA.

Per determinare la posizione di interazione dei raggi gamma tramite il PSA, viene utilizzato l'algoritmo Adaptive Grid Search [26]. L'algoritmo confronta i segnali sperimentali con quelli calcolati utilizzando un processo di minimizzazione con una griglia "GRID" variabile, che ci permette di ottimizzare il tempo di processamento.

La fase off-line dell'analisi dei dati inizia con il Post-PSA. Durante l'analisi on-line, viene eseguita una correzione dell'energia degradata dal danno per neutroni, ma comunque deve essere migliorata nel Post-PSA.

Il danno neutronico e causato dai difetti del reticolo cristallino che appaiono quando i neutroni veloci, cioè i neutroni con energie dell'ordine di MeV, interagiscono con il cristallo di germanio di AGATA e producono difetti che appaiono come trappole per elettroni o buchi. L'intrappolamento di cariche (elettroni o buchi) causa una raccolta incompleta di cariche e si manifesta nello spettro gamma con una coda sul lato a bassa energia dei picchi. La correzione del danno neutronico ricostruisce l'energia degli eventi nella coda del picco stimando il percorso libero medio degli elettroni e dei buchi, determinati con il PSA, ed usando il programma SortPsaHits [54]. Per il presente esperimento, tutti i rivelatori tranne i 1A, 3A, 3B e 3C sono stati corretti.

Ricalibrazione energetiche sono anche introdotte in questa fase dell'analisi così come un riallineamento temporale. Per controllare la qualità dell'allineamento temporale, viene costruita una matrice 35 x 35 con i tempi allineati al centroide nominale TZero per tutte le possibili combinazioni di rivelatori.

Per quanto riguarda il cosiddetto livello globale di analisi dei dati, il primo passo è la ricostruzione con il "event builder" degli eventi dei singoli rivelatori AGATA, utilizzando il riferimento di tempo formito dal GTS "timestamp" dell'evento, quando si trova all'interno della finestra di tempo "time-matching", questi eventi

contengono le informazioni sulle energie e le posizioni delle interazioni. I rivelatori complementari vengono aggiunti successivamente nella messa assieme degli eventi con il "event merger". La finestra temporale per gli eventi costruiti da AGATA era di 200 ns e per la costruzione di NEDA-NW e DIAMANT, così come per la messa assieme dei rivelatori, era di 300 ns. In questo capitolo di analisi, merita una particolare attenzione il tracciamento "tracking", che si occupa di ricostruire la sequenza delle interazioni gamma all'interno dei rivelatori AGATA, utilizzando l'algoritmo OFT [31]. I quattro parametri dell'algoritmo OFT sono stati ottimizzati, arrivando ai valori di $\sigma_\theta = 0.95$, $P_{track} = 0.03$ e $P_{sing} = 0$ e un fattore di riduzione dei cluster di 2.

Durante questa fase dell'analisi, e una volta che i tempi dei rivelatori di neutroni NEDA e NW sono stati allineati, la discriminazione tra neutroni e gammas viene migliorata con il PSA off-line dei rivelatori NEDA e NW, in questo caso utilizzando l'algoritmo di confronto di carica "Charge Comparison"(CC). L'algoritmo di confronto delle cariche fa due integrazioni, una breve e una lunga e, attraverso il rapporto delle due, determina se sono stati rilevati neutroni o gamma, poiché l'intensità relativa delle due componenti dipende dalla natura della particella rilevata. I parametri dell'algoritmo di confronto delle cariche sono stati ottimizzati utilizzando una figura di merito "Figure of Merit" (FoM) che rappresenta la qualità della discriminazione tra neutroni e raggi gamma. Per migliorare la discriminazione, viene utilizzato anche il tempo di volo "time-of-flight" (ToF). Finalmente, le condizioni bidimensionali, utilizzate nell'analisi sono definite nella matrice dove un asse ha il risultato del confronto delle cariche (CC) e l'altro il tempo di volo (ToF). Inoltre, le differenze dei tempi di volo dei neutroni vengono analizzate per determinare se un evento con un segnale in diversi rivelatori NEDA corrisponde a un singolo neutrone o a più neutroni. Il metodo valuta ogni coppia di segnali in coincidenza di neutroni e se la differenza di tempo di volo è abbastanza lungo da coprire la distanza tra i punti centri dei rivelatori, verrà considerato che i due segnali corrispondono a un evento di "cross-talk" e perciò viene considerato come un singolo neutrone rilevato. In caso contrario, si considera che levento corrisponde alle l'interazione di due neutroni reali.

Il rilevamento di particelle cariche leggere è fatto con DIAMANT, che è in grado didentificare l particella con lanalisi delle forme dei segnali (PSA). Lidentificazione viene fatta con delle condizioni bidimensionali sulla matrice con il PID su un asse e l'energia rivelata sull'altro. Il pre-processamento dei segnali digitalizzati viene

effettuato, come nel caso dei rivelatori di neutroni, nella FPGA della NUMEXO2, ottenendo dal segnale digitalizzato, il tempo, il tipo di particella e l'energia. Il tempo è ottenuto con il DCFD in DIAMANT, che deve essere allineato successivamente per lanalisi dei dati.

Per misurare le vite medie degli stati di interesse, nell'esperimento viene utilizzato il metodo di spostamento Doppler per distanza di rinculo (RDDS) utilizzando lo strumento plunger. In particolare, verrà utilizzato il metodo della curva di decadimento, DCM, e il suo differenziale, DDCM. In un esperimento con lo strumento plunger, si possono misurare le due componenti della transizione gamma, che sono ad energie diverse, corrispondenti a la emissioni dei raggi-gamma dai prodotti di reazione prima e dopo il foglio "degrader". La vita media si ottiene dal rapporto tra le intensità delle componenti gamma mostrate nell'equazione 4.1 [56]. La velocità di rinculo dei nuclei $\beta = v/c$ prima e dopo il foglio "degrader" può essere determinata con l'equazione che corregge l'energia dall'effetto Doppler. La velocità determinata nel nostro caso era v/c = 0,038 e v/c = 0,013 rispettivamente prima e dopo il foglio "degrader", ed è stata determinata usando la correzione Doppler del picco 552 keV della transizione $9^- \to 7^-$ nel nucleo ^{112}I.

Il metodo della curva di decadimento (DCM) determina la vita media degli stati eccitati nel nucleo usando la soluzione di Bateman, per le equazioni differenziale del decadimento (equazione 4.6) per aggiustare i dati sperimentali con la normalizzazione della intensità dato nell'equazione 4.1 [56].

Il metodo della curva di decadimento differenziale (DDCM) migliora il metodo precedente eliminando gli errori sistematici determinando la vita media degli stati eccitati per ogni distanza con l'equazione 4.10 [56].

In questo analisi, è stata utilizzata anche una variante del DDCM sviluppata per l'analisi usando le coincidenze gamma-gamma. Imponendo una condizione di coincidenza, sulla componente spostata (veloce) della transizione gamma, nella matrice gamma-gamma, è possibile limitare il modo in cui lo stato è popolato "feeding". Usando una tale condizione di coincidenza, la vita media si ottiene dall'equazione 4.17 [56].

La verifica della determinazione de la vita media, con i metodi descritti, è stata eseguita utilizzando la transizione 643 keV nel nucleo ^{112}I, ottenendo tau = 102 (3) ps. Questa emivita è nota, con un valore di 130(25) ps nella letteratura, ed i due valori rientrano negli errori.

Riassunto del capitolo 5.

La misura delle vite medie nel nucleo ^{112}Xe è impegnativa a causa della difficoltà di popolarlo sperimentalmente, poiché ha una sezione d'urto di produzione di poche centinaia di microbarn. La Fig. 5.2 mostra gli spettri delle proiezioni delle matrici gamma-gamma con la condizione di particelle 2n2p, per le diverse distanze tra bersaglio e foglio "degrader" misurate, dove si possono vedere indicate le principali transizioni del nucleo ^{112}Xe.

Per studiare la collettività di quadrupolo nel nostro nucleo di interesse, è necessario determinare le probabilità di transizione ridotte e a questo scopo si determinano le vite medie degli stati 4^+ e 2^+. Lo stato 4^+ è popolato nella de-eccitazione degli stati 6^+ e 5^-. La sequenza che contiene la de-eccitazione dello stato 6^+ è quella viene utilizzata esclusivamente. Il primo passo per la determinazione della vita media dello stato 4^+ è la misura della vita media effettiva dello stato 6^+. Questo viene realizzato con una condizione di coincidenza sulle due componenti della transizione 466 keV, $2^+ \rightarrow 0^+$, spostata e non spostata, nella matrice gamma-gamma. Usando i metodi descritti sopra, il DCM e il DDCM, otteniamo un valore per la vita media effettiva dello stato 6^+ $\tau = 5.0$ (10) ps e 5.0 (8) ps rispettivamente. In questo caso, come in generale, si adotta il risultato del DDCM perché è meno sensibile alle incertezze sistematiche.

Le componenti spostata e non spostata della transizione 656 keV, $4^+ \rightarrow 2^+$ nel nostro nucleo dinteresse, sono quasi sempre contaminate dalla componente non-spostata della transizione di 643 keV $7^- \rightarrow 5^-$ nel nucleo ^{112}I e dalla componente spostata della transizione di 663 keV $11^- \rightarrow 9^-$ nel ^{112}Xe, rispettivamente.

La determinazione della vita media dello stato 4^+ viene eseguita con una coincidenza gamma in entrambe le componenti della transizione $6^+ \rightarrow 4^+$ per evitare la contaminazione procedente della transizione 663 keV $11^- \rightarrow 9^-$ dello steso nucleo ^{112}Xe, cosi come per semplificare il popolamento dello stato 4^+.

Non essendo possibile ignorare la contaminazione procedente del ^{112}I, la vita media dello stato 4^+ è stato determinato utilizzando soltanto il area della componente non spostata della transizione $4^+ \rightarrow 2^+$, negli spettri per ogni distanza generato con la condizione gamma in entrambe le componenti della transizione $6^+ \rightarrow 4^+$, normalizzata alla somma delle aree di entrambe le componenti della transizione $2^+ \rightarrow 0^+$. La determinazione è fatta con il metodo DCM, considerando una cascata

di due transizioni, $6^+ \rightarrow 4^+ \rightarrow 2^+$ e fissando la vita media effettiva dello stato 6^+, ottenendo una vita media $\tau = 11{,}5$ (18) ps (vedere figura 5.6).

Tenendo conto che la transizione $2^+ \rightarrow 0^+$ non presenta contaminazioni, il corrispondente analisi della vita media dello stato 2^+, è fatta usando il metodo precedentemente descritto del DDCM con una condizione di coincidenza nella componente spostata della transizione $4^+ \rightarrow 2^+$. Le aree ottenute sono normalizzate ad entrambe le componenti della transizione $2^+ \rightarrow 0^+$ nella proiezione della matrice gamma-gamma. La vita media ottenuta con questo metodo è $\tau = 22$ (3) ps (vedere figura 5.8).

Con le vite medie determinate possiamo calcolare probabilità di transizione ridotte che non dipendono dall'energia e ci danno informazioni sull'elemento matrice della transizione di quadrupolo. Usando la vita media dello stato 4^+ abbiamo una probabilità di transizione ridotta B(E2, $4^+ \rightarrow 2^+$) = 584 (91) e^{2}fm^4 e con la vita media dello stato 2^+ determiniamo una B(E2, $2^+ \rightarrow 0^+$) = 1688 (230) e^{2}fm^4.

La collettività di ottupolo è studiata determinando la vita media degli stati a bassa energia della banda ottupolare e determinando la intensità relativa della transizioni E3. In questo lavoro abbiamo determiniamo la vita media dello stato 5^- usando la transizione più intensa, la $5^- \rightarrow 4^+$, con un'energia di 900 keV. Abbiamo determinato che l'unico popolamento che raggiunge lo stato 5^- viene dallo stato 7^- poiché l'intensità della transizione $7^- \rightarrow 5^-$ a 572 keV è uguale alla somma delle intensità di de-eccitazione dello stato 5^-. Di nuovo, per determinare la vita media dello stato 5^- dobbiamo conoscere la vita media effettiva dello stato 7^- poiché e quello che nella sua de-eccitazione lo popola.

Utilizzando gli spettri con coincidenza gamma in entrambe le componenti della transizione $4^+ \rightarrow 2^+$ e nella transizione $2^+ \rightarrow 0^+$, la vita media del 7^- con entrambi i metodi, DCM e DDCM, è determinata, ottenendo $\tau = 24$ (2) ps e $\tau = 23.1$ (14) ps rispettivamente (vedere figura 5.10).

L'vita media dello stato 5^- è determinata tramite la misura della transizione $5^- \rightarrow 4^+$. Avendo determinato già la vita media effettiva dello stato 7^-, la determinazione è possibile farla usando il metodo DDCM con una condizione gamma sulla componente spostata della transizione $7^- \rightarrow 5^-$. Come nel caso precedente, con questo metodo, le aree della transizione di interesse sono normalizzate all'area della somma di entrambe le componenti di transizione $2^+ \rightarrow 0^+$ nella proiezione

della matrice gamma-gamma. La vita media ottenuta per lo stato 5^- è $\tau = 17(7)$ ps (vedere figura 5.12).

Il valore ottenuto per l'vita media dello stato 5^- è stato verificato utilizzando il metodo DCM con una condizione gamma su entrambe le componenti della transizione $2^+ \to 0^+$, con le equazioni corrispondenti ad una cascata di due transizioni, $7^- \to 5^-$ e $5^- \to 4^+$. In principio, la condizione di coincidenza gamma sulla transizione $4^+ \to 2^+$, avrebbe potuto essere anche utilizzata, ma poiché la componente spostata è contaminata dalla transizione 643 keV appartenente al ^{112}I, il suo utilizzo è stato scartato.

Per la valutazione delle aree di transizione $5^- \to 4^+$, il contributo della transizione 919.5 keV $12^+ \to 10^+$ è stato considerato, nella determinazione delle aree con la coincidenza gamma fatta sulla transizione $2^+ \to 0^+$. La vita media determinata in questo caso è stata di 20 (9) ps (vedere figura 5.13), in buon accordo con quella precedentemente ottenuta di 17 (7) ps.

La probabilità di transizione ridotta per la transizione $5^- \to 4^+$ è calcolata assumendo un dipolo elettrico puro, tenendo conto della intensità relativa "branching ratio" di $b_{ratio} = 0,82$, otteniamo il risultato B(E1, $5^- \to 4^+$) = 6,2 x 10^{-5} (4) e^2fm^2.

Per studiare la collettività di ottupolo nel nucleo ^{112}Xe, abbiamo bisogno sia della vita media 5^- che dellintensità relativa "branching ratio" della transizione ottupolare E3 che de-eccita lo stato 5^- allo stato 2^+, che dovrebbe avere un'energia di 1556 keV. Le altre due transizioni che de-eccitano lo stato 5^- sono note ed hanno energie 900 e 372 keV. è necessario determinare le intensità relative delle tre transizioni per determinare la probabilità della transizione $5^- \to 2^+$ e finalmente la probabilità di transizione ridotta. Le intensità relative ottenute sono 82 (12)% per la transizione di 900 keV, 17 (5)% per la transizione di 372 keV e 1 (2)% per la transizione di 1556 keV. Per determinare queste intensità relative abbiamo usato la somma degli spettri delle distanze più piccole, cioè 22 e 40 μm, che ci danno le migliore condizione per determinare le intensità. In questa tipologia di esperimenti, è molto difficile determinare intensità molto piccole poiché, essendo un esperimento con lo strumento plunger, l'intensità delle transizione è divisa nelle due componenti, quella spostata e quella non spostata, incidendo anche, sul numero di conteggi, la necessità di fare coincidenze gamma per ottenere spettri puliti.

L'intensità relativa della transizione E3 1556 keV sembra essere sotto il limite di sensibilità del nostro esperimento, con un errore che rende la sua intensità compatibile con valori da 0 a 3% con un livello di confidenza del 68%.

La vita media parziale della transizione 1556 keV sarebbe $\tau(5^- \to 2^+) = 1696$ ps, da confrontare con l'vita media della transizione equivalente a ^{114}Xe $\tau(5^- \to 2^+) = 1600$ (300) ps avendo una simile energia di transizione, tuttavia l'errore associato non ci permette di stabilire un valore. L'unica cosa che possiamo stabilire è un limite superiore per la probabilità di transizione ridotta di B(E3, $5^- \to 2^+$) < 141000 e^2fm^6 che corrisponde a B(E3, $5^- \to 2^+$) < 189 W.u.

Riassunto del capitolo 6.

Una sintesi della sistematica della deformazione quadrupolare negli isotopi Xe si trova nello studio di S. Raman e collaboratori [62]. In questo lavoro si stabilisce che si trova un massimo di collettività verso la metta della shell a N=66 e descrive una tendenza decrescente nella deformazione per gli isotopi pesanti Xe verso la chiusura di shell N=82 e per gli isotopi leggeri verso N=50. Lo stesso studio suggerisce una deformazione prolata per tutta la catena isotopica. Tutti i modelli nucleari presentati in questo lavoro hanno difficoltà a riprodurre la completa sistematica di B(E2).

I risultati del nostro lavoro sono molto rilevanti rispetto a questo lavoro, poiché per la maggior parte dei modelli collettivi discussi prevedono una persistenza della deformazione ^{112}Xe con una probabilità di transizione ridotta B(E2; $0^+ \to 2^+$) tra 0,8 e 1 e^2b^2 .

Nel lavoro di M. Sandzelius et al [4] si osserva un'interruzione della tendenza all'aumento delle energie dei primi stati eccitati 2^+ e 4^+ per il nucleo ^{110}Xe, cosa che suggerisce un'interruzione della tendenza alla diminuzione della collettività quando il numero di neutroni si avvicina alla chiusura di shell N=50. In questo lavoro si suggerisce che la ragione di questo cambiamento nella tendenza potrebbe essere la contribuzione della interazione di "pairing" protone-neutrone isoscalare che dovrebbe apparire nelle vicinanze di N=Z. Poiché il nucleo ^{110}Xe è al di là della portata delle tecniche di misura esistenti con fasci stabili, in questo lavoro studiamo le transizioni a probabilità ridotta ancora sconosciute nel nucleo vicino ^{112}Xe.

Il confronto della sistematica dei parametri rilevanti, compresi i risultati di questo lavoro, per gli isotopi Xe insieme a quelli di Te e Sn, è mostrato nelle figure 6.1 - 6.4. In queste sistematiche è evidente il massimo della collettività per Xe verso la meta della shell N=66, cosi come la menzionata tendenza alla diminuzione della collettività spostandosi verso i numeri di neutroni magici N=50 e N=82. Notiamo anche la particolarità di un B(E2, $2^+ \rightarrow 4^+$) molto basso per ^{114}Xe (N=60) e ancora più basso nella nostra misura per ^{112} Xe (N=58). Il rapporto B(E2; $4^+ \rightarrow 2^+$)/ B(E2; $2^+ \rightarrow 0^+$) mostra anche un valore particolarmente baso per un nucleo che si aspetta che abbia una deformazione quadrupolare. Comunque il risultato ottenuto sarebbe in linea con la tendenza stabilita dal nucleo ^{114}Xe.

Sono stati pubblicati risultati di calcoli di large-scale shell model (LSSM) [6] per gli isotopi più leggeri dello Xe, realizzati da E. Caurier e collaboratori [40], usando l'interazione GCN50:82 nello spazio di valenza r4h, che include tutti gli orbitali tra N=Z=50 e N=Z=82. I risultati indicano che questi nuclei possono mostrare strutture collettive deformate di natura triassiale. Per in nucleo ^{112}Xe, i calcoli prevedono un aumento di B(E2, 2+ $\rightarrow$ 0+) da 1130 $e^2 fm^4$ (0,113 e^{2}b^2) nello spazio di valenza pseudo-SU(3) a 1460 e^{2}fm^4 (0,146 e^{2}b^2) nello spazio corrispondente al modello schematico pseudo + quasi-SU(3). Questo spazio allargato sarebbe quindi necessario per riprodurre i dati sperimentali. I calcoli LSSM in questo studio non includono la quasi-SU(3) ma i risultato della probabilità di transizione ridotta B(E2, $4^+ \rightarrow 2^+$) calcolata con un valore di 1560 e^{2}fm^4 (0,156 e^{2}b^2) ed un Q_0 compatibile con una deformazione con β=0,17, i risultati non concordano con i nostri risultati sperimentali per lo stato 4+.

Di particolare interesse sono i calcoli basati sul metodo Beyond Mean-Field (BMF), che descrivono il nucleo ^{112}Xe usando il funzionale di densità di energia sulla interazione Gogny D1S. Questi calcoli sono stati realizzati da T. R. Rodrguez e L.M.Robledo che appartengono al gruppo teorico di Madrid al CIAFF-UAM. I parametri della struttura collettiva possono essere ricavati dalla superficie energetica totale (TES) che corrisponde alla valutazione energetica del metodo HFB in funzione dei gradi di libertà collettivi (le deformazioni del quadrupolo e dell'ottupolo). Nel nucleo ^{112}Xe, due minimi sono mostrati a $\beta_3 = 0$ e $\beta_2 \approx +0.25$ e $\beta_2 \approx -0.2$. Il minimo assoluto corrisponde alla configurazione prolata e, in questo caso, la degenerazione lungo il β_3 è maggiore che nel minimo secondario. Tuttavia, il ^{112}Xe, a livello di campo medio, non mostra una deformazione permanente di ottupolo anche se ha solo due neutroni in più rispetto al numero magico di ottupolo N=56.

Pertanto, dal calcolo TES si estrae che il grado di libertà più rilevante sarà la deformazione quadrupolare. Si conclude anche dallo studio, dopo il ripristino delle simmetrie (parità, numero di particelle e momento angolare), che c'è un forte accoppiamento quadrupolo-ottupolo in questo nucleo. I risultati mostrano in più che il comportamento ricavato nei dati sperimentali, è ben riprodotto qualitativamente, anche se lo spettro è sistematicamente allungato rispetto ad essi, come spesso accade intrinsecamente nell'implementazione SCCM con stati HFB assialmente simmetrici.

D'altra parte, M. Sandzelius et al. hanno incluso nel loro lavoro un calcolo "Total Ruthian Surface" (TRS) basato sul formalismo di Strutinsky "cranked", usando una Hamiltoniana di un nucleo rotazionale e calcolando l'energia minima in funzione dei parametri di deformazione β_2, β_4 e gamma in forme prolate moderatamente deformate, viene osservato che il parametro di deformazione β_2 diminuisce gradualmente in funzione del numero decrescente di neutroni. Il risultato indicherebbe un $\beta_2 \approx 0,19$ per lo stato fondamentale del nucleo ^{112}Xe. La dipendenza delle probabilità di transizione ridotta B(E2) dal parametro di deformazione del quadrupolo β_2, implicherebbe ugualmente una diminuzione continua di B(E2) in funzione della diminuzione del numero di neutroni [4].

Riassunto del capitolo 7.

Questo capitolo descrive il mio contributo alla costruzione dei rivelatori di neutroni ad alta efficienza del NEDA, che sono stati successivamente utilizzati nell'allestimento dell'esperimento oggetto di questa tesi.

La costruzione avviene nelle strutture del Laboratorio Nazionale di Legnaro (LNL), appartenente all'Istituto Nazionale di Fisica Nucleare (INFN) in Italia. Una volta costruita la meccanica dei contenitori di scintillatori liquidi, i rivelatori NEDA passano attraverso un processo, spiegato in questo capitolo, di test di tenuta, controllo della finestra di vetro, agitazione dei rivelatori per eliminare i gas e la chiusura completa dei rivelatori per il loro successivo assemblaggio e caratterizzazione.

Per ottenere la massima efficienza di rilevamento dei rivelatori NEDA, la superficie deve essere completamente coperta e la forma esagonale ci permette di ottimizzare la tassellatura del piano evitando gli spazi vuoti. Lo scintillatore liquido ELJN EJ301 (BC501A) è stato scelto, per riempire il volume attivo del rivelatore, con lo scopo di ottenere la migliore discriminazione tra gamma e neutroni, nonostante le difficoltà nel manipolare questo scintillatore liquido [51] [52]. Il disegno finale dei

rivelatori di NEDA sarebbe una cella esagonale in lega di alluminio 6060 con una distanza da lato a lato di 146 mm, pareti spesse 3 mm e 205 mm di lunghezza, e con un volume di 3,15 litri di liquido scintillatore organico.

La Fig. 7.2 mostra le diverse parti del rilevatore NEDA. Contiene un volume attivo collegato con un tubo alla camera di espansione che si trova nella parte dietro allalloggiamento del tubo fotomoltiplicatore. La superficie interna è rivestita di vernice riflettente EJ520 che include TiO_2 nella sua composizione. Nella parte superiore del volume attivo c'è un vetro con un diametro di 5″ N-BK7 di 5 mm di spessore con una trasmissione del 92% per la lunghezza d'onda emessa dallo scintillatore. La resa luminosa del rivelatore è di 2400 (100) fotoelettroni/MeV. Il tubo PM Hamamatsu R11833-100 è stato scelto per le buone caratteristiche per la discriminazione neutrone-gamma [75] e le buone proprietà di temporizzazione [76].

Allinizio della costruzione, la finestra di vetro viene incollata e sigillata per essere dopo testata la sua tenuta. Questo processo è fatto con un sistema di vuoto, raggiungendo 10^{-3} mbar. Una volta raggiunta questa pressione, la prova di tenuta viene effettuata con gas di elio, che viene scelto per la sua capacità di penetrare attraverso piccoli difetti nella tenuta. Il rivelatore viene poi riempito con il liquido scintillatore EJ301, inizialmente applicando una leggera pressione, e dopo usando la gravitazione fino a raggiungere un volume di 2 litri.

Per rimuovere l'ossigeno dal liquido scintillatore, i rivelatori sono esposti a un processo di gorgogliamento di N_2 gassoso per 40 minuti per a continuazione essere riempiti fino al volume massimo di 3,15 litri con liquido scintillatore dal quale l'ossigeno è stato precedentemente rimosso. In questo processo, è possibile che si depositi l'azoto nel liquido e che vengano rilasciate delle bolle, che dovranno essere rimosse nella fase successiva agitando i rivelatori a 110 rpm.

Nel momento della chiusura finale del rilevatore, il volume desiderato della camera di espansione è impostato, in funzione della temperatura minima e della temperatura ambiente. Con l'aiuto di un sistema meccanico, la camera di espansione viene avvitata in posizione e il liquido di scintillazione che fuoriesce viene pulito.

Per il assemblaggio finale del rivelatore, i fotomoltiplicatori e delle celle di liquido scintillatore di riferimento, vengono utilizzati per controllare che tutto funzioni correttamente. Il fotomoltiplicatore è montato, in contatto con la finestra della cella,

usando del grasso ottico posto al centro del vetro. Questo grasso ha la caratteristica di trasmettere la luce da un mezzo all'altro con il più basso cambiamento dei coefficienti di diffrazione. L'alloggiamento usato per il fotomoltiplicatore include uno strato di μ-metallo per proteggerlo dai campi magnetici intensi. Il divisore di tensione e lo "pusher" sono poi montati dietro il fotomoltiplicatore, concludendo la costruzione del rivelatore.

Una volta che il rivelatore di NEDA è completamente assemblato, viene caratterizzato con le sorgenti ^{137}Cs, ^{60}Co, ^{22}Na e ^{241}Am, controllando che il picco di singolo fotoelettrone (SPE) non cambi nel rivelatore e calcolando il numero di fotoelettroni prodotti. Poi, l'ampiezza dil segnale prodotto con la sorgente di ^{60}Co è controllata con l'oscilloscopio ad un'alta tensione di 1,4 kV. Finalmente, per valutare le prestazioni di discriminazione tra neutroni e gamma, viene utilizzato il modulo NIM NDE202 Bartek con la sorgente ^{60}Co a 1,71 V.

I rivelatori NEDA che ho contribuito a costruire all'INFN-LNL sono stati trasferiti al GANIL, in Francia, per essere utilizzati in una campagna sperimentale che comprendeva anche l'esperimento descritto in questa tesi.

9.3 Conclusioni

Lo scopo di questa tesi è quello di studiare l'evoluzione della collettività di quadrupolo e di ottupolo negli isotopi leggeri di Xe quando nelle vicinanze di N=Z attraverso la misura delle vite medie degli stati eccitati a basa energia nel nucleo ^{112}Xe, determinando le probabilità di transizione ridotte corrispondente alle de-eccitazione di questi stati. I risultati sperimentali ottenuti sono stati confrontati con i calcoli di LSSM e di campo medio. Gli indicatori della collettività R_{42} (definita come il rapporto tra le energie di eccitazione degli stati 4^+ e 2^+) e sopra tutto l'indicatore $R_{42}(B)$ che ripresenta il rapporto tra le probabilità di transizione ridotte B(E2; $4_1^+ \rightarrow 2_1^+$) e B(E2; $2_1^+ \rightarrow 0_1^+$) sono nel nostro nucleo è al di fuori della aspettative dei modelli. Si può concludere che la descrizione dell'evoluzione della collettività in funzione del momento angolare con un modello rotazionale quadrupolare standard non è appropriata per la completa caratterizzazione del nucleo ^{112}Xe.

In un caso simile, il ^{108}Sn è stata anche studiata la differenza di comportamento tra B(E2; $4_1^+ \rightarrow 2_1^+$) e B(E2; $2_1^+ \rightarrow 0_1^+$) dove il valore trovato per il B(E2; $4_1^+ \rightarrow$

2_1^+) indicarebbe che li effetti di "pairing" potrebbero essere più rilevanti che la collettività del nucleo deformato. La chiave della descrizione sarebbe l'equilibrio tra li "pairing" e la collettività del quadrupolo. El valore del B(E2;$4_1^+ \to 2_1^+$) non è ben riprodotto dai calcoli teorici, come nel caso di ^{114}Xe [71]. La spiegazione proposta nella referenza [71] sarebbe la posizione in energia di eccitazione del orbitale h$_{11/2}$ che è legata all'interazione tra la rotazione e la deformazione di ottupolo.

Per quello che riguarda al nucleo ^{112}Xe, oggetto di questa tesi, le conclusioni sono che mentre lo stato 2^+ sembra essere ben descritto da tutti i nostri modelli (LSSM, BMF e TRS) e caratterizzato come stato con deformazione quadrupolare, i risultati esperimentali per lo stato 4^+ non coincidono con le predizioni teoriche di nessun modello. La spiegazione più logica per le differenze tra gli stati 2^+ e 4^+ è un cambiamento di deformazione tra lo stato 2^+ e 4^+, e quindi la de-eccitazione 4^+ $\to 2^+$ non sarebbe una transizione intra-banda, ma più una transizione di "decay-out" dove la probabilità di transizione ridotta deve tenere conto dei cambiamenti strutturali nel nucleo.

Bibliography

[1] J.F. Smith et al. Excited states and deformation of ^{112}Xe. *Physics Letters B*, 523:13–21, 2001.

[2] B. Cederwall et al. Evidence for a spin-aligned neutron-proton paired phase from the level structure of ^{92}Pd. *Nature*, 469:68–71, 2011.

[3] J.F. Smith et al. Excited states and deformation of ^{112}Xe. *Physics Letters B*, 523:13–21, 2001.

[4] M. Sandzelius et al. Identification of Excited States in the T_z=1 Nucleus ^{110}Xe: Evidence for Enhanced Collectivity near the N=Z=50 Double Shell Closure. *Physical Review Letters*, 99, 022501, 2007.

[5] D. S. Delion et al. Investigations of proton-neutron correlations close to the drip line. *Physical Review C*, 82, 024307, 2010.

[6] E. Caurier et al. Collectivity in the light xenon isotopes: A shell model study. *Physical Review C*, 82, 064304, 2010.

[7] P.A. Butler and W. Nazarewicz. Intrinsic reflection asymmetry in atomic nuclei. *Reviews of Modern Physics*, 68:349, 1996.

[8] A. Gadea G. de Angelis et al. Coherent proton-neutron contribution to octupole correlations in the neutron-deficient ^{114}Xe nucleus. *Physics Letters B*, 535:93–102, 2002.

[9] L.M. Robledo and G.F. Bertsch. Global systematics of octupole excitations in even-even nuclei. *Physical Review C*, 84, 054302, 2011.

[10] R. Rodríguez-Guzmán et al. Microscopic description of quadrupole-octupole coupling in Sm and Gd isotopes with the Gogny energy density functional. *Physical Review C*, 86, 034336, 2012.

[11] L.M. Robledo and G.F. Bertsch. Electromagnetic transition strengths in soft deformed nuclei. *Physical Review C*, 86, 054306, 2012.

[12] https://www.ganil-spiral2.eu/scientists/ganil-spiral-2-facilities/available-beams/.

[13] O. Kamalou et al. Stable and exotic beams produced at GANIL. *Proceedings of Cyclotrons 2016*, 2016.

[14] S. Akkoyun et al. AGATA-Advanced GAmma Tracking Array. *Nuclear Instruments and Methods in Physics Research A*, 668:26–58, March 2012.

[15] R.M. Lieder. Development of -Ray tracking detectors. *Acta Physica Polonica B*, 32:2395–2401, 2001.

[16] W. Korten et al. Physics opportunities with the Advanced Gamma Tracking Array: AGATA. *Eur. Phys. J. A*, 56:137, 2020.

[17] A. Korichi and T. Lauritsen. Tracking γ rays in highly segmented HPGe detectors: A review of AGATA and GRETINA. *European Physical Journal A*, 55:121, 2019.

[18] M. Bellato. AGATA Global Trigger and Synchronization Hardware. 2005. hal-00729086.

[19] M. Bellato et al. Sub-nanosecond clock synchronization and trigger management in the nuclear physics experiment AGATA. *Journal of Instrumentation*, 8, July 2013.

[20] A. Georgiev et al. An analog-to-digital conversion based on a moving window deconvolution. *IEEE Transactions on Nuclear Science*, 41:1116 – 1124, 1994.

[21] Th. Kroll et al. Nuclear instruments and methods in physics research. *Nuclear instruments and Methods in physics Research A*, 371:489–496, 1996.

[22] E. Gatti et al. Signal evaluation in multielectrode radiation detectors by means of a time dependent weighting vector. *Nuclear instruments and Methods in physics Research*, 193:651, 1982.

[23] P.-A. Söderström et al. Neutron detection and γ-ray suppression using artificial neural networks with the liquid scintillators BC-501A and BC-537. *Nuclear Instruments and Methods in Physics Research A*, 916:238, 2019.

[24] P.-A. Söderström et al. Interaction position resolution simulations and in-beam measurements of the AGATA HPGe detectors. *Nuclear Instruments and Methods in Physics Research A*, 638:96109, 2011.

[25] B. Bruyneel et al. Pulse shape analysis and position determination in segmented HPGe detectors: The AGATA detector library. *European Physical Journal A*, 52(70), 2016.

[26] R. Venturelli and D. Bazzacco. Adaptive grid search as pulse shape analysis algorithm for gamma-tracking and results. *LNL Annual Report 2004*, page 220, 2005.

[27] L. Lewandowski et al. Pulse-Shape Analysis and position resolution in highly segmented HPGe AGATA detectors. *European Physical Journal A*, 55(81), 2019.

[28] B. Bruyneel et al. Correction for hole trapping in AGATA detectors using pulse shape analysis. *The European Physical Journal A*, 49:61, 2013.

[29] B. Bruyneel et al. Crosstalk properties of 36-fold segmented symmetric hexagonal HPGe detectors. *Nuclear Instruments and Methods in Physics Research A*, 599:196–208, 2009.

[30] D. Bazzacco. The Advanced Gamma Ray Tracking Array AGATA. *Nuclear Physics A*, 746:248c–254c, 2004.

[31] A. López-Martens et al. γ-ray tracking algorithms: a comparison. *Nuclear Instruments and Methods in Physics Research A*, 533:454–466, 2004.

[32] J.J. Valiente Dobón et al. NEDA-NEutron Detector Array. *Nuclear Instruments and Methods in Physics Research, A*, 927:81–86, 2019.

[33] J. Simpson et al. The EXOGAM Array: A Radioactive Beam Gamma-Ray Spectrometer. *Heavy ion physics*, pages 159–188, May 2000.

[34] J.J. Valiente-Dobón et al. Status of the Gamma-Ray Spectrometer GALILEO. *LNL Annual Report*, pages 95–96, 2014.

[35] Ö. Skeppstedt et al. The EUROBALL neutron wall - design and performance tests of neutron detectors. *Nuclear Instruments and Methods in Physics Research, A*, 421:531–541, 1999.

[36] J. Ljungvall et al. Monte Carlo simulation of the Neutron Wall detector system. *Nuclear Instruments and Methods in Physics Research, A*, 528:741–762, 2004.

[37] D.G. Sarantites et al. "Neutron Shell": a high efficiency array of neutron detectors for -ray spectroscopic studies with Gammasphere. *Nuclear Instruments and Methods in Physics Research, A*, 530:473–492, 2004.

[38] G. Jaworski et al. Monte Carlo simulation of a single detector unit for the neutron detector array NEDA. *Nuclear Instruments and Methods in Physics Research, A*, 673:64–72, 2012.

[39] T. Hüyük et al. Conceptual design of the early implementation of the NEutron Detector Array (NEDA) with AGATA. *The European Physical Journal, A*, 52:55, 2016.

[40] G. Jaworski et al. The New Neutron multiplicity filter NEDA and its first physics campaign with AGATA. *Acta Physica Polonica B*, 50:585–590, 2019.

[41] E. Clément et al. Conceptual design of the AGATA 1π array at GANIL. *Nuclear Instruments and Methods in Physics Research A*, 855:1–12, May 2017.

[42] F.J. Egea Canet. Design, verification and integration of a fast digitizer for nuclear structure experiments. Application to EXOGAM and NEDA detectors, 2015. Ph.D. Dissertation.

[43] X. Fabian et al. Artificial neural networks for neutron/γ discrimination in the neutron detectors of NEDA. *Nuclear Instruments and Methods in Physics Research A*, 986:164750, 2021.

[44] A. Goasduff et al. Optimization of the NEDA Pulse Shape Analysis for the AGATA-NEDA-DIAMANT Campaign. *LNL Annual Report 2018*, ISSN 1828-8561:104, 2019.

[45] A. Raggio et al. Pulse Shape Analysis of the NEDA Detector, 2016. LNL Annual Report.

[46] J.N. Scheurer et al. Improvments in the in-beam γ-ray spectroscopy provided by an ancillary detector coupled to a Ge y-spectrometer: the DIAMANT-EUROGAM II example. *Nuclear Instruments and Methods in Physics Research A*, 385:501–510, 1997.

[47] B.M. Nyakó et al. DIAMANT-III: the upgraded 4π light charged-particle detector array. private communication.

[48] J. Ljungvall et al. The Orsay Universal Plunger System. *Nuclear Instruments and Methods in Physics Research A*, 679:61–66, 2012.

[49] A. Dewald et al. The Differential Plunger and the Differential Decay Curve Method for the Analysis of Recoil Distance Doppler-Shift Data. *Zeitschrift für Physik A - Atomic Nuclei*, 334:163–175, 1989.

[50] http://nucalf.physics.fsu.edu/ riley/gamma/.

[51] A. Gravron. Statistical model calculations in heavy ion reactions. *Physical Review C*, pages 230–236, 1980.

[52] W. Reisdorf. Analysis of fissionability data at high excitation energies. *Z. Phys. A*, 300:227–238, 1981.

[53] D.C. Radford. ESCL8R and LEVIT8R:Software for interactive graphical analysis of HPGe coincidence data sets. *Nuclear Instruments and Methods in Physics Research A*, 1995.

[54] $https://atrium.in2p3.fr/nuxeo/nxdoc/default/878272cd - bb33 - 4b35 - aa30 - 227c1a38e8d1/view_documents..$

[55] B. Bruyneel et al. Crosstalk corrections for improved energy resolution with highly segmented HPGe-detectors. *Nuclear Instruments and Methods in Physics Research Section A*, 99-106:608(1), 2009.

[56] A. Dewald et al. Developing the Recoil Distance Doppler-Shift technique towards a versatile tool for lifetime measurements of excited nuclear states. *Progress in Particle and Nuclear Physics*, 67:786–839, 2012.

[57] R. Pérez. Collectivity along N=50: Nuclear structure studies on the neutron-magic nuclei ^{92}Mo and ^{94}Ru with AGATA and VAMOS++, 2019. Ph.D. Dissertation.

[58] `https://root.cern.ch/root/htmldoc/guides/users-guide/` `FittingHistograms.html`.

[59] M. M. Giles et al. Lifetime measurements of lowest states in the π g$_{7/2}$ $\otimes$ vh$_{11/2}$ rotational band in ^{112}I. *Physical review*, 98:044315, 2018.

[60] P.A. Butler et al. Octupole collectivity in nuclei. *Journal of Physics G: Nuclear and Particle Physics*, 43, 073002, 2016.

[61] E. Caurier et al. Intrinsic vs Laboratory Frame Description of the Deformed Nucleus ^{48}Cr. *Physical Review Letters*, 75, 13, 1995.

[62] S. Raman et al. Deformation of light xenon isotopes. *Physical Review C*, 52:1830, 1995.

[63] J. Suhonen, editor. *From Nucleons to Nucleus*. Springer, 2010.

[64] M. Goppert Mayer. On closed shells in nuclei. II. *Physical Review*, 75:1969, 1949.

[65] H. Jensen M. Goppert Mayer. Elementary Theory of Nuclear Shell Structure. 1955.

[66] M. Bender et al. Self-consistent mean-field models for nuclear structure. *Reviews of Modern Physics*, 75, 2003.

[67] L.M. Robledo et al. Mean field and beyond description of nuclear structure with the Gogny force: A review. *Journal of Physics G: Nuclear and Particle Physics*, 46, 2019.

[68] R. N. Bernard et al. Octupole correlations in the nucleus ^{144}Ba described with symmetry conserving configuration mixing calculations. *Physical Review C*, 93, 2016.

[69] J.-P. Delaroche et al. Structure of even-even nuclei using a mapped collective Hamiltonian and the D1S Gogny interaction. *Physical Review C*, 81, 2010.

[70] M. Siciliano. Pairing-quadrupole interplay in the neutron-deficient tin nuclei: First lifetime measurements of low-lying states in ^{106,108}Sn. *Physics Letters B*, 806, 2020.

[71] A. Gadea G. de Angelis et al. Coherent proton-neutron contribution to octupole correlations in the neutron-deficient ^{114}Xe nucleus. *Physics Letters B*, 535:93–102, 2002.

[72] P.-A. Söderström et al. Pulse-Shape Discrimination Properties of the BC-501A and BC-537 Liquid Scintillators for the Neutron Detector Array NEDA. *LNL Report*, 238:66, ISSN 1828–8545, 2012.

[73] P.-A. Söderström et al. Neutron detection and gamma-ray suppression using artificial neural networks with the liquid scintillators BC-501A and BC-537. *Nuclear Instruments and Methods in Physics Research, A*, 916:238–245, 2019.

[74] G. Jaworski et al. Monte Carlo simulation of a single detector unit for the neutron detector array NEDA. *Nuclear Instruments and Methods in Physics Research A*, 673:64–72, 2012.

[75] X. Luo et al. Test of digital neutronγ discrimination with four different photomultiplier tubes for the neutron detector array (neda). *Nuclear Instruments and Methods in Physics Research A*, 767:83–91, 2014.

[76] V. Modamio et al. Digital pulse-timing technique for the neutron detector array NEDA. *Nuclear Instruments and Methods in Physics Research A*, 775:71–76, 2015.